
Editorial Office of *Earth's Cryosphere (Kriosfera Zemli)*
Institute of Geography, Russian Academy of Sciences
37 Vavilov str., office 22, Moscow, 117312, Russia
Editorial staff: *N.V. Arutyunyan, N.G. Belova, O.M. Lisitsyna, G.E. Oblogov*
Phone: 8(985) 957-10-01, e-mail: kriozem@gmail.com
Editor of the English translation: *D.E. Konyushkov*

Journal promoted by
Russian Academy of Sciences, Siberian Branch, Novosibirsk
Earth's Cryosphere Institute, Tyumen Scientific Centre SB RAS, Tyumen
Melnikov Permafrost Institute, SB RAS, Yakutsk

Editorial Manager *M.A. Trashkeeva*
Designed by *N.E. Suranova*
Typeset by *N.M. Raisvikh*

RUSSIAN ACADEMY OF SCIENCES
SIBERIAN BRANCH
EARTH'S CRYOSPHERE INSTITUTE, TYUMEN SCIENTIFIC CENTRE
MELNIKOV PERMAFROST INSTITUTE

EARTH'S CRYOSPHERE
SCIENTIFIC JOURNAL

Founded in January 1997	6 issues per year	Vol. XXVII, No. 1	January–February 2023

CONTENTS

EARTH'S CRYOSPHERE
SCIENTIFIC JOURNAL

Earth's Cryosphere, 2023, vol. XXVII, No. 1, pp. 3–11

REGIONAL AND HISTORICAL GEOCRYOLOGY

LATE HOLOCENE CRYOGENIC DEFORMATIONS IN FLOODPLAIN SEDIMENTS OF RIVER VALLEYS IN THE SELENGA RIVER BASIN

Yu.V. Ryzhov[1–3,*], V.L. Kolomiets[4], M.V. Smirnov[1,3]

[1] *Institute of the Earth's Crust, Siberian Branch of the Russian Academy of Sciences, Lermontova St. 128, Irkutsk, 664033 Russia*
[2] *Sochava Institute of Geography, Siberian Branch of the Russian Academy of Sciences, Ulan-Batorskaya St. 1, Irkutsk, 664033 Russia*
[3] *Irkutsk State University, Lenina St. 1, Irkutsk, 664003 Russia*
[4] *Geological Institute, Siberian Branch of the Russian Academy of Sciences, Sakhyanovoi St. 6a, Ulan-Ude, 670047 Russia*

**Corresponding author; e-mail: ryv@crust.irk.ru*

The morphology and age of cryogenic deformations (cryoturbations and ground wedges) in the Holocene floodplain sediments of river valleys in the Selenga River basin within the areas of seasonal, discontinuous, sporadic, and isolated permafrost were studied. Late Holocene ground wedges and cryoturbations were identified in the seasonally frozen layer of floodplain sections of the Itantsa, Il'ka, and Orkhon rivers. The time of formation of the cryogenic deformations was determined on the basis of detailed morphological descriptions and dating of low and high floodplain sediments of these rivers. The age of the alluvium with cryoturbation on the low floodplain is less than 2 kyr. Cryogenic deformations on the high floodplain formed in the Late Holocene (the last 4.2 kyr). It was determined that alluvium layers with cryoturbation are underlain by moderately wet to satiated wet loamy sands and loams. Cryogenic deformations are considered a paleoclimatic indicator of the Late Holocene in the Transbaikal region and northern and central Mongolia.

Keywords*: frost cracking, ground wedge, cryoturbation, floodplain, Late Holocene, Selenga River Basin.*

Recommended citation: Ryzhov Yu.V., Kolomiets V.L., Smirnov M.V., 2023. Late Holocene cryogenic deformations in floodplain sediments of river valleys in the Selenga River basin. *Earth's Cryosphere* XXVII (1), 3–11.

INTRODUCTION

The Selenga River basin with an area of 447 000 km^2 is located in the center of Eurasia – in western and eastern Transbaikalia and northern and central Mongolia; it belongs to the southern geocryological zone with mainly discontinuous, sporadic, and isolated permafrost [*Ershov, 1989; National..., 2007; Jambaljav et al., 2016*]. Sporadic (<50%) and isolated permafrost with a thickness of 0–50 m and the mean rock temperatures from 2 to –1°C predominates in river valleys [*Ershov, 1998; Jambaljav et al., 2016*].

Under conditions of sporadic permafrost, low winter air temperatures (mean January temperature –18...–26°C), low winter (November–March) precipitation (13–43 mm) [*Scientific and Applied..., 1989*], and shallow snow cover (5–30 cm) in the river basins of this region create favorable conditions for frost cracking and cryogenic heaving in floodplains. Cryoturbation and formation of ground wedges take place [*Romanovskii, 1977, 1993; Ershov, 1998*]. Winter temperature inversions with cold air staying back in basins and river valleys favor the development of these processes; in the Uda Depression, they reach 10°C.

ENVIRONMENTAL CONDITIONS OF THE STUDY AREA

The environmental conditions in river valleys of the Selenga River basin are diverse. Thus, the mean annual air temperature changes from –3.7°C in the upper course of the Menza River valley to +2.3°C in the Orkhon River valley. The absolute minimum air temperature varies from –41 to –55°C, the temperature of the soil surface varies from –46 to –55°C [*Scientific..., 1989*]. In the winter (November–March), 5–12% of the annual precipitation (13–80 mm) falls in river valleys and basins [*Scientific..., 1989*]. The mean air temperature of the warmest month (July) varies from 18 to 24°C. Up to 75–80% of the annual precipitation falls in the summer.

Our study was conducted at three sites: Il'kinskii, Itantsinskii, and Orkhonskii (Fig. 1). The Il'kinskii site is located in the bottom of the Bryansk Depression on the right bank of the Il'ka River, between the Il'ka and Novoil'insk villages in the Zaigraevskii district of the Republic of Buryatia. Floodplains, terraces, and lower parts of slopes are composed of the Late Pleistocene and Holocene sands, loamy sands, loams, and gravels. In the river valley,

Fig. 1. Scheme of the Selenga River basin.

Studied sections: (1) high floodplain of the Il'ka River, (2) high floodplain of the Itantsa River, and (3) low floodplain of the Orkhon River.

the relief is accumulative; at the lower part of slopes, it is erosional-accumulative. Low (up to 1.5 m) and high (up to 2.5 m) floodplain surfaces and low first terrace (3–5 m) are clearly distinguished. Eolian ridges and blowouts are noted on the terrace.

The climate is sharply continental; the mean annual air temperature in the settlement of Zaigraevo is –2.5°C. The coldest month is January (–25°C), the warmest month is July (18°C). The mean annual precipitation is 218–241 mm, including 31 mm (11% of the annual norm) in the winter season (November–March). The average depth of the snow cover is 15–20 cm. Sporadic (with a thickness of up to 50 m) and isolated (0–15 m) permafrost areas with mean annual temperatures of 0 to –2°C are present [*Ershov, 1998; National..., 2007*]. On waterlogged floodplains, a hummocky cryogenic microrelief is seen. The height of hummocks (thufurs) does not exceed 0.5 m, and their width is about 1–2 m. According to the mean annual ground temperatures (+2...–2°C), the transitional and semi-transitional types of seasonal thawing–freezing processes are observed in the study area; according to the annual amplitude of temperatures on the surface, this is the sharply continental type [*Dostovalov, Kudryavtsev, 1967*]. The depth of seasonal freezing on the floodplain for loams and clays is 2.2 m; for coarse and gravelly sands, 2.8 m [*Ershov, 1998*]. Alluvial soils are developed on the floodplain, and gray forest soils predominate on the terraces. Meadow landscapes characterize the valley bottom; forest-steppe and steppe landscapes predominate on slopes.

The Itantsinskii site is located in the bottom of the Itantsinsk Depression, on the right bank of the Itantsa River between the Zasukhino and Koma villages in the Pribaikal'sk district of the Republic of Buryatia. Pleistocene and Holocene sands, loamy sands, loams, and gravels compose the surface layer in the valley bottom and surrounding slopes. The relief of the river valley is accumulative; erosional-accumulative landforms are developed on the slopes. Low (0.5–1.5 m) and high (1.5–2.5 m) floodplains and three terraces (4–16 m) are clearly distinguished. The climate is sharply continental; the mean annual air temperature (Turuntaevo weather station) is –1°C. The coldest month is January (–25°C), the warmest month is July (+19°C). The mean annual precipitation is 318 mm, including 61 mm (19% of the annual precipitation) in the winter season (Novem-

ber–March). The average depth of the snow cover is 25–30 cm. This is the area of isolated (0–15-m-thick) permafrost with the mean annual temperature of 0...–1°C [*Ershov, 1998; National..., 2007*]; permafrost areas are mainly confined to waterlogged floodplains. According to the mean annual temperature (+2...–2°C), the transitional and semi-transitional types of seasonal thawing–freezing are observed; according to the amplitude of temperature fluctuations on the surface, this is the sharply continental type. The depth of seasonal freezing on the floodplain for loamy sands and clays is 2 m; for coarse and gravelly sands, 2.65 m. Alluvial soils are on the floodplain, and gray forest soils are on the terraces. Meadow landscapes predominate in the bottom of the valley; forest-steppe landscapes, on south-facing slopes; and taiga landscapes, on mountain slopes.

The third site is located in the piedmont plain of the Khangai Mountains in the Orkhon River valley, 1.5–2 km north of the bridge across the Orkhon River in the city of Kharkhorin (Karakorum) in Mongolia. Floodplains and terraces are composed of Pleistocene and Holocene gravel, sands, loamy sands. Low (up to 2 m) and high (2–5 m) floodplains and the first terrace (7–10 m) are clearly distinguished. The slopes have a cover of colluvial and eolian sediments. The relief is accumulative in the Orkhon River valley, erosional-accumulative and erosional-denudational on the slopes. The climate is sharply continental; the mean annual air temperature in Kharkhorin is +1°C. The coldest month is January (–17.8°C), the warmest month is July (17.7°C). The mean annual precipitation is 364 mm, including 34 mm (9% of the annual norm) in the winter (November–March). According to the mean ground temperature (1...3°C), semi-transitional and long-term stable types of freezing are observed; according to the amplitude of temperature fluctuation on the surface, this is the extremely sharply continental type of soil climate. The depth of seasonal freeze for loamy sands and clays is 1.5 m; for coarse and gravelly sands, 2.2 m. Permafrost is absent [*Jambaljav et al., 2016*]. Chestnut soils of steppe and dry steppe landscapes predominate.

Numerous manifestations of cryogenic processes, specifically pseudomorphs after ice wedges and cryoturbation, are recorded in Neo-Pleistocene deposits of river terraces in the Selenga River basin [*Ravskii, 1972; Tseytlin, 1979; Konstantinov, 1994; Ryzhov, Golubtsov, 2018, 2021*]. Activation phases of frost cracking and heaving are associated with climate cooling [*Fotiev, 2005, 2006, 2009; Vorob'eva, 2010*]. On floodplains composed of Holocene deposits, cryogenic deformations are seen significantly less frequently, as small ground wedges and cryoturbations [*Konstantinov, 1994; Vorob'eva, 2010*]. In the area Ol'khon Island and adjacent coast, six phases of frost cracking have been established and linked to of climate cooling phases [*Vorob'eva, 2010*]. The deepest (0.3–1.0 m) and widest (0.1–0.2 m) ground wedges are identified in geoarchaeological objects aged 2.8–2.6 kyr cal BP. Presently, for the Northern Hemisphere, global cooling events in the Late Holocene are known to occur 2.8–2.6, 1.65–1.45 and 0.65–0.45 kyr cal BP [*Wanner et al., 2011*].

The goal of this work is to describe disturbances in the stratigraphy of Holocene floodplain sediments in the Selenga River Basin in conditions of seasonal freezing, their morphology and their age.

During field work, the main focus fell on the stratigraphy and lithology of sediments and soils and descriptions of disturbances in the stratigraphy of Holocene floodplain sediments. The absolute age of the buried soils was determined in the Saint Petersburg State University and the Sobolev Institute of Geology and Mineralogy (Siberian Branch of the Russian Academy of Sciences) using the carbon of humic acid. The residual carbon activity was measured on a QUANTULUS-1220 (Liquid Scintillation Counters) device. The approximate time of formation of cryoturbations and soil wedges was determined based on the interpolation of data on the calendar age of soil radiocarbon dates. Published data on frost deformations in different Cisbaikal and Transbaikal districts were generalized [*Konstantinov, 1994; Arzhannikov et al., 2010; Vorob'eva, 2010; Alexeev et al., 2014*].

PALEOCRYOGENIC FORMATIONS IN THE LATE HOLOCENE FLOODPLAIN SEDIMENTS

High floodplain of the Il'ka River

In the section of the high floodplain (2.5 m) on the right bank of the Il'ka River (Fig. 2), two stratigraphic layers were noted: the upper soil layer (0–45 cm) composed of humified loamy sands (<3.41 kyr cal BP) and the underlying (50–150 cm) sandy layer with gravel inclusions (>3.71 kyr cal BP) (Fig. 2, Table 1). They are separated by a layer (45–50 cm) of loamy sand aged 3.71–3.41 kyr cal BP. In the upper soil unit, at depths of 27–32 cm, lenses and inclined interlayers of light brown loamy sand with inclusions of sand are seen. The time of their accumulation was 2.8–2.55 kyr cal BP. At depths of 50–150 cm, a buried, 40 cm-wide ground wedge is found (Fig. 2). At depths of 50–70 cm, its width constitutes 20–40 cm; in the lower part, it narrows to 1–10 cm. The wedge is characterized by a subvertical stratigraphy of layers of fine and coarse sand; three thin (1–3 cm) vertical loamy sand interlayers and fine slightly humified sands. The time of formation and filling of the ground wedge was 3.8–3.6 kyr cal BP.

Figure 2*C* shows the distribution of the <1 mm fraction (measurements according to the N.A. Kachinsky method). In the upper layer (0–6 cm) of the modern soil, fine and very fine sand (0.25–0.05 mm) (44%), coarse silt (0.05–0.01 mm) (22%), and fine silt

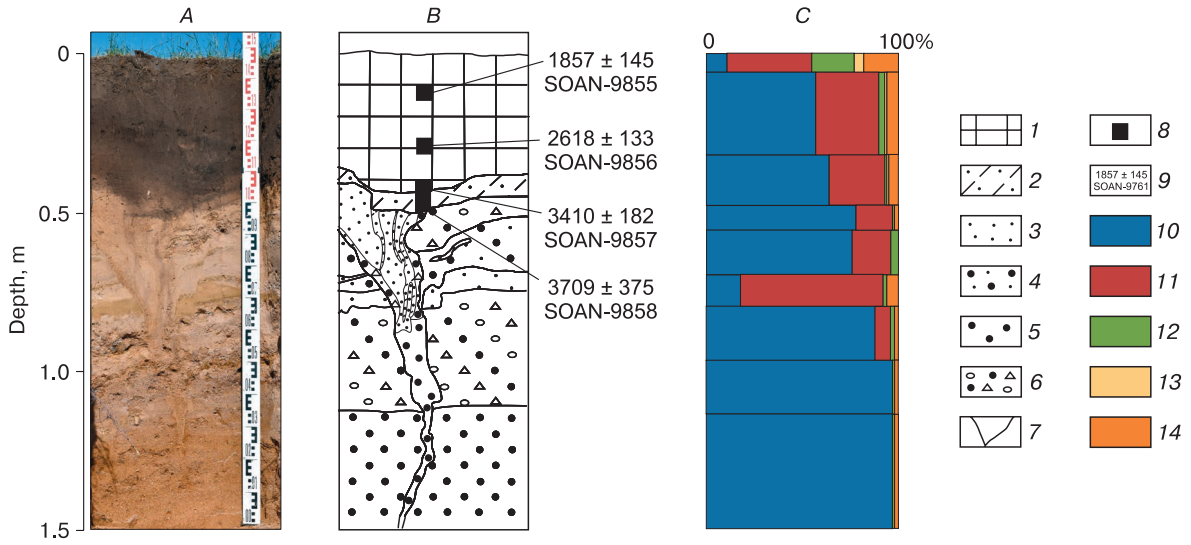

Fig. 2. Section (*A*, *B*) and particle-size distribution data (*C*) of sediments composing the high floodplain of the Il'ka River.

1 – humified loamy sand, light humified loam; *2* – loamy sand, fine and very fine sand; *3* – fine sand; *4* – inequigranular sand; *5* – very coarse sand; *6* – inequigranular sand with grus and gravel; *7* – ground wedge; *8* – sampling for ^{14}C; *9* – calendar age, years ago and sample laboratory number; particle-size fractions (Kachinsky's method), mm: *10* – 1.0–0.25, *11* – 0.25–0.05, *12* – 0.05–0.01; *13* – 0.01–0.005; *14* – 0.005–0.001.

Table 1. **Radiocarbon and calendar age of floodplain sediments**

Horizon	Depth, cm	Laboratory number	^{14}C age, BP	Calendar age, BP
High floodplain (2.5 m) of the Il'ka River, 51°41′43.9″ N, 108°37′20.3″ E, 629 m a.s.l.				
Humified sandy loam	10–15	SOAN-9855	1930 ± 120	1857 ± 145
Humified sandy loam	27–32	SOAN-9856	2535 ± 105	2618 ± 133
Humified loam	40–45	SOAN-9857	3200 ± 150	3410 ± 182
Mix of sandy, humified loamy sand and fine and very fine sand	45–50	SOAN-9858	3400 ± 300	3709 ± 375
High floodplain (1.5–1.7 m) of the Itantsa River, 52°10′30.1″ N, 107°31′49.8″ E, 500 m a.s.l.				
Bottom of humified peaty loam	115–120	SOAN-9761	3120 ± 65	3319 ± 79
Low floodplain (1.3–1.5 m) of the Orkhon River (Mongolia), 47°24′06.8″ N, 102°51′51.0″ E, 1468 m a.s.l.				
Humified loamy sand	13–17	LU-9820	1380 ± 120	1265 ± 112
Humified loamy sand	59–63	LU-9821	2030 ± 140	1985 ± 164
Light, gleyed loam	88–94	LU-9822	2130 ± 110	2085 ± 96

Note: Conversion of radiocarbon dates into calendar dates was performed using Calib Rev 8.1.0 software (calibration curve IntCal20) [*Reimer et al., 2020*].

(0.005–0.001 mm) (18%) fractions dominate. In the lower layer of humified loamy sand (6–48 cm), the contents of coarse and medium (1–0.25 mm) and fine and very fine (0.25–0.05 mm) sand are 57–64 and 29–33%, respectively. The content of fine silt fraction (0.005–0.001 mm) is 5–6%. Coarse and medium sand predominates at a depth of 0.5–0.7 m (1–0.25 mm, 77–88%; 0.25–0.05 mm, 9–19%). Below (0.7–0.8 m), the contents of these fractions change to 18 and 74%, respectively. Fine silt (0.005–0.001 mm) fraction equals 6%. In channel alluvium layers (depth 0.8–1.5 m), coarse and medium (1.0–0.25 mm) sand content is 88–97%.

Low floodplain of the Orkhon River

The low floodplain (1.3–1.5 m) section on the left bank of the Orkhon River near Khakhorin is shown in Fig. 3. It consists of (from top to bottom): humified brown loamy sand with inclusions of gravel (0–12 cm), humified ferruginous gray-brown loamy sand (12–33 cm), mixed gray light gray sand with inclusions of fine and medium gravel (33–42 cm), light

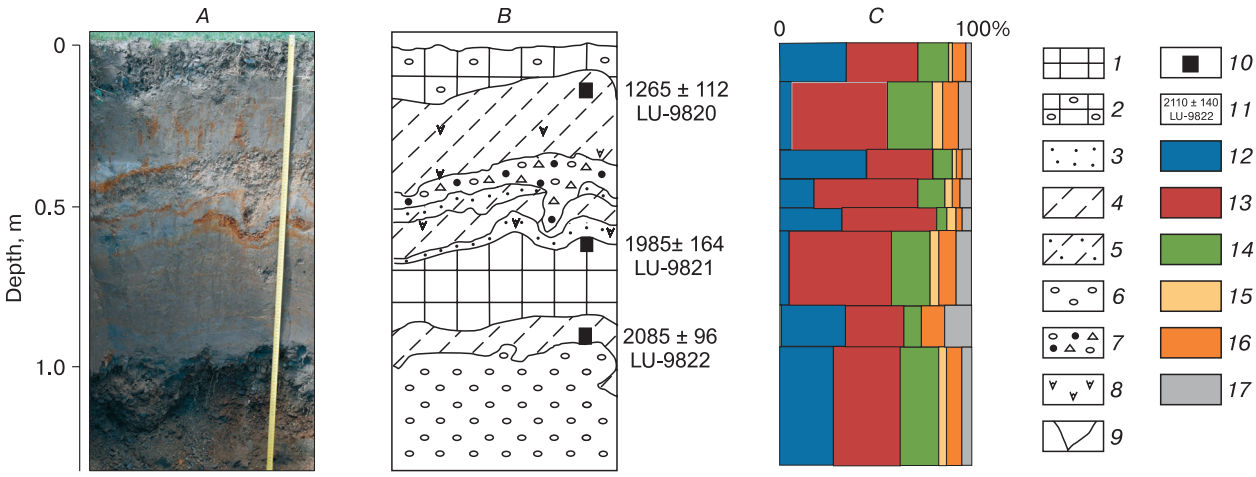

Fig. 3. Section (*A*, *B*) and particle-size distribution data (*C*) of sediments composing the low floodplain of the Orkhon River.

1 – humified loamy sand; *2* – humified loamy sand with small gravel; *3* – fine sand; *4* – loamy sand; *5* – light gray loamy sand, fine sand; *6* – gravel; *7* – differently grained sand with inclusions of grus and gravel; *8* – ferrugination; *9* – outline of cryogenic structure; *10* – sampling for ^{14}C; *11* – calendar age, years ago and sample laboratory number; particle-size fractions (Kachinsky's method), mm: *12* –1.0–0.25, *13* – 0.25–0.05, *14* – 0.05–0.01, *15* – 0.01–0.005, *16* – 0.005–0.001, *17* – <0.001.

gray loamy sand, light gray fine sand, and whitish moist loamy sand (42–51 cm), yellowish brown moist fine sand (51–58 cm), humified dark brown ferruginous moist loamy sand (58–81 cm), light gleyed wet brown loam (81–94 cm), and wet fine and coarse gravel (91–130 cm).

At depths of 39–60 cm, cryogenic disturbances of the alluvium layer stratigraphy (cryoturbations) are seen. Cryoturbations are deformations of sediments looking like swirls, bends, rings, etc. They occur under the influence of dynamic processes caused by freezing–thawing of excessively moistened dispersed rock. The particular kinds of cryoturbations are pockets, frost boils, and some others [*Geocriological Glossary, 2003*].

A ground wedge of 14 cm in width at is seen in the described section, It consists of differently grained sand with inclusions of gravels (39–54 cm), gray and whitish loamy sand (54–56 cm), and ferruginous yellowish brown fine sand (56–60 cm). These layers are inclined or subvertical; together with the wavy patterns of enclosing soil material, this suggests the cryogenic genesis of the wedge. Ferrugination and gleying of humified moist loamy sands (55–81 cm) and light gleyed brown loams (81–94 cm) are the result of high moistening. The age of cryoturbation formation was 1985–1265 cal BP. The cryogenic structure is overlapped and filled by differently grained sands with inclusions of fine gravels resulting from the erosion of the slope of the first terrace of the Orkhon River during spring floods. Sands are underlain by humified dark brown ferruginous loam.

Figure 3*C* shows the distribution of fine earth (<1 mm) fractions in the section. The high content (>52%) of sand fractions (1.0–0.05 mm) is seen in all the layers of the section. The content of silt particles (0.05–0.001 mm) constitutes 10–40%. Minimum values (10–18%) are typical for depths of 0–0.12 and 0.33–0.58 m. At depths of 0.12–0.33, 0.58–1.3 m, the silt content increases to 24–40%. The content of the clay fraction (<0.001 mm) varies from 3.5 to 8% reaching 14% at depths of 0.81–0.94 m. The horizon with cryoturbation features (0.39–0.60 m) in the low floodplain section of the Orkhon River is underlain by moist humified loamy sands; it was formed as a result of deformation during seasonal freezing–thawing of moist river sediments.

High floodplain of the Itantsa River

In the section of the high floodplain (1.5–1.7 m above the water level) of the Itantsa River, alluvial sediments are represented by (from top to bottom): humified dark brown loamy sands with gravel (0–10 cm), reddish brown loamy sands with numerous ocherous mottles (10–33 cm), reddish brown ferruginous loamy sands (33–46 cm), light humified peaty moist loams (46–75 cm), medium humified peaty wet loams with lenses of medium and fine sand (75–120 cm), wet medium and coarse sands with inclusions of gravel from the channel facies alluvium (120–170 cm) (Fig. 4).

At a depth of 36–65 cm, the stratigraphy is disturbed by seasonal freezing–thawing of up to 25 cm in width at the top and a thickness of 30 cm is characterized by the subvertical, wavy, and inclined layers with intrusions of layers into one another. Moist peaty loamy sands are found below. A wedge-shaped structure consists of reddish brown ferruginous

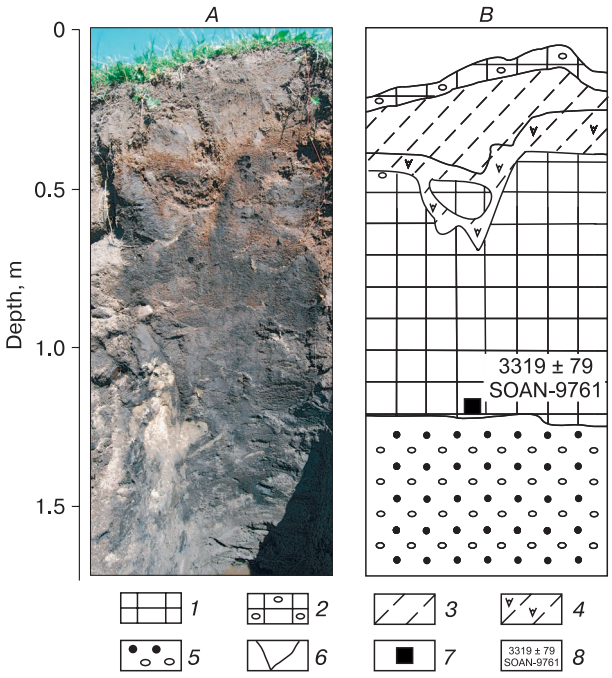

Fig. 4. Section of sediments composing the high floodplain of the Itantsa River.

1 – humified peaty loam; *2* – humified loamy sand with small gravel; *3* – loamy sand with ferrugination mottles; *4* – brown ferruginated loamy sand; *5* – medium and coarse sand with inclusions of gravel; *6* – cryogenic structure; *7* – sampling for ^{14}C; *8* – calendar age, years ago and sample laboratory number.

loamy sands and is overlapped by lenses of light peaty loams and reddish brown ferruginous loamy sands. The loamy layer at the bottom of the section (115–120 cm) dates back to 3319 ± 79 cal BP (Table 1).

DISCUSSION

Low air and soil temperatures in the winter season, moistening of floodplain deposits by surface and ground waters, ferrugination, gleying, the presence of loamy sands and sandy loams in the section favor the development of freeze–thaw processes, cryogenic heaving, and frost cracking of the sediments. The most active cryogenic processes in the Transbaikal region take place in waterlogged floodplain areas, where polygons of 0.5–3.0 m in size are formed and cryogenic microtopography (hummocks, thufurs) is common. Hummocks (thufurs) do not exceed 0.5 m in height and 1–2 m in width [*Ryzhov, Golubtsov, 2018*].

Freezing and thawing of moistened loamy sand and loam leads to deformation of floodplain sediments. Wedge-like structures, and inclined and wavy patters are related to frost cracking and heaving are seen. Usually, layers with cryogenic deformation are underlain by moist loamy sands, loams, or peaty loams. Cryogenic deformations are related to local and regional changes in the environmental conditions (abruptly dropping winter air temperatures, deep freezing of moist Quaternary sediments, climate cooling). During spring and summer flooding, ground wedges and layers with cryoturbation were covered with new portions of alluvium.

Age of cryogenic deformations

Low floodplains began to form in the Late Holocene. The age of the humus soil horizons and cryoturbation features is less than 2 kyr. The time of sediment accumulation on the high floodplain of rivers in the Selenga River Basin extends from the Early to the Late Holocene. An abrupt change in the lithological composition of the sediments and high floods took place 3.8–3.4 kyr cal BP. Cryogenic deformations of sediments on the high floodplain deposits were formed in the Late Holocene (<4.2 kyr cal BP).

The earliest activation phase of frost cracking and heaving in the Late Holocene dates back to 4.2–3.4 kyr cal BP [*Arzhannikov et al., 2010*]. It matches the beginning of the Late Holocene, the Neoglacial, Bond event 3 [*Wanner et al., 2011*]. A cooling phase occurred (3775 ± 40)–(3205 ± 45) BP ((4124 ± 36)–(3418 ± 36) cal BP), when cryoturbation features were formed in the Merzlyi Yar section in the Todzhinskaya Basin in Eastern Sayan at depths of 1.2–0.5 m, as judged from the pollen analysis (a decrease in the content of pollen grains s to 2–6% for fir and 2–9% for pine and an increase in the content of grass pollen) and an annual growth index of buried wood [*Arzhannikov et al., 2010, p. 218*].

G.A. Vorob'eva [*2010*] highlights a cooling ~3.4 kyr BP (3.7–3.6 kyr cal BP). It led to the formation of small ground wedges. At the same time, glaciers appeared in the Bol'shaya Badarinskaya Cave in Priol'khonie [*Vorob'eva, 2010, p. 99*]. According to pollen data and temperature and atmospheric precipitation biomarkers, the climate of Mongolia and Siberia was cold and humid [*Dugerdil et al., 2021*]; according to pedolithological data [*Vorob'eva, 2010, p. 95*], it was temperate and humid.

The stage of frost cracking at the beginning of the Late Holocene, 3.8–3.6 kyr cal BP, reflects regional and local environmental-climatic conditions of the river valleys of Eastern Siberia. It is related to local weather conditions (abnormal low winter air temperatures, deep freezing) and climate cooling. The deterioration of climate conditions 3.8–3.6 kyr cal BP is recorded in the decreased content of diatoms content in bottom sediments of Lake Baikal [*Derevyanko, 2008*]. The formation and burying of the soil wedge described in the Il'ka section took place during this period; in the Il'ka and Itantsa sections, abrupt changes in deposition conditions (substitution of channel alluvium facies by floodplain alluvium) were observed.

Cryogenic involutions took place in the Baikal region 2.7 kyr cal BP [*Vorob'eva, 2010*]. The cooling 2.8–2.6 kyr cal BP is recorded in small ground wedges and cryoturbations in Transbaikal [*Konstantinov et al., 2016*] and Cisbaikal [*Vorob'eva, 2010*] regions. This cooling matches Bond event 2, low solar activity [*Wanner et al., 2011*] and cold dry climate. The accumulation of lenses and inclined interlayers of light brown loamy sand with inclusions of sand attesting to changes in sedimentation conditions (27–32 cm, Il'ka 1 section) are related to this time interval.

The stage of activation of cryogenic processes ~1.5 kyr cal BP was characterized by frost cracking during cooling and aridification of the climate 1.65–1.45 kyr cal BP [*Vorob'eva, 2010; Wanner et al., 2011*]. In the section of the low floodplain of the Orkhon River, a cryoturbated layer (Fig. 3) of light gray loamy sands and gleyed sands overlain by differently grained sands with inclusions of gravel is related to this interval. Steppe landscapes with a relatively dry climate 1.65–1.45 kyr cal BP near Kharkhorin were reconstructed according to palynological data [*Lehmkuhl et al., 2011*].

The final stage of frost cracking is correlated to the Little Ice Age (LIA) (1312–1860) in Siberia [*Vorob'eva, 2010*]. Three phases can be distinguished during the LIA: cold and rainy (1300–1440), relatively warm (1440–1600), and cold (1640–1860) [*Levi, 2014*]. They date back to 0.65–0.51, 0.51–0.35, and 0.31–0.10 kyr cal BP, respectively. It is possible that cryoturbation in floodplain deposits of the Itantsa River is related to the LIA (Fig. 4).

Figures 5*A*–5*C* generalize information about the phases of activation of frost cracking and the duration of warm and cold periods in the Selenga River Basin and adjacent districts in the Late Holocene. A decrease in winter air temperatures occurred during stages of climate cooling [*Tarasov et al., 2007*]. Figure 5*D* shows data on the distribution of diatoms in the bottom sediments of Lake Baikal during the first half of the Holocene [*Derevyanko, 2008*]. Minimum diatom content (100–150 valves/cm) is identi-

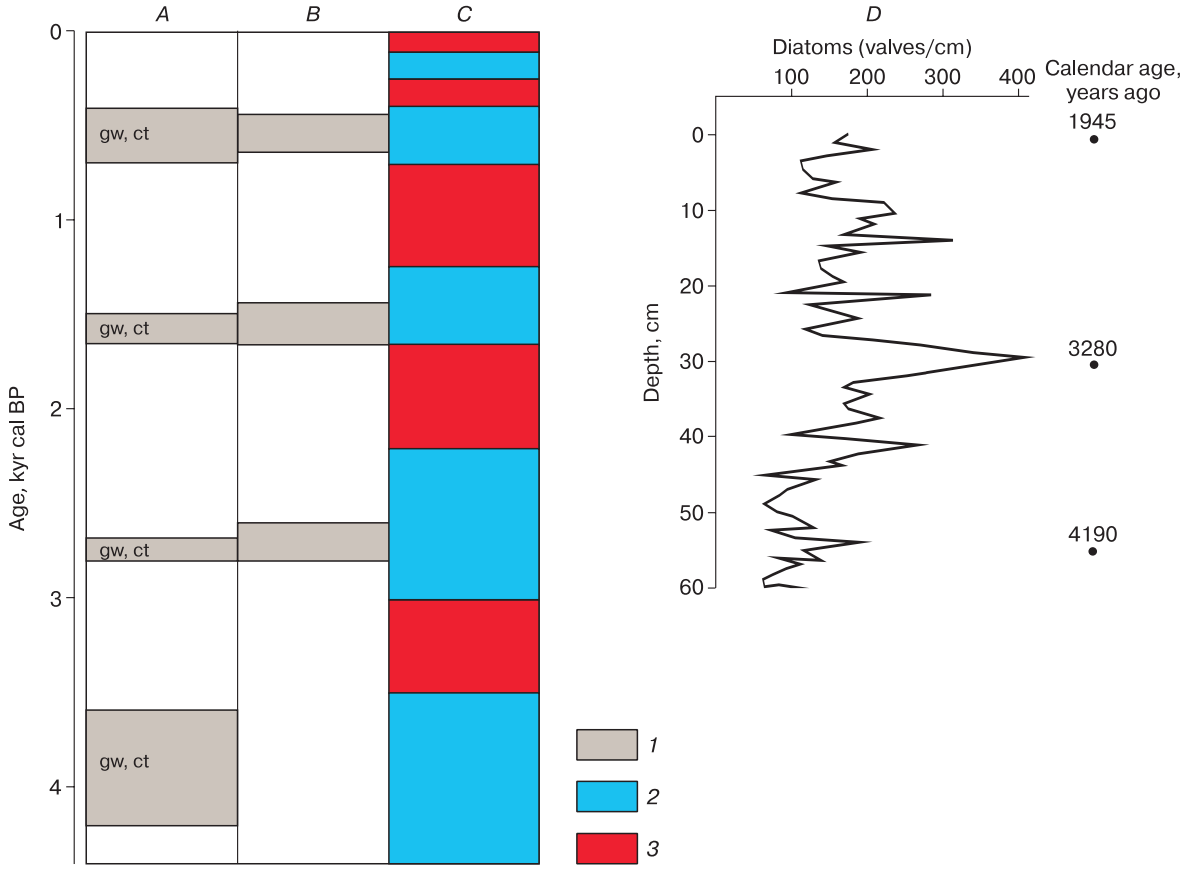

Fig. 5. Chronology of the formation of ground wedges and sediments with cryoturbation features in the Selenga River Basin and adjacent areas in the Late Holocene.

A – cryogenic indicators (gw – ground wedges, ct – cryoturbation); *B* – global cold events (*1*) [*Wanner et al., 2011*]; *C* – periods of cooling (*2*) and warming (*3*) of the climate in the Baikal region and northern Mongolia [*Wang et al., 2004; Vorobieva, 2010; Levi, 2014; Klinge, Sauer, 2019*; *author's data*]; *D* – distribution of diatoms in lacustrine sediments of Lake Baikal (borehole BDP-93-2) [*Global..., 2008*].

fied in the layers of 4.1–3.8 and 2.8 kyr cal BP, which matches climate cooling, low winter air temperatures, a decrease in water temperature, and an increase in the thickness of ice on Lake Baikal.

CONCLUSIONS

Late Holocene floodplain sediments with cryogenic deformations were studied and dated in the valleys of the Il'ka, Itantsa, and Orkhon rivers. Deformations of the normal stratigraphy of the alluvial layers under conditions of seasonal freezing and thawing were noted in the sections of the low and high floodplains. Cryogenic deformations indicate local low winter temperatures, deep freezing, and regional and global changes in the environment and climate.

Buried ground wedges and cryoturbations in alluvium in conditions of seasonal freezing, as well as in the areas of discontinuous, sporadic, and isolated permafrost in river valleys of the Selenga River Basin are related to frost cracking, heaving, and seasonal freezing–thawing of wet floodplain sediments. Particle-size distribution analysis indicated that the cryoturbated layers are underlain by humified moist loamy sands and loams.

Cryogenic deformations of different ages have been identified in the studied sections of floodplain sediments. Cryoturbation features have developed in the alluvium of low floodplains in the past 2 kyr. High floodplains were formed earlier; they consist of the Early and Late Holocene alluvium, and the age of cryogenic deformations in the alluvium of high floodplains is <4.2 kyr cal BP.

The burial of soil wedges and horizons with cryoturbations in the Late Holocene took place during spring and summer flooding. Alluvial sediments differing in their texture and reflecting the hydrological regime of the rivers accumulated on low floodplains. Primarily organic-rich (humified loamy sands and loams) sediments are related to soil formation in conditions of predominantly subaerial deposition predominate in sediment sections on high floodplains.

Ground wedges and cryoturbations in the Selenga River Basin are paleoclimatic indicators of the Late Holocene changes in the environment and climate in the Transbaikal region and Northern and Central Mongolia.

Acknowledgments. *The authors express their deep gratitude to A.Yu. Petrov, F.E. Maksimov, and I. Yu. Ovchinnikov for conducting radiocarbon dating of floodplain seiments and to the reviewers and editors for their valuable comments and suggestions on the content of the article.*

This study was performed in agreement with state assignments of the Institute of the Earth's Crust (no. 121042700218-2) and Sochava Institute of Geography (no. AAAA-A21-121012190017-5), with partial financial support from the Grant of the Government of the Russian Federation no. 0475-15-2021-631 (August 6, 2021) "Baikalian Siberia in the Stone Age: At the Intersection of Worlds".

References

Alexeev S.V., Alexeeva L.P., Kononov A.M., 2014. Cryogenic deformation structures in Late Cenozoic unconsolidated sediments of the Tunka depression in the Baikal rift zone. *Perm. Perigl. Proc.* **25**, 117–126. doi: 10.1002/ppp.1809.

Arzhannikov S.G., Alexeev S.V., Glyzin A.V. et al., 2010. The Late Pleistocene–Holocene climate history in the Western Todzha basin (Eastern Tuva). *Russ. Geol. Geophys.* 51 (2), 163–175.

Dostovalov B.N., Kudryavtsev V.A., 1967. *General geocryology*. Moscow, Izd. Mosk. Gos. Univ., 404 p. (in Russian).

Derevyanko A.P. (Ed.), 2008. *Global and Regional Climate and Environment Changes in the Late Cenozoic in Siberia*. Novosibirsk, Izd. Sib. Otd. Ross. Akad. Nauk, 511 p. (in Russian).

Dugerdil L., Joannin S., Peyron O. et al., 2021. Climate reconstructions based on GDGTs and pollen surface datasets from Mongolia and Baikal area: calibrations and applicability to extremely cold-dry environments over the Late Holocene. *Climate of the Past* **17** (3), 1199–1226. doi: 10.5194/cp-17-1199-2021.

Ershov E.D. (Ed.), 1989. *Geocryology of the USSR*. Vol. 4. Central Siberia. Moscow, Nedra, 414 p. (in Russian).

Ershov E.D. (Ed.), 1998. *Fundamentals of geocryology.* Part 3. *Regional and Historical Geocryology of the World*. Moscow, Izd. Mosk. Gos. Univ., 575 p. (in Russian).

Fotiev S.M., 2005. Modern concepts of the evolution of cryogenic region of Western and Eastern Siberia in the Pleistocene and Holocene (Communication 1). *Kriosfera Zemli* IX (2), 3–22 (in Russian).

Fotiev S.M., 2006. Modern concepts of the evolution of cryogenic region of Western and Eastern Siberia in the Pleistocene and Holocene (Communication 2). *Kriosfera Zemli* X (2), 3–26 (in Russian).

Fotiev S.M., 2009. Geocryological annals of Siberia. *Kriosfera Zemli* XIII (3), 3–16 (in Russian).

Geocryological Glossary. Moscow, GEOS, 2003, 140 p. (in Russian).

Jambaljav Ya., Gansukh Ya., Temuujin X. et al., 2016. *Permafrost Distribution Map of Mongolia*. Ulaanbaatar, Gazriin Zurag LLC, 2016, 1 p.

Klinge M., Sauer D., 2019. Spatial pattern of Late Glacial and Holocene climatic and environmental development in Western Mongolia – A critical review and synthesis. *Quater. Sci. Rev.* **210**, 26–50. doi: 10.1016/j.quascirev.2019.02.020.

Konstantinov M.V., 1994. *Stone Age of the Eastern Region of Baikal Asia*. Ulan-Ude; Chita, Izd. BSC SB RAS and ChSPI, 180 p. (in Russian).

Konstantinov M.V., Ekimova L.V., Vereshchagin S.B., 2016. *Taiga Chikoy at the Turn of Stone and Bronze*. Chita, Izd. TSU, 247 p. (in Russian).

Lehmkuhl F., Hilgers A., Fries S. et al., 2011. Holocene geomorphological processes and soil development as indicator for environmental change around Karakorum, Upper Orkhon Valley (Central Mongolia). *Catena* **87**, 31–44. doi: 10.1016/j.catena.2011.05.005.

Levi K.G., 2014. Little Ice Age. Part 1. Cosmic and global meteorological aspects. *Izvest. Irkutsk Gos. Univ., Ser. Geoarkheolog. Etnolog. Antropolog.* **8**, 2–14 (in Russian).

National Atlas of Russia. Vol. 2. *Nature and Ecology,* 2007. Moscow, Roskartografiya, 495 p. (in Russian).

Ravskii E.I., 1972. *Sedimentation and Climates of Inner Asia in the Quaternary*. Moscow, Nauka, 336 p. (in Russian).

Reimer P.J., Austin W.E.N., Bard E. et al., 2020. The IntCal20 northern hemisphere radiocarbon age calibration curve (0–55 cal kBP). Radiocarbon **62** (4), 725–757. doi: 10.1017/RDC.2020.41.

Romanovskii N.N., 1977. *Formation of Cryogenic Polygonal Wedge Structures*. Novosibirsk, Nauka, 215 p. (in Russian).

Romanovskii N.N., 1993. *Fundamentals of Cryogenesis of the Lithosphere*. Moscow, Izd. Mosk. Gos. Univ., 336 p. (in Russian).

Ryzhov Yu.V., Golubtsov V.A., 2018. Cryogenesis and development of erosional landforms in the forest-steppe landscapes of the Selenga midlands in the Late Glacial and Holocene. *Geomorfologiya,* no. 2, 88–97. doi: 10.7868/S0435428118020074 (in Russian).

Ryzhov Yu.V., Golubtsov V.A., 2021. Paleocryogenesis and erosional landform development in the Baikal region, Siberia, during the second half of the Late Pleistocene and the Holocene. *Archaeol. Res. in Asia*, **26**, 100277. doi: 10.1016/j.ara.2021.100277.

Scientific and Applied Reference Bool on Climate of the USSR. Ser. 3. *Long-term data*. Parts 1–6. Iss. 23. *Buryat ASSR, Chita Region,* 1989. Leningrad, Gidrometeoizdat, 550 p. (in Russian).

Tarasov P., Bezrukova E., Karabanov E. et al., 2007. Vegetation and climate dynamics during the Holocene and Eemian interglacials derived from Lake Baikal pollen records. *Palaeogeogr. Palaeoclimatol. Palaeoecol.* **252**, 440–457. doi: 10.1016/j.palaeo.2007.05.002.

Tseytlin S.M., 1979. *Geology of the Paleolithic of North Asia*. Moscow, Nauka, 288 p. (in Russian).

Vorob'eva G.A., 2010. *Soil as a Chronicle of Natural Events in the Baikal Region: Problems of Evolution and Classification of Soils*. Irkutsk, Izd. Irkutsk Gos. Univ., 205 p. (in Russian).

Wang W., Feng Z.-D., Lee et al., 2004. Holocene abrupt climate shifts recorded in Gun Nuur Lake core, northern Mongolia. *Chinese Sci. Bull.* **49** (5), 520–526. doi: 10.1360/03wd0264.

Wanner H., Solomina O.N., Grossjens M. et al., 2011. Structure and origin of Holocene cold events. *Quater. Sci. Rev.* **30**, 3109–3123. doi: 10.1016/j.quascirev.2011.07.010.

Received April 30, 2021
Revised February 13, 2022
Accepted December 9, 2022

Translated by M.A. Korkka

EARTH'S CRYOSPHERE
SCIENTIFIC JOURNAL

Earth's Cryosphere, 2023, vol. XXVII, No. 1, pp. 12–20

PHYSICAL AND CHEMICAL PROCESSES IN FROZEN GROUND AND ICE

RESULTS OF PHYSICAL MODELING OF SOIL FREEZING

V.G. Cheverev[1,*], A.V. Brushkov[1], E.V. Safronov[1], Yu.A. Kaynov[2], A.L. Fedotov[2]

[1] *Lomonosov Moscow State University, Leninskie Gory 1, Moscow, 119991 Russia*
[2] *Research Institute of Pipeline Transport, Sevastopolsky prosp. 47a, Moscow, 117186 Russia*

**Corresponding author; e-mail: cheverev44@mail.ru*

The article presents the results of physical modeling of soil freezing in laboratory. The samples of silty clay of kaolinite composition were used as model soil. The main characteristics of the component and phase composition of water, as well as the heat and mass transfer and deformation properties of the soil were experimentally determined. During the physical modeling, parameters of the freezing process, differential heaving of frozen and shrinkage of thawed zones, heat and moisture transfer, and pore pressure were monitored. The appearance of segregated ice in the freezing soil, layered axial and horizontal deformation, and the dynamics of density and water content of water-saturated soil samples over time were determined using position markers and time-lapse video.

Keywords*: physical modeling, freezing, heaving, characteristics of silty clay, process parameters.*

Recommended citation: Cheverev V.G., Brushkov A.V., Safronov E.V., Kaynov Yu.A., Fedotov A.L., 2023. Results of physical modeling of soil freezing. *Earth's Cryosphere* XXVII (1), 12–20.

INTRODUCTION

Frost heaving of freezing soils is a widespread dangerous geocryological process for buildings and engineering structures in the permafrost region of Russia [*Garagulya et al., 2000*]. In this regard, the forecast and management of this process are relevant.

Currently, despite many years of studies into the mechanism and regularities of the heaving process, the problem of developing a mathematical forecast of this process is still far from a final solution. The existing models of heat and mass transfer and deformations for numerical forecasting of soil freezing and heaving have not yet found experimental confirmation in terms of quantitative compliance.

For mathematical modeling of the freezing and heaving process, a physical formulation of the problem is relevant, if it takes into account the essential factors of the processes that take place when testing homogeneous samples with fixed boundary conditions. Currently, it is advisable to conduct research under simpler conditions than those that occur in nature, that is, not to take into account the heterogeneity of soils and the variability of external thermodynamic conditions.

The totality of the essential elements of the system and the parameters of the freezing process should be divided into three groups: (a) internal characteristics (mineralogical composition, organic matter content, grain size, density, porosity, total water content, unfrozen water content, ice content, chemical composition and ionic strength of the pore solution; thermal, mass transfer, and mechanical properties); (b) external factors (the nature of heat exchange and mass transfer, mechanical, hydraulic, and pneumatic effects on the freezing soil and ways to set them in the experiment); and (c) the observed parameters of internal processes of freezing and heaving (temperature and pore pressure distribution, thermal and mass flows, the nature of deformations and ice release, and so on).

CHARACTERISTICS OF KAOLINITE CLAY AS A MODEL SOIL

For physical modeling, a pulverized kaolinite clay was chosen, because of the fact that it is a striking representative, even a standard, in a series of heaving soils. The results of determining the particle-size and microaggregate-size compositions, analysis of water extract, moisture conductivity coefficients, and thermal conductivity of kaolinite clay in thawed and frozen states, as well as the unfrozen water content and starting point of freezing are presented in Tables 1–3 and, Fig. 1. The maximum molecular water capacity of kaolinite clay W_{MWC} is 20.6%; the liquid limit W_L is 45.8%; the plastic limit W_ρ is 34.0%; the plasticity index I_ρ is 11.8%; the solid phase density ρ_s is 2.72 g/cm^3; the initial water content W is 42%; and the compression load is 0.3 MPa. Methods for determining special characteristics (except for the routine methods for determining particle-size distribution and composition of water extract) are described in [*Cheverev, 2004*].

Table 1. **Particle-size and microaggregate-size (in parentheses) distributions in the kaolinite clay sample**

Geol. symbol	Sampling site	Fraction size, mm; fraction content, %								Texture (V.V. Okhotin's classification)
		>0.5	0.5–0.25	0.25–0.1	0.1–0.05	0.05–0.01	0.01–0.005	0.005–0.001	<0.001	
eP_2	Chelyabinsk region, Novokaolinovyi city	0.7 (1.5)	0.5 (0.2)	0.4 (0.2)	2.9 (1.2)	19.5 (32.2)	11.2 (24)	40.2 (34.5)	24.6 (6.2)	Silty clay

Table 2. **Analysis of water extract from kaolinite clay**

pH	Ion content, meq/100 g clay							TDS, %
	HCO_3^-	Cl^-	SO_4^{2-}	Ca^{2+}	Mg^{2+}	K^+	Na^+	
6.9	0.125	0.075	0.407	0.100	0.100	0.019	0.370	0.051

Table 3. **Dependence of the freezing temperature of water-saturated kaolinite clay on density and water content**

Sample no.	Weight water content, u.f.	Density, g/cm^3	Temperature of the beginning of freezing, °C
1	0.36	1.82	–0.26
2	0.39	1.78	–0.24
3	0.42	1.76	–0.16

Figure 1 demonstrates that the dependence of the moisture content of kaolinite clay due to unfrozen water is of a standard character. The temperature of the beginning of freezing depends on the density of the clay and naturally decreases with clay compaction (Table 3).

The analysis of the dependence of the thermal conductivity of clay on the temperature during the transition from the thawed to the frozen state of the soil and back is more complex. In the positive area, the dependence is linear, since it is completely determined by the linear dependence of the thermal conductivity of water on temperature (Fig. 2).

Further, as the soil cools, beginning from the start point of the clay freezing, the appearance of ice due to a decrease in the specific water content significantly increases the thermal conductivity to a peak value. This is due to a fourfold increase in the thermal conductivity of ice (2.2 W/(m·K)) relative to water (0.55 W/(m·K)).

Further cooling from temperature of the completion of the intensive phase transition of water in the clay pores into ice leads to a decrease in thermal conductivity, which is explained by the formation of microcracks.

The temperature reversal, when approaching the area of intense phase transitions, leads to the filling of microcracks of frozen soil with unfrozen water, which restores the high values of thermal conductivity. With a further increase in the temperature of frozen clay, the decrease in thermal conductivity occurs due to a sharp drop in the ice content of the soil and an increase in the content of unfrozen water.

Figure 3 shows the dependences of the moisture conductivity of kaolinite clay in the thawed state on the gradient of pore (hydraulic) water pressure. The method of determination is described in detail in [*Cheverev, 2004*]. Experimental data indicate that, upon small gradients of hydraulic pore pressure (less than 87 m/m), there is a threshold gradient of mois-

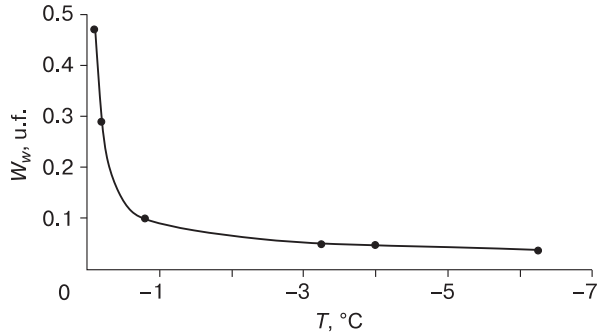

Fig. 1. Dependence of the unfrozen water content of (W_w) frozen silty clay of kaolinite composition on temperature (T) determined by desorption method [*Cheverev et al., 2005*].

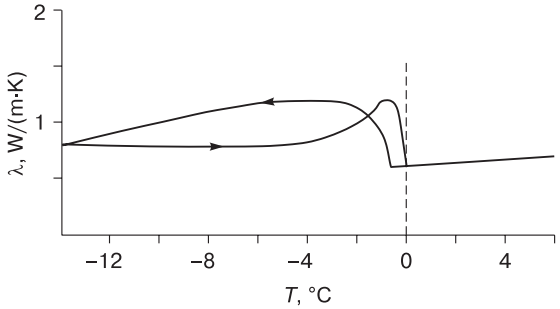

Fig. 2. Dependence of the thermal conductivity coefficient (λ) on the temperature (T) of water-saturated kaolinite clay in the freezing–thawing cycle as determined by the method of stationary thermal regime [*Cheverev, 2004*].

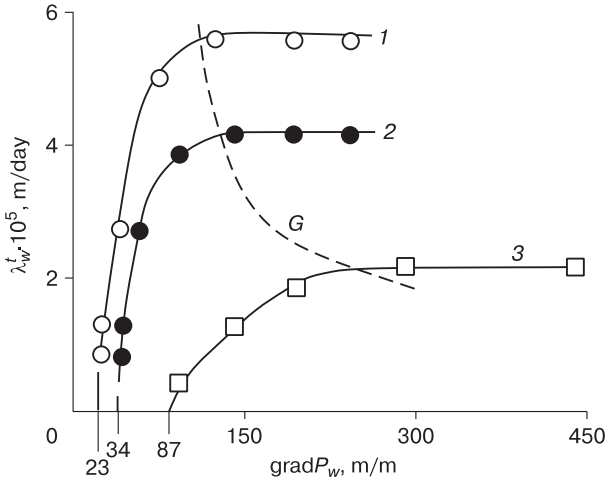

Fig. 3. Dependence of the moisture conductivity coefficient of thawed kaolinite clay (λ_w^t) on the pore pressure gradient (grad P_w) at different densities ρ_d:

(*1*) 1.24, (*2*) 1.3, and (3) 1.42 g/cm^3. *G* is the grad P_w boundary between the linear and nonlinear moisture transfer law.

ture transfer of pore water. As can be seen from the experimental data, the threshold gradient increases with compaction of the clay, namely: at a density of 1.24 g/cm^3, 23 m/m; at 1.30 g/cm^3, 34 m/m; and at 1.42 g/cm^3, 87 m/m. With an increase in the pressure gradient (pressure), the moisture conductivity of clay increases reaching a constant value at pressure gradients characteristic of a particular clay, its temperature and density, and only then Darcy's linear law begins to be fulfilled.

In the frozen zone of the freezing soil, non-compliance with Darcy's law within the limits of the accuracy of determination has not been experimentally established (Fig. 4). In the freezing zone of the soil, a change in the temperature gradient and, accordingly, the pore pressure gradient, while maintaining the average temperature, does not change the proportionality of the cryogenic migration flow density and the pore pressure gradient calculated by Eq. (1).

$$I_w = \lambda_w \, \text{grad} \, P_w, \qquad (1)$$

where λ_w is the soil moisture conductivity coefficient, m/s; I_w is the flow density of cryogenic water migration in the soil, m/s; grad P_w is the gradient of hydraulic pore pressure, m/m. Pressure P_w is measured in meters of water column (1 atm. is equal to 10.33 m of the water column). This pressure dimension is more convenient than Pa and is widely used in agrophysics in describing the thermodynamics of soil moisture and in hydrogeology.

With a decrease in the temperature of clay in the negative area, the moisture conductivity decreases sharply, qualitatively corresponding to the dependence of soil moisture due to the unfrozen water content on temperature [*Cheverev, 2004*].

METHODS OF PHYSICAL MODELING

The purpose of the experimental studies was to examine the parameters of freezing and heaving of soils by laboratory physical modeling. The obtained data were later used to describe the physical formulation of the problem of mathematical modeling of the process taking into account heat and mass transfer and its verification by a preliminary one-dimensional mathematical model [*Cheverev et al., 2021a,b*].

The task of experimental studies was to determine the boundary conditions of the process of freezing and heaving of clay, the dynamics of the temperature field, the movement of the freezing front, the flow of cryogenic migration, deformation of the frost heaving of the freezing zone and shrinkage of the thawed zone, and the parameters of the formation of cryogenic texture recorded by time-lapse video.

The process parameters and characteristics of the clay were set as follows: one-dimensional freezing with fixed boundary conditions for temperature and with an open system for moisture exchange, initial

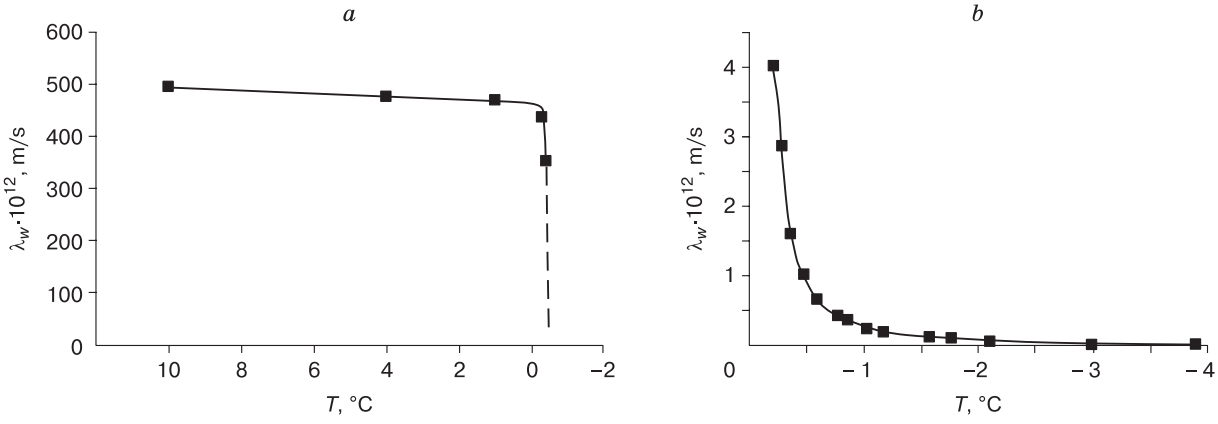

Fig. 4. Dependence of the moisture conductivity coefficient (λ_w) of kaolinite clay in (*a*) thawed and (*b*) frozen states on temperature (*T*).

density and humidity as dependent characteristics of the freezing soil with a full degree of pore filling.

The parameters and characteristics determined were: the distribution of temperature (T) in height and time, pore pressure (P_w), shrinkage and heaving deformation (H_y, H_p), the specific content of unfrozen water (W_w), and the type of cryogenic structure.

To achieve this objective, an automated device was used, the main distinguishing feature of which, giving a significant positive effect, is that soil samples are frozen from the bottom up, and the water supply comes from the top down. A similar scheme of freezing was previously substantiated and successfully used in [*Penner, 1986; Cheverev, 2004; Cheverev et al., 2013*]. In this case, an external load is applied from above from the side of the thawed zone (Fig. 5).

Further, in the description of the equipment, the substantiation of the validity of the application of the proposed methodology for determining the characteristics of frost heaving of soils, including the case of freezing from below, is given.

The device for physical modeling of freezing and heaving of soil (Fig. 5) has the shape of a sleeve with a removable bottom; the soil sample is placed into it. At the upper end of the sample, a capillary-porous stone is placed in an inverted glass with the bottom equipped with a fitting for supplying water and forming pressure in it, unlike atmospheric pressure, in one direction or another, if necessary.

For layer-by-layer measurement of deformations, needle position sensors are installed into the soil at 10 × 10 mm grid. The location of needle position sensors is fixed in time during video shooting. Strain gauges for measuring negative pore pressure in the thawed zone of freezing soil are introduced through the side wall of the sleeve. The strain gauges with a ceramic porous disk and a tube filled with degassed water are provided from the end. The device also includes cooling and load systems not shown in the figure, as well as a control and management automation unit.

The device works as follows. A soil sample is loaded into the sleeve, in the side wall of which, according to a 1 × 1 cm stencil, needle-position sensors are placed to track changes in the density and water content of the soil sample. A capillary-porous stone saturated with water (burnt carborundum or sintered fine-grained sand) is supplied to the soil sample in the glass. A preset load is applied to the bottom of the glass. A water supply system is connected to the fitting for the water supply of the sample through a porous stone.

Water in a porous stone during the experiment is guaranteed to be in a capillary-suspended state. This excludes its gravitational runoff into the soil sample. At the same time, both increased and decreased pressure can be supplied through the fitting, simulating both the pressure of the aquifer and the hydraulic resistance of the thawed zone, or neutral atmospheric pressure, which is equal to zero. Such boundary conditions are possible in nature during soil freezing and therefore were provided by the construction.

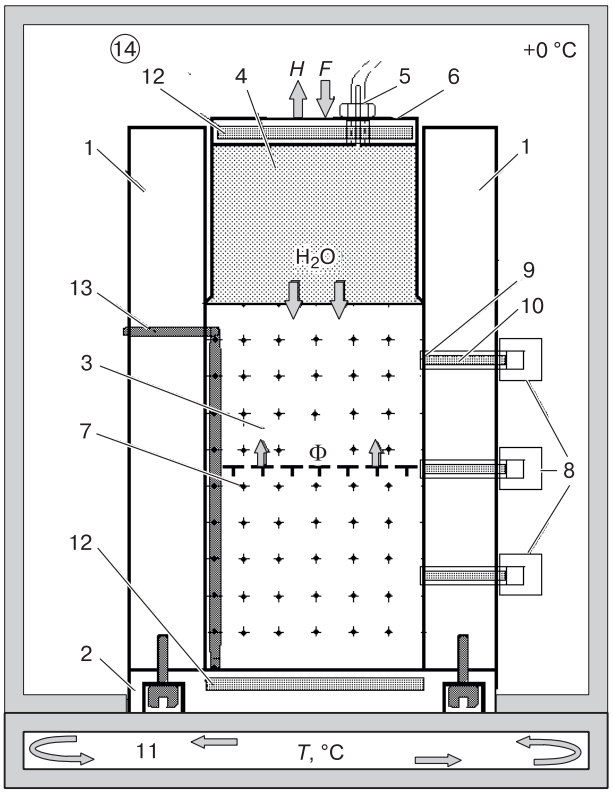

Fig. 5. A device for physical modeling of freezing and heaving of soil with control of boundary conditions and determination of process parameters.

1 – sleeve, 2 – bottom of the sleeve, 3 – soil sample, 4 – capillary-porous stone (or fine-grained sand), 5 – fitting for supply of water and pressure formation in it, 6 – bottom of the cup, 7 – position sensors (tags), 8 – strain gauges of pore hydraulic pressure, 9 – ceramic porous disk at the end of the sensor, 10 – tube with degassed water, 11 – cooling (freezing) zone, 12 – heat flow sensor, 13 – string of thermal sensors, 14 – zero temperature zone; H – heaving vector, F – static load vector, F – freezing front position, H_2O – water in capillary-saturated sand; arrows indicate the direction of water movement into the freezing sample from an external source.

To control the movement of the freezing front in the ground, a garland of thermal sensors is installed on the inside of the sleeve.

The load on the freezing soil sample is carried out through the force sensor by the pneumatic drive unit. Pressure control is carried out by the automated control system. The total pressure in the system is created by means of a compressor.

The theoretical substantiation of the applicability of determining the degree of frost heaving of the soil by freezing the test sample from below is supported by comparative experiments [*Cheverev et al., 2013*].

RESULTS OF PHYSICAL MODELING

Figure 6, as an example, presents the results of freezing the same sample of kaolinite powdery clay obtained during testing with time-lapse shooting: at the beginning of the experiment 0 h and after 20 h.

Moisture-saturated samples of kaolinite clay with the water content of 42% were prepared for the experiment. The samples were placed in sleeves having a parallelepiped shape, in which they were compacted at a load of 0.3 MPa during a week before freezing.

Four freezing experiments were carried out: experiments 2, 3, 4 and 5; each sample during the test had its own characteristics in terms of boundary conditions. In the case of experiment 2, the temperature at the upper and lower ends of the sample was maintained constant (+2 and –1.5°C, respectively) for 36 h; after this, the conditions were changed and new values were set: +1.7 and –3°C, respectively. The remaining experiments did not have such significant changes: for experiment 3, these temperatures were +0.9 and –3.2°C, respectively; for experiment 4, +0.9 and –4.9°C; for experiment 5, +0.5 and –7°C. Unlimited water supply was carried out to the samples, except for experiment 3. In the latter experiment, it was decided to leave for heaving only the volume of moisture that was in the layer of water-saturated sand from above, holding it due to capillary forces. In addition, the samples had different initial heights: experience 2, 150 mm; 3, 121 mm; 4, 103 mm; and 5, 121 mm.

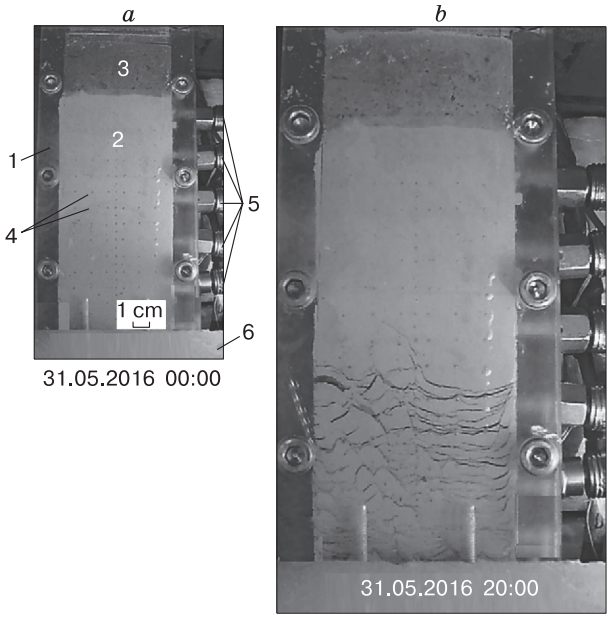

Fig. 6. Experiment 2. Kaolinite clay sample before freezing (*a*) and 20 hours after freezing (*b*).

1 – sleeve, 2 – kaolinite clay sample, 3 – fine-grained sand capillary-saturated with water, 4 – position sensors (tags), 5 – pore pressure sensors, 6 – cooling thermal plate.

During the experiments, pore pressure was measured using built-in sensors along the height of the sleeve, temperature and heat flow density were measured at the upper and lower ends of the sample (Fig. 6).

To track the evolution of the cryogenic structure. the course of the experiment was continuously recorded on the camera. Examples of such evolution during the experiment with an open moisture exchange system at the initial water content of 42% are presented in Fig. 7.

By using time-lapse video recording, the dynamics of segregation ice formation in the freezing soil, layered axial and horizontal deformation (heaving and shrinkage), as well as the dynamics of density and water content of the sample over time. along the height and width of the sample, were obtained. During the cooling of the clay sample, the rate of the freezing front movement naturally slows down, since the temperature gradient decreases with an increase in the height of the frozen zone under fixed boundary conditions.

As a result, the optimum freezing rate for the formation of the largest ice layers and heaving (0.01–0.02 m/day). The cryogenic structure gradually changes from massive and fine-grained to medium- and large-grained. With the maximum deceleration of the movement of the freezing front, the largest ice lenses grow; when the critically low speed of the front movement is reached, the growth of the lenses near it stops. This conclusion logically follows from the established fact that at small gradients of pore pressure (less than 87 m/m) there is a threshold gradient of moisture transfer of pore water (Fig. 3). As a result, cryogenic migration to the freezing front stops. Further extremely slow cooling of the soil may be accompanied by the formation of only a massive cryogenic structure.

Tracing the layered axial and horizontal deformation, as well as the dynamics of the sample density over time, in height and width of the sample showed the following. In the freezing soil, the outflow of water from the thawed zone into the frozen zone causes a decrease in pore pressure in it. As a result, the thawed zone experiences volumetric shrinkage. During freezing, the shrinkage zone lengthens and becomes the zone of transit transfer of water from an external source to the freezing zone. In this case, the density and water content of the shrinkage limit is achieved, which is close to the lower limit of plasticity of kaolinite clay [*Cheverev, 2004*].

As the height of the samples was different, different values given were used as evaluation characteristics. For example, Fig. 8 presents the results of changes in the relative deformation of samples over time (e), which was calculated by the formula:

$$e = (H - H_0)/H_0,$$

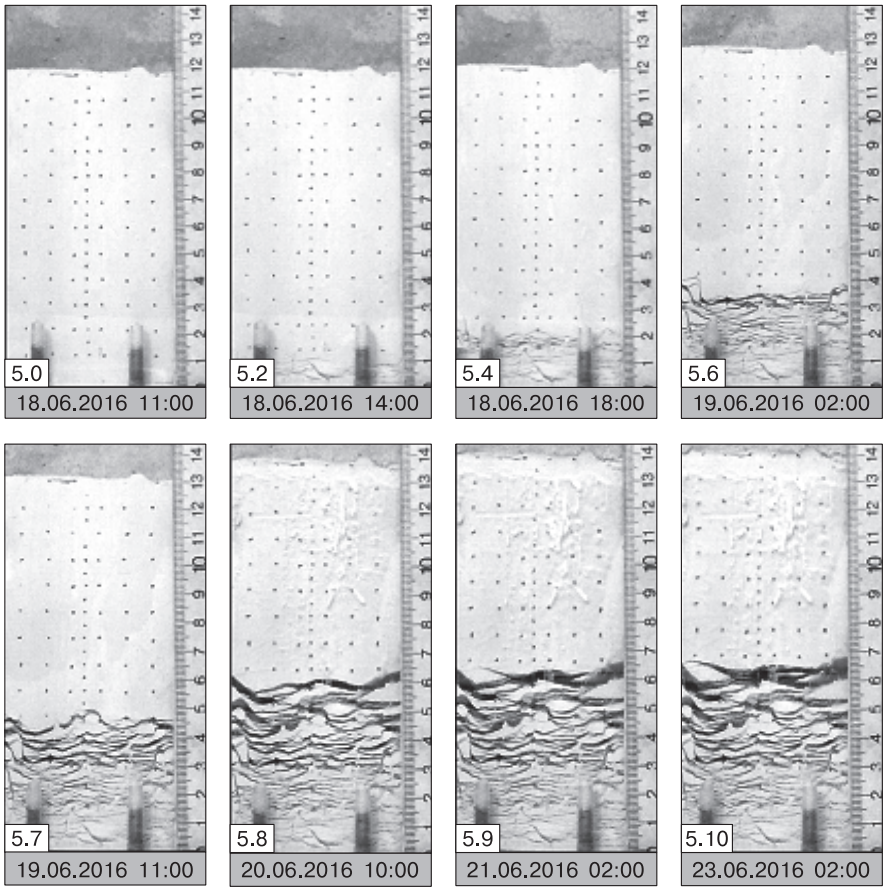

Fig. 7. Experiment 5. Fragments of the dynamics of cryogenic structure formation in a sample of kaolinite clay at different points in time.

5.0–5.10, laboratory numbers of time-lapse photos. State of the sample before the beginning of freezing at 11 a.m. on June 18, 2016.

where H_0 is the height before freezing, and H is the height during freezing.

The change in the height of the frozen layer over time was calculated on the basis of camera data, on which the boundary of the thawed and frozen zones was clearly visible even in the absence of ice lenses in the transition zone ("freezing edge"), where the massive cryogenic structure is observed: the frozen part of the soil sample in the vicinity of the freezing front was darker compared with the thawed part.

Figure 9 shows the change in the proportion of the frozen part of the total height of the freezing samples over time.

Tracking the frozen part made it possible to calculate the relative heaving deformation (ε_{fh}) of samples over time (Fig. 10) using the formula:

$$\varepsilon_{fh} = h_f/d_i,$$

where h_f is the vertical deformation of the soil sample at the end of the test, mm; d_i is the thickness of the frozen layer of the soil sample minus h_f, mm.

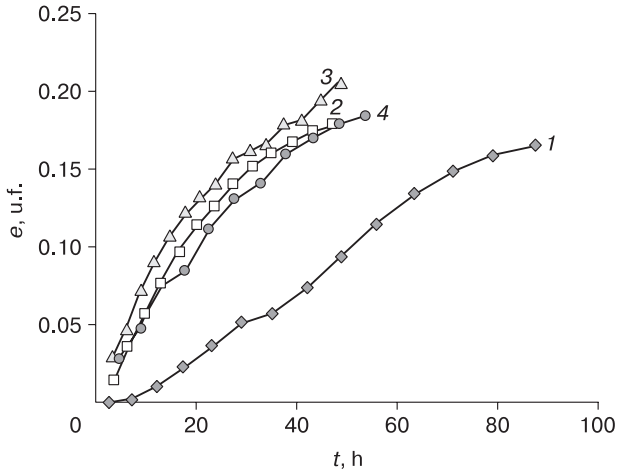

Fig. 8. Change in the relative deformation of freezing samples (e) over time (t) under different temperature boundary conditions.

1 – experiment 2, T = +2, –1.5°C up to 30 h and T = +1.7, –3°C after 36 h; *2* – experiment 3, T = +0.9, –3.2°C; *3* – experiment 4, T = +0.9, –4.9°C; *4* – experiment 5, T = +0.5 и –7°C.

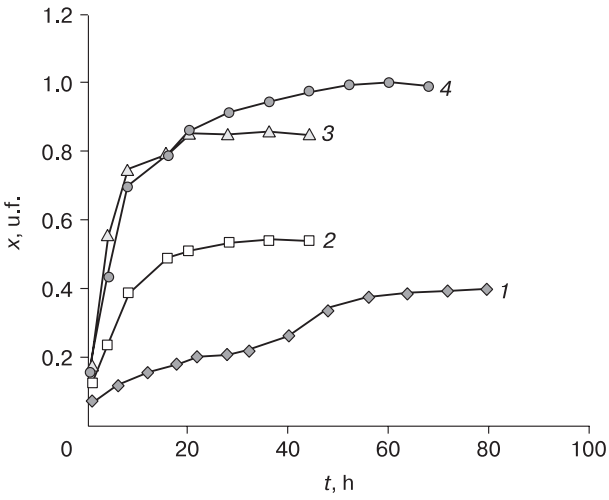

Fig. 9. Change in the relative fraction of the frozen part from the total height of the freezing samples (x) over time (t) under different boundary conditions.

(*1–4*) see Fig. 8.

In Fig. 9, one can note a significant acceleration of the freezing process and an increase in the proportion of the height of the frozen part in the sample, when the boundary conditions change from the cold part towards lower temperatures. Interestingly, the dynamics of deformation of a freezing sample with the lowest temperature of the cold zone –7°C (experiment 5), as can be seen from Fig. 8, is comparable with freezing samples at a higher corresponding boundary temperature (experiments 3 and 4), while the freezing sample in experiment 2 with the highest boundary temperatures is noticeably behind them.

At the same time, the sample in experiment 5 has the lowest dynamics of heaving, and the sample in experiment 2 has the highest one (Fig. 10). This is primarily due to the fact that the sample in experiment 5 froze much faster than in experiment 2 (Fig. 9). As a result, due to too fast freezing, the high initial values of the water flow in the ground in experiment 5 were leveled and rapidly decreased, while the value of the water flow in experiment 2 kept a high value (Fig. 11).

The dynamics of freezing of the sample in experiment 5, as the authors believe, is associated with the prevailing expansion of the soil in this case due to the freezing of water that was in its pores initially. The contribution to the expansion of the soil in this experiment due to the growth of ice lenses is minimal in comparison with other samples, which is further confirmed by the low values of the water flow during the test (Fig. 11). At the same time, for the sample in experiment 2, in the "warmest" conditions, the contribution to the expansion of the soil due to the growth of ice lenses plays the dominant role, which is reflected in Figs. 10 and 11.

Figure 12 shows graphs of changes in heat fluxes over time (I_q), with "cold" and "warm" denoting the lower and upper ends of the sample, respectively.

The heat flow density was measured at the upper and lower ends of the sample, while negative temperature was applied to the lower end, and positive temperature was applied to the upper end.

The pore pressure sensors in the samples worked stably only for the first 6 to 9 h, and this is normal. During this time, bubbles gradually formed inside the sensors due to a decrease in pressure from the air dissolved in water, after which the sensor could not correctly measure the pore pressure. The lower the pres-

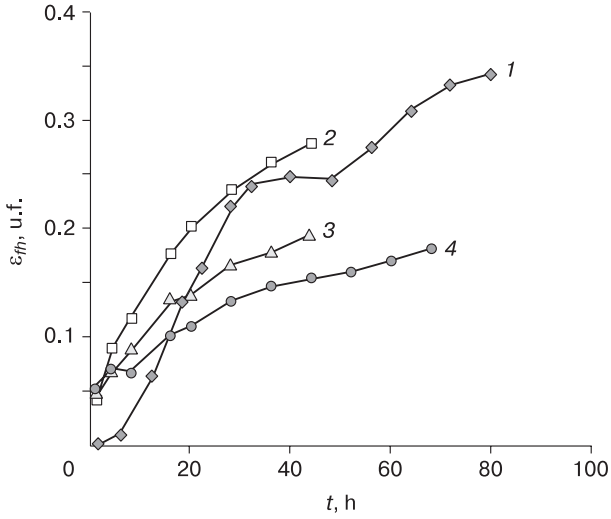

Fig. 10. Changes in the relative heave deformation (ε_{fh}) of samples over time (t) under different boundary conditions.

(*1–4*) see Fig. 8.

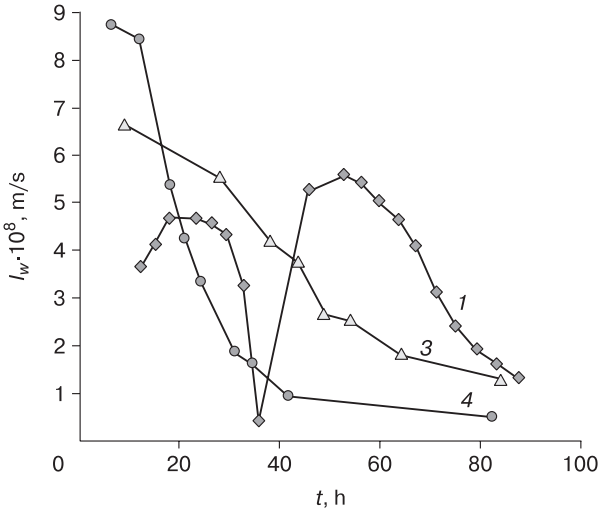

Fig. 11. Changes in the soil water flow density (I_w) in the samples as a function of time (t) under different boundary conditions.

(*1–4*) see Fig. 8.

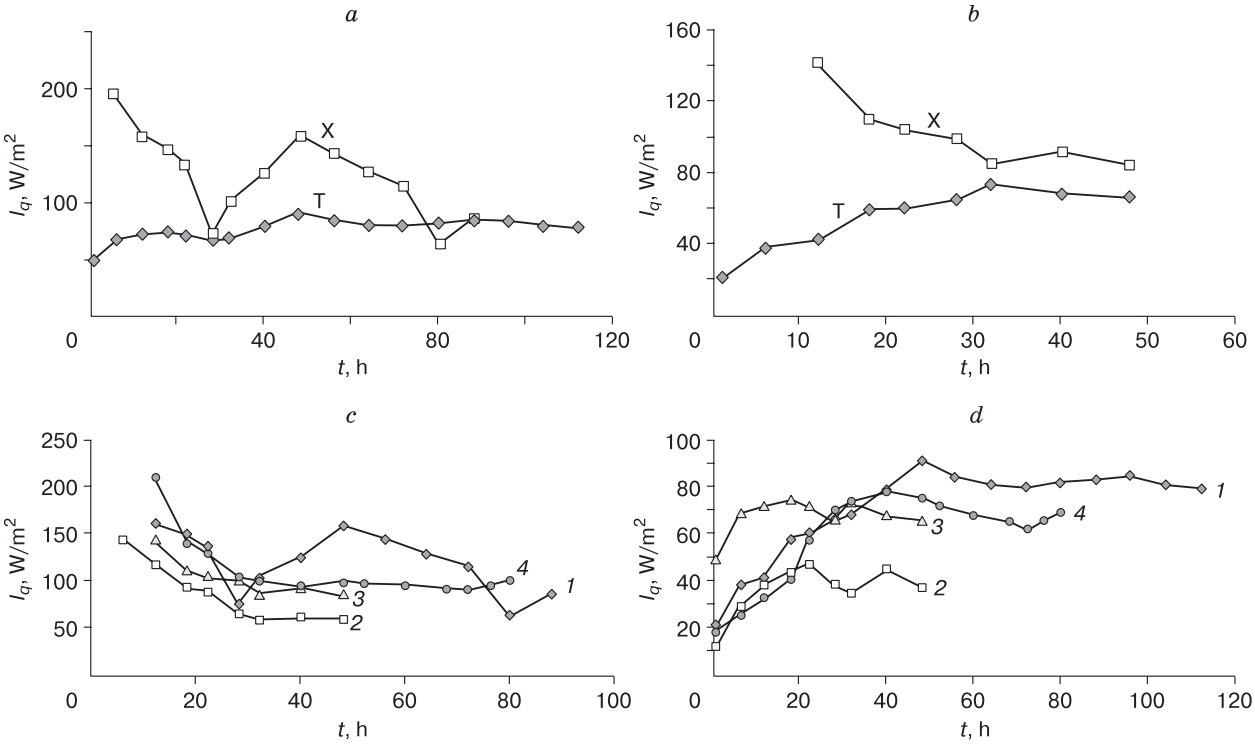

Fig. 12. Changes in the density of heat fluxes (I_q) over time (t) in the freezing kaolinite clay sample:

(a, b) heat fluxes at the warm (T) and cold (X) ends during freezing of the sample in experiments 2 and 4, respectively; (c) heat fluxes at the warm end face; and (d) heat fluxes at the cold end face. (*1*–*4*) see Fig. 8.

sure, the faster this process. When the sensor froze, the reverse process occurred, that is, the freezing of water in the sensor increased the pressure in it to 12 atm or more. That is, for this type of sensors made of baked kaolinite clay, there is a natural measuring range of negative pressure no lower than –0.8 atm. To measure lower pressures, as well as for measurements in saline freezing soils, it is necessary to use osmometers, which, unfortunately, are not yet technically developed enough to measure pore pressure in freezing soils.

As can be seen from the experimental data (Fig. 13), the distribution of pore pressure along the height of the freezing soil in its thawed zone is close to linear, which indicates the filtration mechanism of moisture transfer.

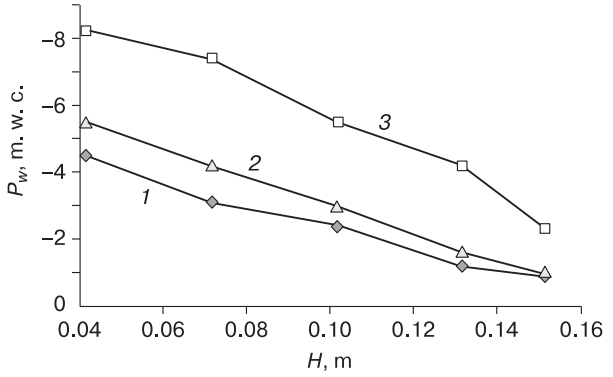

Fig. 13. Pore pressure profile in the thawed zone (P_w) by the height (H) of the kaolinite clay sample at different time moments during freezing (experiment 2).

1 – 1 h, *2* – 3 h, and *3* – 6 h.

CONCLUSIONS

1. Physical laboratory modeling of the freezing of kaolinite clay composition, which belongs to strongly heaving soils, was performed. The main characteristics of the component and phase composition of water in the model clay, as well as its heat and mass transfer and deformation properties were determined. During the physical modeling, the parameters of the freezing process, differential heaving of frozen and shrinkage of thawed zones, heat and moisture transfer and pore pressure of water were monitored.

2. By using time-lapse video, the dynamics of segregation ice release in the freezing ground, layered axial and horizontal deformation (heaving and shrinkage), as well as the dynamics of the density (moisture content) along the sample height over time were revealed.

3. A change in the boundary conditions, namely a sudden decrease in temperature from the cold source, first led to a sharp slowdown in the deformation and heaving of the sample and the process of moisture transfer to the freezing front, and then, conversely, accelerated these processes.

4. The freezing of samples in a certain range of boundary conditions led to comparable dynamics of the heaving of samples; however, the freezing rates varied significantly, which ultimately resulted in different final heaving deformation after the freezing front in the sample was practically stopped.

5. The filtration mechanism of moisture transfer in the thawed zone of the freezing highly porous soil was experimentally confirmed.

Acknowledgments. *The materials for this paper were obtained with financial support of Transneft Research Institute LLC (contract no. 4220 P/20-511/2015 from November 19, 2015.*

References

Cheverev V.G., 2004. *The Nature of Cryogenic Properties of Soils.* Moscow, Nauchnyi mir, 234 p. (in Russian).

Cheverev V.G., Brushkov A.V., Polovkov S.A. Pokrovskaya E.V., Safronov E.V., 2021a. Analysis of concepts on the mechanism of cryogenic water migration in freezing soils. *Earth's Cryosphere* XXV (5), 3–10.

Cheverev V.G., Burnaev R.S., Gagarin V.E., Safronov E.V., 2013. Influence of the external pressure on the degree of frost heaving of clay soils. *Kriosfera Zemli* XVII (4), 57–62 (in Russian).

Cheverev V.G., Safronov E.V., Korotkov A.A., Cherniatyn A.S., 2021b. Physical formulation of the numerical modeling of freezing and frost heaving of soils with consideration of heat and mass transfer. *Nauka Tekhnol. Truboprovodn. Transp. Nefti Nefterpoduktov* **11** (3), 244–256 (in Russian).

Cheverev V.G., Vidyapin I.Yu., Motenko R.G., Kondakov M.V., 2005. Determination of the content of unfrozen water in soils by sorption-desorption isotherms. *Kriosfera Zemli* IX (4), 29–33 (in Russian).

Garagulya L.S., Buldovich S.N., Romanovsky N.N. et al., 2000. Geocryological hazards. In: *Natural Hazards of Russia*. Moscow, Firm "KRUK", 315 p. (in Russian).

Penner E., 1986. Aspects of ice lens growth in soils. *Cold Reg. Sci. Technol.* **13**, 91–100.

Received July 5, 2022
Revised December 12, 2022
Accepted December 19, 2022

Translated by S.B. Sokolov

Earth's Cryosphere, 2023, vol. XXVII, No. 1, pp. 21–29

DIELECTRIC METHOD FOR MEASURING THE CONTENT OF UNFROZEN WATER IN MINERAL SOIL

A.Yu. Karavayskiy[1,*], Yu.I. Lukin[1], E.I. Pogoreltsev[1,2]

[1] *Kirensky Institute of Physics, Siberian Branch of the Russian Academy of Sciences, Akademgorodok 50/38, Krasnoyarsk, 660036 Russia*
[2] *Institute of Engineering Physics and Radio Electronics, Siberian Federal University, Kirenskogo St. 28, Krasnoyarsk, 660074 Russia*

**Corresponding author; e-mail: rsdak@ksc.krasn.ru*

The possibility of using the dielectric method to determine the unfrozen water content in the frozen natural mineral soil was proved by establishing the relationship between the contents of soil water forms measured by the dielectric, calorimetric, and contact methods. The unfrozen water content in the sample was measured by the calorimetric and contact methods. In the dielectric method, it was estimated by measuring the maximum content of bound water. The unfrozen water content measured by the calorimetric method in the soil samples with different initial water contents varied within 17%. The unfrozen water content measured by the contact method and the bound water content determined by the dielectric method were within the ranges of values determined by the calorimetric method. The values of the bound water content obtained by the dielectric method and the unfrozen water content obtained by the contact method differed by no more than 17%.

Keywords: *mineral soils, calorimetric method, permittivity, unfrozen water, bound water, unbound water.*

Recommended citation: Karavayskiy A.Yu., Lukin Yu.I., Pogoreltsev E.I., 2023. Dielectric method for measuring the content of unfrozen water in mineral soil. *Earth's Cryosphere* XXVII (1), 21–29.

INTRODUCTION

The measurement of soil moisture is of interest to many areas of economic and scientific activity, such as agriculture, forestry, and meteorology. Electromagnetic methods are widely used to measure the water content in soil [*Lesaignoux et al., 2013; Lekshmi et al., 2014; Bobrov et al., 2019; Muhammad, Almushfi, 2020*]. Most electromagnetic methods for measuring the water content in soil use data on the dependence of complex permittivity (CP) on moisture in the kilohertz and gigahertz frequency ranges of the electromagnetic field [*Pardo Lara et al., 2020; Mavrovic et al., 2021*]. For practical application, on the basis of developed methods, electromagnetic measuring instruments for the water content of unfrozen soils have been developed and are widely used.

Many works note the importance of conducting research to determine the unfrozen water content in frozen soils [*Andrianov, 1936; Ananyan, 1961; Nersesova, Tsytovich, 1963; Tsytovich, 1973; Horiguchi, 1985; Frolov, 1998; Ershov, 2004; Zhang et al., 2010; Kozlowski, 2016; Kuzmin, Sleptsova, 2019; Hu et al., 2020*]. Currently, there are methods that allow measuring the unfrozen water content, e.g., nuclear magnetic resonance (NMR) [*Turov, Leboda, 1999; Watanabe, Mizoguchi, 2002*], calorimetric [*Kozlowski, 2003a, 2007, 2016; Grigoriev, 2020*], and water-potentiometric [*Chuvilin et al., 2020*] methods. There are also methods for determining the content of bound water, which involve measuring the CP of frozen soils [*Fabbri et al., 2006; Mironov, Savin, 2015; Mironov et al., 2018, 2020*]. Desorption [*Cheverev et al., 2005*] and contact methods [*GOST R 59537-2021, 2021*] are used as standard measurement methods. The essence of the desorption method is to determine the equilibrium soil moisture with respect to the vapor phase of a reference solution, for which the freezing point is known. The essence of the contact method is to saturate air-dry soil with water upon contact with ice at a given negative temperature and measure the relative amount of water absorbed by the soil from the moment phase equilibrium is reached.

Each method uses the results of studies of certain physical properties of the soil–water mixture. For example, in calorimetric measurements, thermal properties are studied, by analyzing which it is possible to calculate the amount of water that has experienced a phase transition. Dielectric methods for measuring moisture imply the use of a CP model that takes into account the CP of various forms of soil water: unbound and bound. In frozen soils, unbound water is present in the form of ice. It is known that the relative permittivity (RP) of bound water differs from the RP of ice in frozen soil and unbound water in thawed soil. According to the results presented in [*Mironov, Lukin, 2011*], the real part of the RP of bound water in frozen soil at a frequency of 8 GHz decreased from 90 to 9 during soil freezing. Therefore, it is important to correctly take into account the CP of bound water in dielectric soil models used in moisture meters due to the content of unfrozen water. However, the change in CP of frozen mineral soil with temperature change is not an unconditional sign that bound water remains in a liquid state. Therefore, the possibility of using the dielectric method for the quantitative measurement of unfrozen water in soils requires additional research.

This issue was already considered earlier in [*Mironov et al., 2018*], where joint dielectric and calorimetric studies of Na-bentonite clay were carried out. Using a refractive dielectric model, the authors were able to determine the content of bound water in Na-bentonite clay as a model parameter using dielectric measurements. It was shown that the found content of bound water in frozen Na-bentonite clay coincides within the measurement errors with the unfrozen water content. The authors suggested that this conclusion can be extended to other types of soils, but this assumption requires experimental justification. In the meantime, the approach proposed in [*Mironov et al., 2018*] for determining the content of unfrozen water by the calorimetric method introduces additional errors associated with the delay in recording the heat flow by the measuring device. A somewhat different method for measuring the content of unfrozen water was implemented in [*Kozlowski, 2003a*]. The method proposed in [*Kozlowski, 2003a*] assumes the use of the calorimetric signal data of the entire phase transition process in the calculation of the unfrozen water content. This method makes it possible to find not only the temperature dependence of the unfrozen water content in frozen soil but also the temperature of the end of sample melting, which is also a significant physical characteristic for mineral soils.

This article presents the results of measurements of unfrozen water content by calorimetric, contact, and dielectric methods in the frozen mineral soil of the Yamal Peninsula in order to prove that the dielectric method, along with other methods, can be used to measure the content of unfrozen water in frozen mineral soil.

MATERIALS AND METHODS

Description of samples. The natural mineral soil of the Arctic tundra from the Yamal Peninsula (70°16′52″ N, 68°53′29″ E) was chosen as the study object. The soil sample was taken from a depth of 5–15 cm and belongs to silty clay (sand, 1.6%; silt, 57.1%, clay 41.3%). The mineral composition of the soil (%) is as follows: quartz 60, feldspar 20–25, plagioclase 5, mica and chlorite as accessory minerals, and smectite and amphibole in trace amounts.The study of the soil was carried out for samples with different moisture contents from dry to the field water capacity (the maximum water content retained in the soil by capillary forces). Prior to measurements, the samples of a given moisture content were prepared as follows. The required amount of distilled water was added to the dry soil. The resulting soil-water mixture was hermetically sealed and left for 7 days, so that water could be evenly distributed over the sample, and the added water was adsorbed on the surface of the particles. After this, measurements on the samples were performed.

Table 1. **Characteristics of measured samples**

No.	Weight, mg		Gravimetric water content, g/g	Total amount of heat, mJ
	moistened sample	water,		
1	47.12	2.4	0.054	0
2	50.35	4.37	0.095	231.6
3	42.65	3.9	0.101	308.3
4	47.20	5.3	0.126	421.5
5	60.04	7.56	0.144	1093.3
6	52.15	7.9	0.179	1440.9
7	55.16	9.4	0.205	1859.9
8	64.20	13.0	0.254	2691.3
9	64.41	13.3	0.260	2852.1
10	57.93	12.53	0.276	2934.7
11	93.38	22.58	0.319	5524.4
12	62.26	15.77	0.339	4041.3

Calorimetric method. For calorimetric measurements, a differential scanning calorimeter DSC 204 F-1 Phoenix (NETZSCH) was used. To measure the heat capacity, a sample of moist mineral soil was placed in an aluminum container (V = 25 mm^3, d = 6 mm). The mass of the sample in the container varied from 42 to 93 mg (Table 1). The mass was controlled by weighing on a balance with an accuracy of 0.5 mg. Weighing was carried out before the measurement procedure, after the measurement, and after drying the mixture. Drying of the mixture was carried out at a temperature of 104°C for 8 h. After weighing, the gravimetric moisture content of the samples (m_g) was calculated, which is defined as the ratio of the mass of water (m_w) in the soil to the mass of dry soil (m_d). Additionally, the control of possible water losses during the measurements was carried out. The measurements were carried out during the heating of the sample at a constant rate of 1 K/min. This heating rate was chosen as optimal to reduce the duration of one experiment while maintaining the appropriate sensitivity and resolution of the equipment. The experimental data were processed using the NETZSCH Proteus Thermal Analysis software package.

The calorimeter has two measuring cells: one is intended for the test sample, the second remains empty. The location and design of the cells is made as symmetrical as possible (the same crucibles, the same sensors, the same distance from the heater to the sensor, etc.). Each cell is equipped with an individual thermal sensor and a microheater. An experimental signal measured by a calorimeter carries information not only about the phenomenon under study but also about the features of the method, the design of the device, and the conditions of the experiment. Regardless of the design of the device, instead of the real heat flow ($q(T)$) the calorimeter measures some experimental heat flow curve ($h(T)$). The presence of ther-

mal resistance between the sample and the thermal sensor leads to the effect of broadening the experimental curve. With an increase in the rate of temperature change, this broadening of the experimental curve becomes more pronounced. In this regard, regardless of the design of the calorimeter, the experimental heat flow curves ($h(T)$) obtained using it are not true [*Hemminger, Hehne, 1989; Kozlowski, 2003a; Emelina, 2009*]. Due to this feature, it is difficult to calculate the unfrozen water content m_u at a specific temperature, which can lead to errors if the calculation method does not allow obtaining a real heat flow signal, such a method was used in work [*Mironov et al., 2018*].

To isolate the real heat flow signal, at the first stage, calibration measurements of the heat flows of substances are carried out, the thermodynamic characteristics of phase transitions of which are known. Then, using deconvolution, the instrumental function is calculated that describes the influence of the device elements on the experimental signal. After that, deconvolution is applied to the recorded signal of the sample, the thermodynamic characteristics of phase transitions in which are to be measured. Taking into account the found hardware function, a signal of the real heat flow is obtained. This procedure is described in detail in [*Kozlowski, 2003a*]. Additionally, this method makes it possible to find the melting liquidus temperature at which all ice passes into the liquid phase. For distilled water outside the soil under normal conditions, this temperature is 0°C; for soil water. this temperature can be in the subzero rage (close to 0°C). However, this method is rather complicated, as numerical analysis is required.

A method for reconstructing a real heat flow signal [*Kozlowski, 2003a; Kozlowski, Nartowska, 2013*] was tested and used to calculate the unfrozen water content. As a result of the measurements, differential scanning calorimetry (DSC) signals were recorded depending on the temperature and the total amount of absorbed heat (Δh) for each measured sample (table). As an example, Fig. 1 shows the experimental DSC peaks for some water contents.

The experimental heat flow curve ($h(T)$) can be transformed into a real heat flow ($q(T)$) using the apparatus function ($a(T)$). The apparatus function describes the influence of the elements of the measuring setup on the recorded heat flow signal and, for the same experimental conditions, does not depend on the measured substance. The hardware function makes it possible to establish a connection between the measured and real heat flow signals and is equal to the response of the experimental setup to a single heat flow pulse caused by a phase transition in the sample.

The apparatus function can be found empirically by measuring a substance undergoing a phase transition in the temperature range under consideration, whose thermodynamic parameters are known (in our case, such a substance was distilled water):

$$a\left(T_0 - T\right) = \frac{h\left(T_0 - T\right)}{\Delta h}, \qquad (1)$$

where $h(T)$ is the experimental function of the heat flow, J/K, Δh is the total amount of absorbed heat at temperature T_0, J, and $a(T)$ is the apparatus function of the calorimeter used.

The observed heat flow function was divided into the number of finite elements of width $\Delta T_i = T_{i+1} - T_i$, for each of which some value of the heat flow ($h(T_i)$) was compared. The hardware function was also divided into intervals of the same width. The expression for the observed heat flow ($h(T_j)$) at a certain temperature (T_j) is written as a discrete convolution of the apparatus function ($a(T)$) and the real heat flow ($q(T)$) as follows:

$$h\left(T_j\right) = \sum_{i=1}^{n} \sum_{j=i}^{i+m-1} a\left(T_j - T_i\right) q\left(T_i\right) \Delta T_i, \qquad (2)$$

where n is the number of elements of the observed function and m is the number of elements of the apparatus function. The experimental function of the real heat flow is determined by solving Eq. (2) for the unknown value $q(T_i)$ by a numerical method by minimizing the functional of the following form:

$$D_k = \sum_{i=1}^{n} \left(h\left(T_1\right) - h_k\left(T_i\right)\right)^2. \qquad (3)$$

Here, D_k is the sum of the squares of the difference between the values of the measured and calculated by formula (2) heat flows ($h(T_i)$ and $h_k(T_i)$), respectively. Thus, knowing the temperature depen-

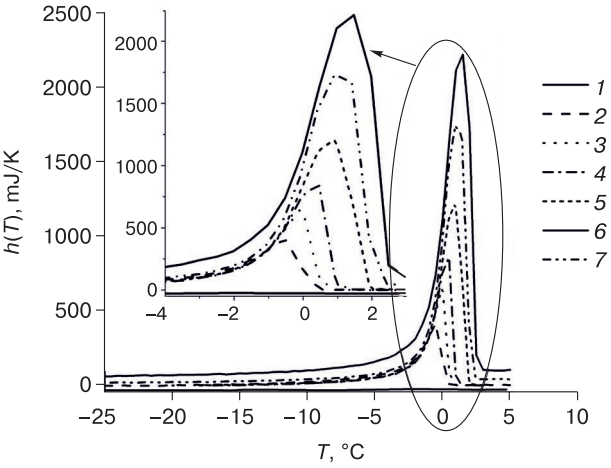

Fig. 1. Endothermic peaks for mineral soil samples with different mass moisture content (m_g), depending on temperature.

1 – 0.054 g/g; *2* – 0.144 g/g; *3* – 0.178 g/g; *4* – 0.205 g/g; *5* – 0.276 g/g; *6* – 0.319 g/g; *7* – 0.339 g/g.

dence of $a(T)$ and $h(T)$, with the help of Eqs. (1)–(3), real thermal peaks associated with the processes of phase transitions in the sample can be reconstructed.

In order to calculate the specific unfrozen water content, the following equation was used:

$$m_u\left(T_i\right) = w - \sum_{j=i}^{n} \frac{100q\left(T_i\right)\Delta T_j}{\lambda m_s}, \qquad (4)$$

where $m_u(T_i)$ is the mass content of unfrozen water at the temperature T_i, %, λ is the specific heat of ice melting, J/g, w is the total water content in the sample by mass, %, and m_s is the mass of dry soil, g.

Dielectric method. To carry out dielectric measurements, a dielectric measuring complex was used, which includes: a Keysight N5232 vector network analyzer, an SU-241 Espec temperature camera, a coaxial measuring container, and a personal computer.

The measured soil sample with a given moisture content was placed in a container made in the form of a coaxial waveguide. The length of the container was 37 mm, its radius was 7 mm, and the radius of the central conductor was 3 mm. The measurements were carried out in the temperature range from –30 to 0°C. An SU-241 Espec temperature chamber was used to maintain a stable set sample temperature. The temperature setting accuracy in the chamber was 0.1°C. The vector network analyzer makes it possible to measure, in the frequency range from 300 kHz to 20 GHz, the frequency spectra of the elements of the scattering matrix S of a connected quadripole, which consists of a series-connected container and adapters that match the connectors of the container and the vector analyzer. Using the vector network analyzer, the amplitude and phase of the scattering matrix components S_{11} and S_{12} were recorded in the frequency range from 0.05 to 15 GHz. Using the methodology described in [*Mironov et al., 2010, 2013*], the frequency spectra of the real and imaginary parts of the complex refractive index (CRI) of moist mineral soil samples were obtained from the S-elements of the scattering matrix:

$$n_s = n_s + i\kappa_s,$$

where n_s and κ_s are the refractive index (RI) and the normalized attenuation coefficient (NAC) of the electromagnetic wave in the measured sample, respectively.

As a result, the values of RI and NAC were obtained for mineral soil samples with different moisture contents. To determine the content of bound water in soil samples, the frequencies of 500 MHz, 1.4 GHz, and 6.9 GHz were chosen. Contact measurements with moisture sensors can be carried out using moisture meters based on the Time Domain Reflectometry (TDR) method with a spectral frequency range from 10 MHz to 3 GHz [*Topp et al., 2000*]. In order to reduce the influence of the clay fraction on the accuracy of moisture measurements, it was proposed in [*Lin, 2003*] to use the frequency range of 0.5–1.0 GHz. In this regard, a frequency of 500 MHz was chosen. Frequencies of 1.4 GHz and 6.9 GHz are used to show that the content of bound water in frozen soil does not depend on frequency; in addition, these frequencies are widely used in remote sensing of the Earth by radiophysical methods.

As an example, for some temperatures, Fig. 2 shows the dependences of the reduced RI ($(n_s - 1)/\rho_d$) and NAC (κ_s/ρ_d) on moisture; here, ρ_d is the density of the dried soil.

In order to find the unfrozen water content, the refractive equation of a mixture with two forms of soil water was used in the following form [*Mironov et al., 2017, 2020*]:

$$\frac{n_s - 1}{\rho_d} = \begin{cases} \dfrac{n_m - 1}{\rho_m} + \dfrac{n_b - 1}{\rho_b} m_g, & m_g \le m_{gt}, \\ \dfrac{n_m - 1}{\rho_m} + \dfrac{n_b - 1}{\rho_b} m_{gt} + \dfrac{n_i - 1}{\rho_i}\left(m_g - m_{gt}\right), & m_g \ge m_{gt}, \end{cases} \qquad (5)$$

$$\frac{\kappa_s}{\rho_d} = \begin{cases} \dfrac{\kappa_m}{\rho_m} + \dfrac{\kappa_b}{\rho_b} m_g, & m_g \le m_{gt}, \\ \dfrac{\kappa_m}{\rho_m} + \dfrac{\kappa_b}{\rho_b} m_{gt} + \dfrac{\kappa_i}{\rho_i}\left(m_g - m_{gt}\right), & m_g \ge m_{gt}. \end{cases} \qquad (6)$$

Here, the subscripts *s, d, m, b,* and *i* refer to moist soil, dry soil, mineral component, bound water, and ice, respectively; m_{gt} is the maximum content of bound water at a fixed temperature; and m_g is the gravimetric moisture content of the sample, g/g.

Equations (5) and (6) describe the dependence on mass moisture of the values of RI and NAC of

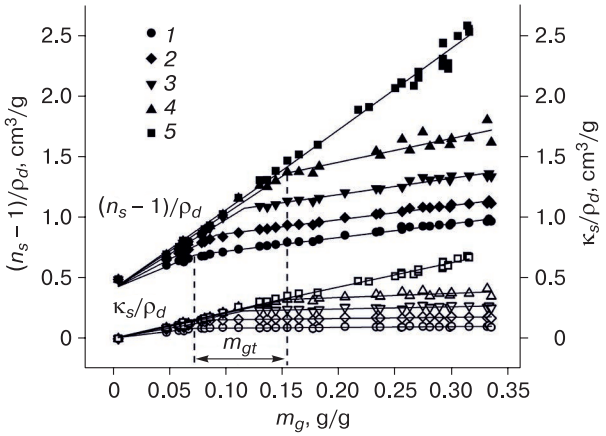

Fig. 2. Reduced refractive index ($(n_s - 1)/\rho_d$) and normalized attenuation coefficient (κ_s/ρ_d) of an electromagnetic wave measured in soil at different temperatures depending on mass moisture (m_g) at a frequency of 500 MHz.

1 – T = –30°C; *2* – T = –15°C; *3* – T = –5°C; *4* – T = –1°C; *5* – T = 0°C.

moist soil reduced in a certain way to a single density by piecewise linear functions with break points corresponding to the maximum content of bound water m_{gt}. As can be seen in Fig. 2, CRI values depending on moisture can indeed be described by a piecewise linear function. Approximation of the experimental values of RI and NAC using equations (5) and (6) makes it possible to determine the value of m_{gt} in frozen soil at each measurement temperature. The m_{gt} value separates the moisture regions related to bound water and ice as shown in Fig. 2. As can be seen in Fig. 2, m_{gt} changes its value from 0.07 at −30°C to 0.15 at −1°C, which is marked by vertical dotted lines. Also, in Fig. 2, together with the experimental values, the lines show the results of the approximation using equations (5) and (6) as theoretical functions.

Testing methods on the example of measuring the unfrozen water content in Na-*bentonite clay.* Earlier in [*Mironov et al., 2018*], joint calorimetric and dielectric studies of the content of unfrozen water and bound water in Na-bentonite clay were carried out. In this work, a calorimetric method was proposed to determine the unfrozen water content from an experimental heat flow curve without reconstructing the real heat flow. However, due to the chosen relatively low rate of temperature change, 5 K/min, this method showed a fairly good agreement with the results of measurements of the content of bound water obtained by the dielectric method. Meanwhile, it is rather difficult to preliminarily choose the rate of temperature change during calorimetric measurements, at which one can neglect the difference between the measured heat flow signal and the real one. Therefore, it makes sense for calorimetric measurements to use the method proposed in [*Kozlowski, 2003a; Kozlowski, Walaszczyk, 2014*], which assumes the restoration of the real heat flow using the apparatus function obtained in the course of preliminary calibration measurements.

In order to assess the applicability of the method of measuring the content of unfrozen water without reconstructing the real thermal signal in relation to natural mineral soils, test calculations of moisture content due to the content of unfrozen water in samples of Na-bentonite clay were carried out from the DSC measurements given in [*Mironov et al., 2018*]. Next, the calculation results from the data of the recorded heat flow signal were compared with the results obtained using the method that assumes the restoration of the real signal. Figure 3 shows the temperature dependences of the maximum content of bound water in frozen Na-bentonite clay, as well as moisture content due to the unfrozen water content calculated from the data of calorimetric measurements using various methods: calculation from the signal recorded by the device and calculation from the reconstructed real heat flow signal. The moisture content due to the content of unfrozen water determined by the method from [*Mironov et al., 2018*] was calculated using the following expression:

$$m_u = \frac{\Delta h}{\lambda_{ti} m_d} + m_{un}, \qquad (7)$$

where λ_{ti} is the specific heat of ice melting equal to 291 J/g, m_{un} is the content of unfreezable water (the amount of water that does not undergo a phase transition in the considered temperature range), and Δh is the total amount of absorbed heat.

Figure 3 shows that the m_u values calculated by the two methods correspond to one another up to a temperature of −10°C. At temperatures above −10°C, discrepancies begin in the values of the unfrozen water content. This is due to the fact that the method proposed in [*Mironov et al., 2018*] does not take into account the difference between the experimental heat flow function and the real heat flow. At the moment when the temperature of the frozen clay sample reaches the temperature of the end of ice melting (for some samples, it was −3°C), the beginning of a discrepancy between the values of m_u and the maximum content of bound water is observed. The moisture value obtained using the calorimetric method corresponds to the total water content in the sample, including bound and unbound water, which cannot be distinguished by the calorimetric method used, while the dielectric method allows determining the proportion of bound water in thawed soil. In frozen soil, calorimetric and dielectric methods determine the relative content of only one form of water, unfrozen water.

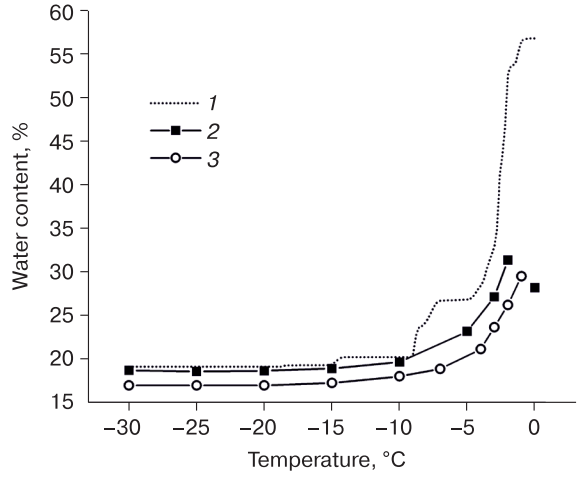

Fig. 3. Dependence of bound water content (m_{gt}) and unfrozen water content (m_u) on temperature for Na-bentonite clay.

(*1*) unfrozen water content obtained using the method from [*Kozlowski, 2003a*] for a sample with moisture content m_g = 0.58 g/g, (*2*) maximum bound water content determined from dielectric measurements, (*3*) bound water content obtained using the method from [*Mironov et al., 2018*].

RESULTS AND DISCUSSION

The unfrozen water content. Measurement of the unfrozen water content with the procedure for reconstructing the real heat flow signal [*Kozlowski, 2003a; Kozlowski, Walaszczyk, 2014*] tested on samples of Na-bentonite clay was applied to samples of natural mineral soil. The apparatus function $a(T)$ was determined from the calorimetric peak $h(T)$ obtained from a 22-mg sample of distilled water. The specific heat of fusion of distilled water was measured to be 327 J/g. This is slightly below the table value $\lambda = 334$ J/g, but still very close to it. The observed peak was divided into regions with a width of $\Delta T = 0.2$ K. Using Eq. (1), the experimental discrete instrumental function of the calorimeter used was obtained, which is shown in Fig. 4.

Further, by solving Eq. (2) using the numerical method of minimizing the functional (3), the real heat flow ($q(T)$) from soil samples of different moisture contents was found. Just as with distilled water, the initial thermal signal was divided into regions with a width of $\Delta T = 0.2$ K. As a result of numerical simulation, the best agreement between the observed calorimetric peaks and the calculated ones was obtained. Using the obtained temperature dependence of the heat flow from soil samples ($q(T)$) and Eq. (4), the content of unfrozen water for the measured frozen soil samples was calculated (Fig. 5). The temperature of the end of ice melting in the soil for the studied samples varied from −2.8 to −0.6°C. Here, the pattern is clearly visible: the lower the moisture content of the test sample, the lower the temperature of the end of melting.

The maximum content of bound water. As a result of the analysis of the dependences of the reduced RI and NAC of the studied samples on the water content obtained as a result of dielectric measurements and shown in Fig. 2, two forms of soil water have been identified in the frozen soil: bound water and ice. According to [*Mironov et al., 2018*], ice and two forms of bound water were identified in frozen Na-bentonite clay, namely: tightly bound and loosely bound water. Such a difference between natural mineral soils and bentonite clay is due to the fact that the specific surface area in the bentonite clay is significantly higher than that in mineral soils, and, consequently, the content of water bound by clay particles should be greater. In mineral soils, where the content of water bound on soil particles is lower, it is impossible to separate tightly bound and loosely bound water, which is confirmed in [*Mironov et al., 2017, 2020*] on the example of several mineral soils. This is clearly seen in Fig. 2, where two segments of piecewise function are clearly distinguishable, the slope of each of which to the moisture axis is determined by the dielectric constant of a certain form of water.

Using Eqs. (5) and (6) and applying the approximation method to the obtained moisture dependences of RI and NAC, the values of the maximum content of bound water at three frequencies depending on temperature were obtained (Fig. 6). Figure 6 shows that the differences in the values of the maximum content of bound water found at different frequencies of the electromagnetic wave are within the measurement error. Similar assessments were made in [*Mironov et al., 2018*] for samples of Na-bentonite clay, where the same results were obtained. Accordingly, it can be concluded that the content of bound water in frozen mineral soils does not depend on the frequency of the electromagnetic wave in the studied frequency range.

Since the dielectric properties of bound water differ from the dielectric properties of ice, when cre-

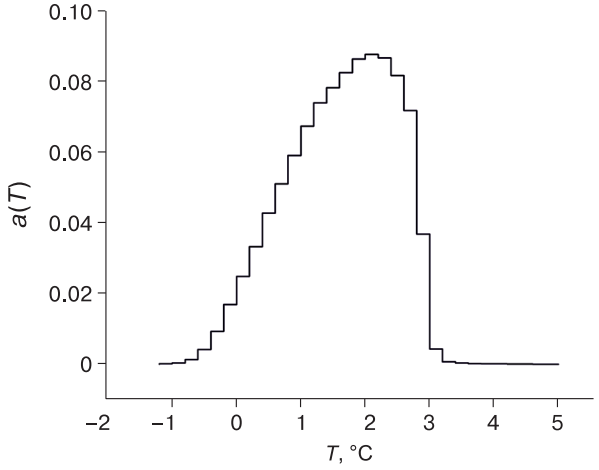

Fig. 4. Apparatus function ($a(T)$), obtained for a sample of distilled water weighing 22 mg.

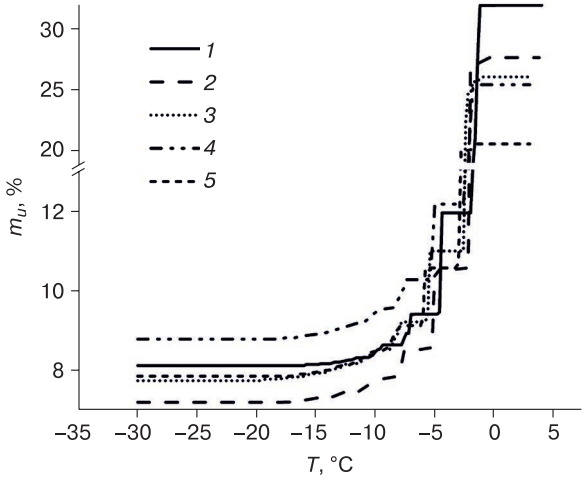

Fig. 5. Dependence of the content of unfrozen water (m_u) on temperature for mineral soil samples with different gravimetric water content (m_g).

1 – 0.310 g/g; *2* – 0.276 g/g; *3* – 0.260 g/g; *4* – 0.254 g/g; *5* – 0.205 g/g.

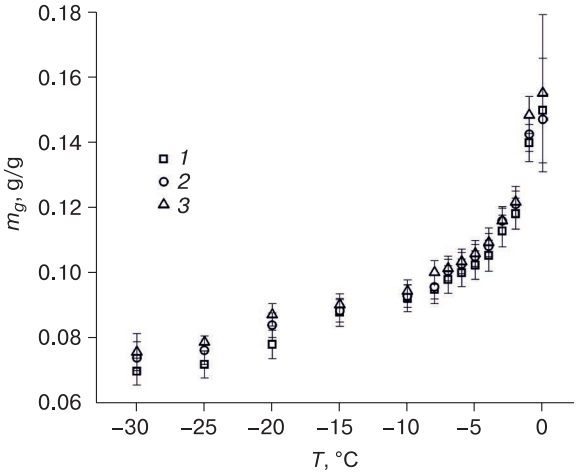

Fig. 6. Dependence of the maximum content of bound water in mineral soil samples (m_g) on temperature at frequencies:

1 – 500 MHz, *2* – 1.4 GHz, *3* – 6.9 GHz.

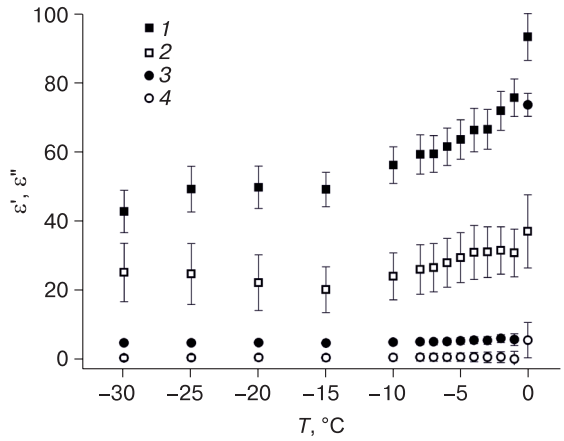

Fig. 7. Temperature dependence of the real and imaginary parts of the complex permittivity (ε′, ε″) of bound water and ice in frozen mineral soil at a frequency of 500 MHz.

1 and *2* are the real and imaginary parts of the complex permittivity of bound water, *3* and *4* are the real and imaginary parts of the complex permittivity of ice.

ating dielectric models of frozen soils for use in moisture meters, it is necessary to correctly take into account the RP of each form of soil water. Using the refractive model (5) and (6), the CP values of bound water and ice were found in frozen soil samples at a frequency of 500 MHz (Fig. 7). Figure 7 shows a decrease in the values of the real and imaginary parts of the CP of bound water with decreasing temperature. Thus, the real part of the CP of bound water decreases from 93 at a temperature of 0°C, to 43 at a temperature of −30°C. Noticeable changes in the CP of ice were not found in the entire temperature range under consideration.

Having obtained the temperature dependencies of moisture for the unfrozen water and bound water found by dielectric and calorimetric methods, one can compare them. For convenience, these dependencies are shown on one graph (Fig. 8). It can be seen from Fig. 8 that the unfrozen water content in the temperature range from −30 to −15°C for samples with different initial moisture slightly varies within 1.6%. This form of water can be classified as unfreezable water in the considered temperature range. Similar variations were also found in [*Kozlowski, 2003b*] for bentonite clay. In the temperature range from −30 to −15°C, the maximum content of bound water m_{gt} measured for this soil by the dielectric method and equal to 7.4% is also within the variation of the content of unfreezable water. From this we can conclude that the content of nonfreezing water at temperatures below −15°C can be determined by dielectric and calorimetric methods. In the temperature range from −15 to −2°C, the maximum content of bound water is within the range of variation in the unfrozen water content. This also proves that two different methods can measure the content of the same form of water.

Differences between the unfrozen water content and the maximum content of bound water begin at temperatures above −2°C, when soil samples reach their melting point. The calorimetric method measures the mass of ice that has undergone a phase transition to unfrozen water. After the entire volume of ice melts, the content of unfrozen water becomes

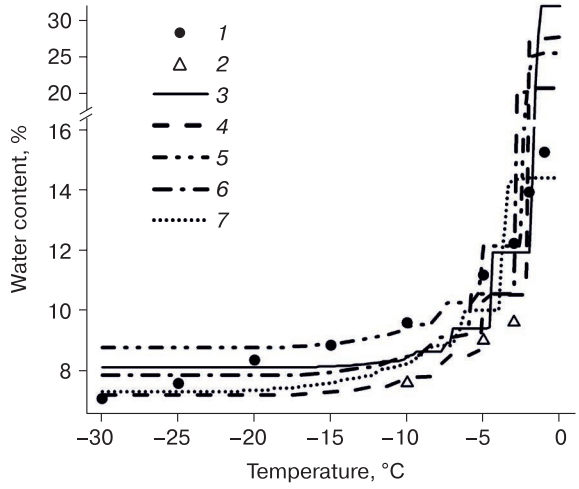

Fig. 8. Temperature dependences of the (*1*) maximum content of bound water obtained by the dielectric method (m_{gt}), (*2*) unfrozen water content obtained by the contact method (m_{cm}); (*3*–*7*) unfrozen water content obtained by the calorimetric method (m_u) for samples with different mass moisture (m_g):

3 – 0.310 g/g, *4* – 0.276 g/g, 5 – 0.254 g/g, *6* – 0.205 g/g, and *7* – 0.144 g/g.

equal to the total water content in the soil, while the calorimetric method does not allow separating liquid bound and unbound water. In dielectric measurements, the content of bound water is determined from the value of its CP. Bound water is observed both in frozen and thawed soil [*Bogdan et al., 1996; Turov, Leboda, 1999*], and the value of the CP of liquid bound water differs from the values of the CP of both ice and liquid unbound water, which makes it possible to determine the content of bound water by the dielectric method at both negative and positive temperatures. In a frozen soil, m_u and m_{gt} are the same, and m_{gt} can be defined as the unfrozen water content.

Although both calorimetric and dielectric methods allow us to determine the moisture content of frozen soil (the unfrozen water content), these methods are still indirect. In this regard, at several temperatures, additional measurements of the content of unfrozen water (m_{cm}) were performed by the direct contact method. The contact method is a standard method for measuring the unfrozen water content; it is described in detail in [*GOST R 59537-2021, 2021*]. The results of measurements using the contact method are shown in Fig. 8 by triangles. Figure 8 shows that the values of m_{cm} are within the range of variation in the m_u values measured by the calorimetric method, near its lower boundary. The values of m_u for different moisture contents vary within 17%. The difference between the m_{gt} values and the m_{cm} values at the same temperatures ranged from 10 to 17%, which is comparable with the m_u variations. Thus, it can be concluded that the values of moisture due to the unfrozen water content obtained by the calorimetric and dielectric methods coincide with the values of moisture due to the content of unfrozen water obtained by the contact method.

CONCLUSIONS

Our study showed that the values of moisture due to the unfrozen water content measured by calorimetric and dielectric methods are close and agree well with one another. In general, when the soil temperature changes from −30 to 0°C, the maximum content of bound water determined by the dielectric method is within the limits of moisture variations due to the content of unfrozen water measured by the calorimetric method, which are 17% for soil samples of different moisture contents. Also, the values of the maximum content of bound water are quite close to the values of moisture due to the unfrozen water content obtained by the contact method. The difference for the studied temperatures ranged from 10 to 17%, which is comparable to the limiting variations in moisture due to the unfrozen water content measured using the calorimetric method for samples with different initial moisture. As a result of joint measurements of the content of unfrozen water in frozen mineral soil using the dielectric, calorimetric, and contact methods, the possibility of practical use of the dielectric method for measuring the unfrozen water content was confirmed, and the measurement errors of this method were estimated. These studies can serve as the basis for the creation of moisture meters for frozen mineral soils due to the unfrozen water content, which are based on electromagnetic methods.

The coincidence of the temperature dependences of the maximum content of bound water with the temperature dependences of moisture due to the unfrozen water content confirms the fact that phase transitions of ice into unfrozen water can be studied using dielectric measurements.

The method for measuring the content of unfrozen water in mineral soils proposed in [*Mironov et al., 2018*] can be applied in the temperature range from −30 to −5°C. The results of measuring the content of unfrozen water by different methods in this temperature range are the same. This method is simpler and does not require the use of complex numerical calculation methods. The method proposed in [*Kozlowski, 2003a*] is applicable for the entire temperature range under study and makes it possible to calculate the moisture due to the unfrozen water content up to the end temperature of the wet sample thaw, and also to find this temperature. The disadvantages of the method include only the complexity in the calculations, since it is necessary to use numerical calculation methods.

References

Ananyan A.A., 1961. On the relationship between the unfrozen water content in finely dispersed frozen soils and their water-physical properties. *Merzlotn. Issledov.*, iss. **1**, 184–189 (in Russian).

Andrianov P.I., 1936. *Soil Freezing Temperatures.* Moscow, Izd. AN SSSR, 16 p. (in Russian).

Bobrov P.P., Belyaeva T.A., Kroshka E.S., Rodionova O.V., 2019. Soil moisture measurement by the dielectric method. *Eurasian Soil Sci.* **52** (7), 822–833. https://doi.org/10.1134/S106422931905003

Bogdan A., Kulmala M., Gorbunov B., Kruppa A., 1996. NMR study of phase transitions in pure water and binary H_2O/HNO_3 films adsorbed on surface of pyrogenic silica. *J. Colloid Interface Sci.* **177** (1), 79–87. https://doi.org/https://doi.org/10.1006/jcis.1996.0008

Cheverev V.G., Vidyapin I.Yu., Motenko R.G., Kondakov M.V., 2005. Determination of the content of unfrozen water in ground from sorption-desorption isotherms. *Kriosfera Zemli* IX (4), 29–33 (in Russian).

Chuvilin E.M., Sokolova N.S., Bukhanov B.A. et al., 2020. Application of water-potentiometric method for unfrozen water content determination in different frozen soils. *Earth's Cryosphere* XXIV (5), 14–22.

Emelina A.L., 2009. *Differential Scanning Calorimetry*. Moscow, Izd. Mosk. Gos. Univ., 42 p. (in Russian).

Ershov E.D. (Ed.), 2004. *Methods of Geocryological Research.* Moscow, Moscow Univ. Press, 512 p. (in Russian).

Fabbri A., Fen-Chong T., Coussy O., 2006. Dielectric capacity, liquid water content, and pore structure of thawing-freezing materials. *Cold Reg. Sci. Technol.* **44** (1), 52–66. https://doi.org/https://doi.org/10.1016/j.coldregions.2005.07.001

Frolov A.D., 1998. *Electrical and Elastic Properties of Frozen Rocks and Ice*. Pushchino, ONTI PNC RAN, 515 p. (in Russian).

GOST R 59537-2021 (State Standard), 2021. Soils. Method for Laboratory Determination of Moisture Due to Unfrozen Water. Moscow, Standartinform, 11 p. (in Russian).

Grigoriev B.V., 2020. Development of a calorimetric method for measuring the content of unfrozen water in soil at a negative temperature. *Vestn. Tuymensk. Gos. Univ.* **6** (1), 87–99 (in Russian). https://doi.org/10.21684/2411-7978-2020-6-1-87-99

Hemminger W., Hehne G., 1989. *Calorimetry: Fundamentals and Practice*. Verlag Chemie, 176 p.

Horiguchi K., 1985. Determination of unfrozen water content by DSC. In: *Proc. 4th Int. Symp. Ground Freezing*, Sapporo, p. 33–38.

Hu G., Zhao L., Zhu X. et al., 2020. Review of algorithms and parameterizations to determine unfrozen water content in frozen soil. *Geoderma* **368**, p. 114277. https://doi.org/https://doi.org/10.1016/j.geoderma.2020.114277

Kozlowski T., 2003a. A comprehensive method of determining the soil unfrozen water curves: 1. Application of the term of convolution. *Cold Reg. Sci. Technol.* **36** (1–3), 71–79.

Kozlowski T., 2003b. A comprehensive method of determining the soil unfrozen water curves. 2. Stages of the phase change process in frozen soil-water system. *Cold Reg. Sci. Technol.* **36** (1–3), 81–92.

Kozlowski T., 2007. A semi-empirical model for phase composition of water in clay-water systems. *Cold Reg. Sci. Technol.* **49** (3), 226–236. https://doi.org/10.1016/j.coldregions.2007.03.013

Kozlowski T., 2016. A simple method of obtaining the soil freezing point depression, the unfrozen water content and the pore size distribution curves from the DSC peak maximum temperature. *Cold Reg. Sci. Technol.* **122**, 18–25. https://doi.org/10.1016/j.coldregions.2015.10.009

Kozlowski T., Nartowska E., 2013. Unfrozen water content in representative bentonites of different origin subjected to cyclic freezing and thawing. *Vadose Zone. J.* **12** (1), 1–11. https://doi.org/10.2136/vzj2012.0057

Kozlowski T., Walaszczyk Ł., 2014. Analyzing Expanding Clays by Thermoporometry Using a Stochastic Deconvolution of the DSC Signal. *Clays Clay Miner.* **62** (5), 386–402. https://doi.org/10.1346/CCMN.2014.0620503

Kuzmin G., Sleptsova Y., 2018. Determining unfrozen water content in frozen soils by means of sample deformation. *Vestn. Zabaikal'sk. Gos. Univ.* **25** (1), 4–9 (in Russian).

Lekshmi S.S.U., Singh D.N., Shojaei Baghini M., 2014. A critical review of soil moisture measurement. *Measurement* **54**, 92–105. https://doi.org/10.1016/j.measurement.2014.04.007

Lesaignoux A., Fabre S., Briottet X., 2013. Influence of soil moisture content on spectral reflectance of bare soils in the 0.4–14 μm domain. *Int. J. Remote Sens.* **34** (7), 2268–2285. https://doi.org/10.1080/01431161.2012.743693

Lin C.-P., 2003. Frequency domain versus travel time analyses of TDR waveforms for soil moisture measurements. *Soil Sci. Soc. Am. J.* **67** (3), 720–729. https://doi.org/10.2136/sssaj2003.7200

Mavrovic A., Pardo Lara R., Berg A. et al., 2021. Soil dielectric characterization during freeze–thaw transitions using L-band coaxial and soil moisture probes. *Hydrol. Earth Syst. Sci.* **25** (3), 1117–1131. https://doi.org/10.5194/hess-25-1117-2021

Mironov V.L., Karavayskiy A.Y., Lukin Y.I., Molostov I.P., 2020. A dielectric model of thawed and frozen Arctic soils considering frequency, temperature, texture and dry density. *Int. J. Remote Sens.* **41** (10), 3845–3865. https://doi.org/10.1080/01431161.2019.1708506

Mironov V.L., Karavayskiy A.Y., Lukin Y.I., Pogoreltsev E.I., 2018. Joint studies of water phase transitions in Na-bentonite clay by calorimetric and dielectric methods. *Cold Reg. Sci. Technol.* **153**, 172–180. https://doi.org/10.1016/j.coldregions.2018.04.010

Mironov V.L., Komarov S.A., Lukin Y.I., Shatov D.S., 2010. A technique for measuring the frequency spectrum of the complex permittivity of soil. *J. Commun. Technol. Electron.* **55** (12), 1368–1373. https://doi.org/10.1134/S1064226910120065

Mironov V.L., Kosolapova L.G., Lukin Y.I. et al., 2017. Temperature- and texture-dependent dielectric model for frozen and thawed mineral soils at a frequency of 1.4 GHz. *Remote Sens. Environ.* **200**, 240–249. https://doi.org/10.1016/j.rse.2017.08.007

Mironov V.L., Lukin Y.I., 2011. A physical model of dielectric spectra of thawed and frozen bentonitic clay within the frequency range from 1 to 15 GHz. *Russ. Phys. J.* **53** (9), 956–963. https://doi.org/10.1007/s11182-011-9516-4

Mironov V.L., Molostov I.P., Lukin Y.I., Karavaisky A.Y., 2013. Method of retrieving permittivity from S12 element of the waveguide scattering matrix. In: *Int. Siberian Conf. on Control and Communications (SIBCON)*. Krasnoyarsk (12–13 Sept. 2013), p. 1–3. https://doi.org/10.1109/SIBCON.2013.6693609

Mironov V., Savin I., 2015. A temperature-dependent multi-relaxation spectroscopic dielectric model for thawed and frozen organic soil at 0.05–15 GHz. *Phys. Chem. Earth, Parts A/B/C* **83–84**, 57–64.

Muhammad M., Almushfi S., 2020. Dielectric analysis model for measurement of soil moisture water content using electrical capacitance volume tomography. In: *Modern Applications of Electrostatics and Dielectrics*. London, IntechOpen, 138 p. https://doi.org/10.1016/j.pce.2015.02.011

Nersesova Z.A., Tsytovich H.A., 1963. Unfrozen water in frozen soils. In: *Intern. Conf. on Permafrost. Section 4. Phase Equilibrium and Transitions*. Moscow, Izd. AN SSSR, p. 62–70 (in Russian).

Pardo Lara R., Berg A.A., Warland J., Tetlock E., 2020. In situ estimates of freezing/melting point depression in agricultural soils using permittivity and temperature measurements. *Water Resour. Res.* **56** (5), 1–16. https://doi.org/10.1029/2019WR026020

Topp G.C., Zegelin S., White I., 2000. Impacts of the real and imaginary components of relative permittivity on time domain reflectometry measurements in soils. *Soil Sci. Soc. Am. J.* **64** (4), 1244–1252. https://doi.org/10.2136/sssaj2000.6441244

Tsytovich N.A., 1973. *Mechanics of Frozen Soils*. Moscow, Vyssh. Shkola, 448 p. (in Russian).

Turov V.V., Leboda R., 1999. Application of 1H NMR spectroscopy method for determination of characteristics of thin layers of water adsorbed on the surface of dispersed and porous adsorbents. *Adv. Colloid Interface Sci.* **79** (2), 173–211. https://doi.org/https://doi.org/10.1016/S0001-8686(97)00036-5

Watanabe K., Mizoguchi M., 2002. Amount of unfrozen water in frozen porous media saturated with solution. *Cold Reg. Sci. Technol.* **34** (2), 103–110. https://doi.org/10.1016/S0165-232X(01)00063-5

Zhang L., Zhao T., Jiang L., Zhao S., 2010. Estimate of phase transition water content in freeze–thaw process using microwave radiometer. *IEEE Trans. Geosci. Remote Sens.*, **48** (12), 4248–4255. https://doi.org/10.1109/TGRS.2010.2051158

Received September 20, 2021
Revised July 21, 2022
Accepted December 6, 2022

Translated by A.V. Muravyov

EARTH'S CRYOSPHERE
SCIENTIFIC JOURNAL

Earth's Cryosphere, 2023, vol. XXVII, No. 1, pp. 30–38

SURFACE AND GROUND WATERS IN TERRESTRIAL PERMAFROST REGION

HYDROGEOLOGICAL CONDITIONS IN THE LENA RIVER FLOODPLAIN NEAR YAKUTSK

N.A. Pavlova*, V.V. Ogonerov, M.V. Danzanova, L.S. Lebedeva

Melnikov Permafrost Institute, Siberian Branch of the Russian Academy of Sciences, Merzlotnaya St. 36, Yakutsk, 677010 Russia

**Corresponding author; e-mail: napavlova@mpi.ysn.ru*

This paper reports on the hydrogeological conditions and groundwater regime in the Lena River floodplain near Yakutsk. The published and archive materials, including field data collected by the authors in 2013–2021, were analyzed. Data from more than 70 boreholes were examined to characterize permafrost and hydrogeological conditions in the area. Data on groundwater level monitoring in the reclaimed area of the floodplain were also used. Over 250 sample analyses were interpreted to characterize the chemical composition of surface and ground waters. The results suggest that suprapermafrost waters in the high floodplain are recharged both by infiltration of river water and by a transit water flow under the river channel hydraulically connected to floodplain taliks. The seasonal and spatial variability of the chemical composition of waters was revealed in the Lena River and in the studied taliks. The surface and ground waters of the Quaternary aquifer on the east bank of the Lena River are characterized by the lowest total dissolved solids (TDS) concentration (0.1–0.3 mg/L) and by the magnesium–calcium chloride–bicarbonate composition. These waters are recharged by fresh water of the supra- and interpermafrost taliks of the Bestyakh terrace and by the riverbed taliks under small rivers. In the vicinity of Yakutsk, TDS concentrations in the Lena River and in the Quaternary aquifer increase to 0.5–1.3 g/L due to high mobility of chloride and sulfate ions migrating with the surface and suprapermafrost runoff from the low terrace, where the city is located.

Keywords: *Lena River, floodplain taliks, suprapermafrost water, hydrodynamic regime, chemical composition.*

Recommended citation: Pavlova N.A., Ogonerov V.V., Danzanova M.V., Lebedeva L.S., 2023. Hydrogeological conditions in the Lena River floodplain near Yakutsk. *Earth's Cryosphere* XXVII (1), 30–38.

INTRODUCTION

Floodplain and under-channel taliks in river valleys are important, in terms of hydrogeology, in the area of continuous permafrost. Groundwater generally passes through suprapermafrost taliks in the zone of free water exchange [*Romanovsky, 1983; Mikhailov, 2013*]. Open under-channel taliks are a kind of a buffer providing water exchange between the surface and subpermafrost waters [*Fotiev, 2009; Chang, Qianlai, 2017; Shepelev, 2021*].

In recent years, the study of the floodplain taliks in the middle reaches of the Lena River has become more relevant. First of all, this is caused by the increasing demand of the population of Central Yakutia for water. It is difficult to cover this demand by exploiting subpermafrost aquifer complexes due to their limited natural resources and the significant thickness (165–470 m) of permafrost. Secondly, the technogenic load on the river ecosystem increases due to the engineering development of the territory. For example, in 1980–2013, in the vicinity of Yakutsk, the part of the Lena River floodplain was reclaimed and two residential city quarters were built up. In the early 2000s, an underwater gas pipeline was laid along the river bed. In addition, a bridge over the river is planned to be built. To provide the safe operation of these facilities, as well as the further development of floodplain areas, it is important to assess the distribution of groundwater in the Lena River valley. The purpose of this work was to study the permafrost-hydrogeological conditions of the floodplain-channel complex in the section Tabaga–Yakutsk, where the above-mentioned engineering structures are concentrated.

MATERIALS AND METHODS

Data from the permafrost-hydrogeological and hydrogeochemical studies of the aquifers developed under the channel, watercourses, and floodplain of the Lena River were used in this work. The data have been collected over many years. To characterize the geological-hydrogeological and geocryological conditions of the territory, more than 70 boreholes were studied. Hydrodynamics of groundwater of the taliks was considered on the basis of the archive materials and the data of monitoring made by the author's team in the floodplain in 2013–2021. The chemical composition of the surface and groundwaters was analyzed for more than 250 water samples. Of these, 78 samples were collected from the Lena River and its tribu-

taries, 60 samples from the boreholes that uncovered suprapermafrost groundwater of the under-channel and floodplain taliks, 94 samples from 9 boreholes equipped for monitoring in the reclaimed floodplain area of Yakutsk, 20 samples from the boreholes drilled through the open under-channel talik in the area of Tabaga village and Pokrovsk settlement, 6 samples from under-channel taliks of the Tamma and Shestakovka rivers. In addition, the results of chemical analyses of inter- and subpermafrost waters developed in the adjacent area were involved.

HYDROLOGICAL CONDITIONS

The studied territory is located in the middle reaches of the Lena River, where the river passes from the Prilensky Plateau to the Central-Yakutia Lowland. The narrow (4–5 km) valley of the river with a bluff right bank at Tabaga Cape is replaced downstream by the wide (8–15 km) terraced accumulative plain downstream. The mean annual runoff of the Lena River near Yakutsk is 7070 m^3/s; the maximum runoff is 36 200 m^3/s [*Chalov et al., 2016*]. The river belongs to the East Siberian type. The water level is 81.7–83.5 m a.s.l. during the winter low-water season (March–April). During the spring flood, the water level rises up to 7–11 m and causes flooding of the wide floodplain; the 5% probability maximum water level in the river reaches 94.7 m a.s.l. (in Yakutsk). Ice on the Lena River forms in October. Temperature of river water varies according to the changes in hydrological conditions: it is 0–1°C in winter and during the spring flood, about 10–12°C in June, and 15–17°C in July [*Gautier et al., 2018*].

Downstream Tabaga Cape, the branching of the Lena River channel is observed; there are numerous islands of 0.5 to 10 km in length (Fig. 1). The erosion of river banks and islands in some areas and the accumulation of sediment in others lead to shifts in the mainstream and to the redistribution of river runoff along several branches contributing to their migration, dissection, and periodic shallowing and deepening [*Tananaev, 2016*]. For example, at the beginning of the 20th century, a ship track was laid along the Gorodskaya watercourse [*Chistyakov, 1952; Chalov et al., 2016*]. In the 1940s and early 1950s, the dynamic axis of the river flow shifted to the right bank. Later on, under the influence of natural channel processes and the construction of an enclosing dam, the Gorodskaya watercourse shallowed and gradually turned into a secondary stream crossing the floodplain.

The floodplain of the Lena River is two-sided. The exception is the section near the settlement of Nizhnii Bestyakh, where the water flow adjoins the Bestyakh terrace. The floodplain topography is slightly hilly, with numerous narrow elongated oxbow lakes and watercourses and low ridges.

The uneven thickness of the Quaternary alluvial sediments under the river bottom is due to deformations of the channel. The thickness of the alluvium varies from 1 to 18 m directly under the channel and watercourses of the Lena River [*Stognii, 2003; Khristoforov, Omelyanenko, 2013*]. It is represented by fine- and medium-grained quartz-feldspar sands, with fine and coarse gravels of quartz, flint, and limestone at the base of the section. The floodplain ridges are composed of sands of channel facies in the lower part of the section and loamy sandy and loamy sediments of 0.5–5.0 m in thickness in the upper part [*Roman et al., 2008*]. The total thickness of the alluvial formations in the floodplain near Yakutsk is about 7–15 m. The Quaternary sediments are underlain by the Middle Jurassic siltstone and quartz-feldspar micaceous sandstone with frequent interlayers of clay.

Small tributaries of the Lena River (the left-bank rivers – Shestakovka, Markhinka, and Khorogor and the right-bank rivers – Tamma and Myla) periodically dry up in summer and freeze completely in winter, except for the deepest parts of river channels [*Anisimova, Pavlova, 2014*].

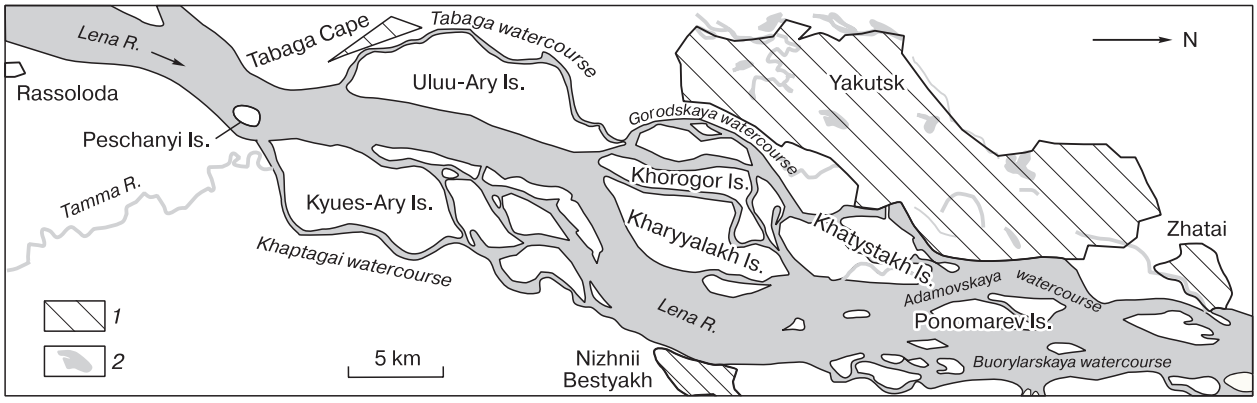

Fig. 1. Schematic map of study area.

1 – settlements; *2* – watercourses and water bodies.

Floodplain taliks

Studies of taliks in the Lena River valley near Yakutsk began in the 1930s–1960s in connection with the search for groundwater to provide technical and drinking water supply for the city population [*Melnikov, 1963; Efimov, 1964*]. As a result of these works, a suprapermafrost talik of 24–30 m in thickness was found under the Gorodskaya and Adamovskaya watercourses of the Lena River; its contours are limited by the low-water level of the river [*Hydrogeology of the USSR, 1970*]. Groundwater with a temperature of 0.5–2°C occur in the Quaternary alluvial sediments and the upper part of the weathered Middle Jurassic deposits.

The thickness of the suprapermafrost water-bearing taliks does not exceed 10–12 m under the drying and freezing watercourses of the Lena River, as well as under the oxbow lakes flooded during floods (Fig. 2) [*Balobaev et al., 2003; Roman et al., 2008; Pavlova et al., 2020*]. The cryogenic aquiclude occurs deeper. According to the classification by N.N. Romanovskii [*Romanovskii, 1983*], most floodplain taliks belong to the soil-filtration class, but there are also taliks with stagnant water [*Anisimova et al., 2005*].

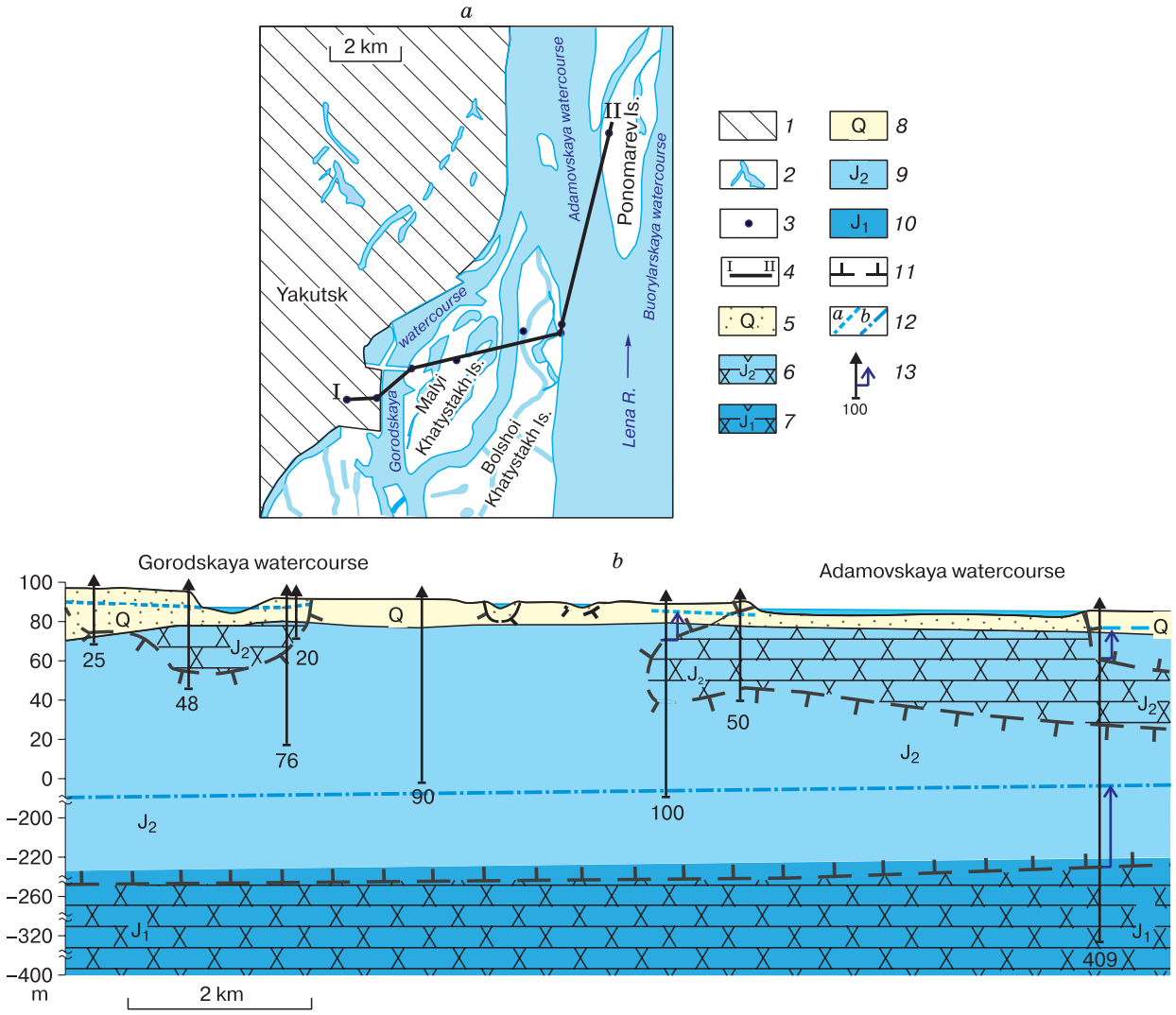

Fig. 2. Schemes of the (*a*) borehole and (*b*) the hydrogeological section of the Lena River floodplain near Yakutsk.

a: (*1*) Yakutsk territory, (*2*) watercourses and water bodies, (*3*) exploration hydrogeological borehole; (*4*) line of the hydrogeological section; *b*: (*5*) local aquifers in Quaternary sediments (sands, gravels), (*6*) local aquifers in the Middle Jurassic deposits (sandstone, siltstone, clay), (*7*) subcryogenic (subpermafrost) aquifer in the Lower Jurassic deposits (sandstone, siltstone, aleurite); (*8–10*) permafrost aquicludes in the Quaternary, Middle Jurassic, and Lower Jurassic deposits, respectively; (*11*) permafrost boundary; (*12*) groundwater level position (*a* – suprapermafrost groundwater, *b* – subpermafrost groundwater); (*13*) exploration hydrogeological boreholes (lower figure, depth (m); side arrow, groundwater head).

Often, the spatial position of the suprapermafrost taliks does not correspond to the modern channels of watercourses. This discrepancy is caused by displacement of surface water flows during repeated deformations of the channel, by thermoabrasion of the banks, and by the formation of frozen rocks on the drying near-channel banks [*Romanovskii, 1983; Tananaev, 2005; Shepelev, 2011*]. River waters are known to be the main source of heat on floodplains; the heat and mass transfer between watercourses and rocks is carried out mainly by convection [*Fotiev, 1968, 2009; Romanovskii, 1983; Mikhailov, 2013*]. In the periodically flooded floodplain of the Lena River valley, the convective heat transfer is limited by the alluvium sequence, which has good filtration properties. The underlying Jurassic deposits have poor water abundance because of the predomination of impermeable layers in the section. Therefore, when the heat source (surface flow) is displaced, the conditions for freezing both above and below are created in the closed floodplain taliks, and only well-permeable sediments remain thawed and provide the supra- and interpermafrost runoff. The direction of this runoff (toward a bank or to a low-water river channel) may vary throughout the year in dependence on the ratio of the water level in the aquifer and in the watercourse, but generally corresponds to a slope of the river.

In addition to natural taliks, there are natural-technogenic taliks in the Lena River floodplain. They are widespread under the reclaimed soils of Yakutsk. During creation of the reclamation base for civil construction in 1970–1990, the oxbow lakes and taliks under them were buried under 10–15-m-thick layer of alluvial sands. On the floodplain ridges composed of frozen sands and loamy sands, the top of the cryogenic aquiclude deepened due to a high temperature of the pulp; and artificial water-saturated taliks of up to 3–5 m in thickness were formed under the technogenic soil of 6–8 m in thickness. Suprapermafrost water-bearing taliks under the reclamation massif are preserved to the present day. For example, during the engineering and geological surveys in the residential block 203 in 2013–2019, suprapermafrost groundwater was uncovered by boreholes everywhere at the depths from 6.4 to 13 m [*Roman et al., 2008; Shesternev et al., 2014; Pavlova et al., 2020*]. The thickness of the water-bearing strata varies from 0.5–6.0 m of the floodplain ridges to 12 m or more in the areas of the former oxbow lakes [*Pavlova et al., 2020*]. The aquifer is underlain by permafrost soils of the natural basement. The temperature of the water-bearing sediments, as in natural taliks, varies from 0.1 to 1.5°C.

The absence of the cryogenic aquiclude within the floodplain and under the Lena River channel opposite Yakutsk has not been proved or disproved by drilling and geophysical works so far. The open talik connecting subpermafrost and surface waters, was established under the Lena River by the geophysical works and drilling to the south of the studied area near Pokrovsk and in the area of Tabaga Cape on Peschanyi Island [*Balobaev et al., 2003; Shepelev, Makogonova, 2010*]. Near Pokrovsk, sandy gravelly deposits of up to 27 m in thickness underlain by the Cambrian fractured limestone were uncovered by deep (70–200 m) boreholes on the islands and in the river channel. In this area, the water-discharge talik partially drains the Cambrian subpermafrost water-bearing complexes [*Beletsky, 1975*]. Downstream the Lena River, fractured calcareous rocks dip beneath the Jurassic terrigenous sandstones and siltstones. At Peschanyi Island, according to the data from the 360-m borehole, the Lower Jurassic 238-m-thick aquifer was uncovered under the 21-m sequence of alluvium; the Middle and Lower Cambrian aquifer complexes lie deeper [*Balobaev et al., 2003*]. Within the Pokrovsk–Tabaga section, some loss of the river runoff indirectly indicates the presence of a water-recharge talik [*Shepelev et al., 2002*].

The open talik in Tabaga Cape area is limited in plan by the Lena River channel. Drilling on the left-bank floodplain of the river near Tabaga settlement revealed permafrost from the surface to a depth of 165 m [*Shepelev et al., 2002*]. On the right bank, it is possible that the open talik may have spread to the floodplain, as well. Before the 19th century, the axis of the main branch of the Lena River was located here; it shallowed over time and formed the Khaptagai watercourse [*Chalov et al., 2016*]. Taking into account the conditions of the formation of the under-channel taliks and their evolution during the displacement of surface water flows, we can expect the decrease in thickness of permafrost to first tens of meters on the right bank near the modern shoreline of the river. It should be noted that the aforementioned open taliks are located in the areas, where the river channel is crossed by tectonic faults or by rock crushing zones.

Within the studied area, the interpermafrost taliks have been uncovered by exploration boreholes on the islands to the north of Tabaga Cape. For example, between Adamovskaya and Buorylarskaya watercourses on Ponomarev Island, thawed water-bearing sediments lie under permafrost rocks from a depth of 25 m. The thickness of the talik is 35 m, and the base of the underlying cryogenic aquiclude was recorded at a depth of 320 m [*Stogny, 2003*]. The water uncovered in the Middle Jurassic sandstone is sodium bicarbonate with the high content of chlorides; the water mineralization is about 1 g/L. This composition may be due to the impeded water exchange in the talik. Permafrost was found on Khatystakh Island, between the Gorodskaya watercourse and the main channel of the Lena River. In the central part of the island, the 90-m deep borehole uncovered permafrost in the entire section (Fig. 2).

Under the small tributaries of the Lena River, the thickness of the under channel taliks varies from

1.5 to 60 m. For example, in the near-mouth part of the Tamma River, water-saturated rocks occur from the depths of 0.3–3.0 m at the end of winter [*Anisimova, Pavlova, 2014*]. The thickness of the talik does not exceed 20 m. It is preserved under the freezing river with a relatively small channel width (10–20 m) due to good filtration properties of sandstone and gravels and because of the relatively high subzero temperature (from –0.2 to –0.7°C) of the surrounding permafrost. The thickness of the under-channel taliks increases in the areas, where sandy gravelly deposits are underlain by the Cambrian fractured calcareous rocks. For example, to the south of the studied area, in the lower reaches of the Mendy River, the thickness of the water-bearing talik is up to 60 m. The under-channel waters of small right-bank tributaries are discharged into the talik of the Lena River.

Under the left-bank small tributaries of the Lena River, taliks are preserved in winter only in some deeper sections of channels; their thickness rarely exceeds 1.5 m [*Anisimova, 1996*].

Hydrodynamic regime of taliks

The hydrodynamic regime of groundwater under the Lena River channel remains poorly studied, because it is difficult to equip the monitoring boreholes in the water area of the river and to keep them safe during ice drift. However, prospecting and exploration works in the Gorodskaya and Adamovskaya watercourses demonstrated that groundwater level in suprapermafrost taliks in winter lowers in parallel to a decrease in the surface water level [*Hydrogeology of the USSR, 1970*]. After experimental pumping from the boreholes, the time of groundwater level recovery is only 15–60 minutes.

The influence of the Lena River on hydrodynamics of groundwater is not limited to the under-channel flow. This is confirmed by the data of long-term observations in the reclaimed area of Yakutsk [*Roman et al., 2008; Pavlova et al., 2020*]. The free surface of suprapermafrost groundwater in the taliks under the reclamation massif is affected by seasonal fluctuations (Fig. 3). Its lowest levels are observed in March–early May corresponding to the winter low-water period in the Lena River. The level of river water at this time is 3–4 m lower than that of the suprapermafrost water in the reclaimed area. In May, with the beginning of flood on the Lena River, water saturation of soils takes place s due to filtration of river waters along the contour of the reclamation massif. The calculated zone with a backwater effect extends to 150–170 m from the watercourse [*Roman et al., 2008*]. In fact, the groundwater surface rises during the period of the maximum river flow also in the boreholes distant from the river shoreline, at a distance of 400–600 m [*Pavlova et al., 2020*]. The highest levels of suprapermafrost groundwater are observed in the areas, where lakes previously existed.

The rise of water level in the boreholes at such a distance can only be explained by transfer of pressure from the river along the under-channel taliks connected with the taliks of the buried ancient lakes. Annual extremes of the level regime of groundwater lag behind river water by 35–63 days. The rate of hydrodynamic impulse spreading from the river along the aquifer was calculated on the basis of the regime ob-

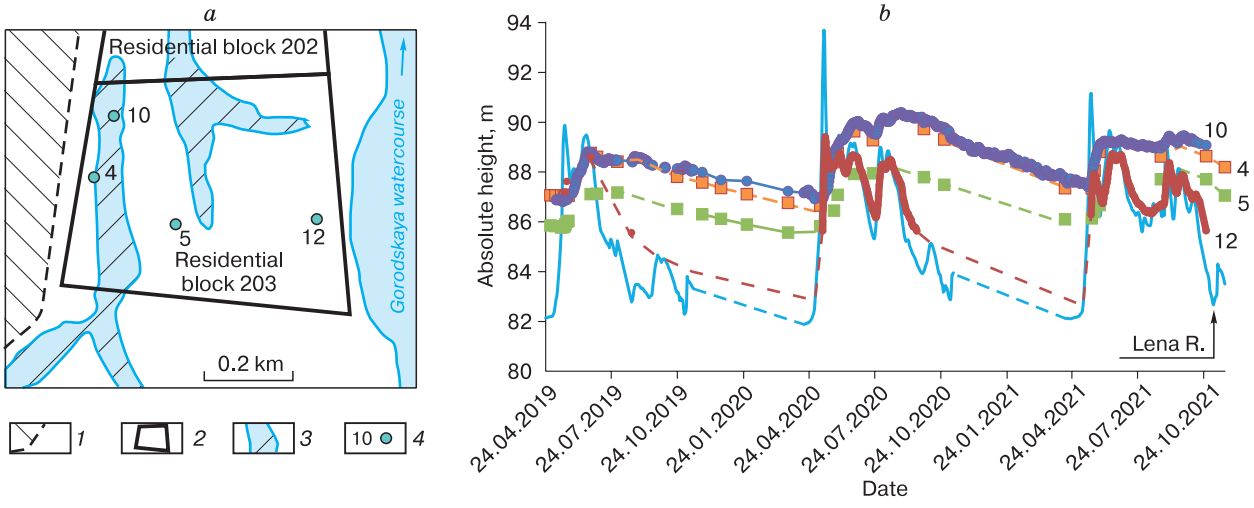

Fig. 3. Location of hydrogeological monitoring boreholes (*a*) and the plot of changes in the level of suprapermafrost groundwater in the floodplain-reclaimed area of Yakutsk and the Lena River (Yakutsk gauging station) in 2019–2021 (*b*).

(*1*) first terrace of the Lena River, (*2*) contour of the reclaimed area, (*3*) oxbow lakes buried during reclamation, (*4*) hydrogeological monitoring boreholes. Symbol and number on the plot correspond to the hydrogeological borehole and its number on the scheme.

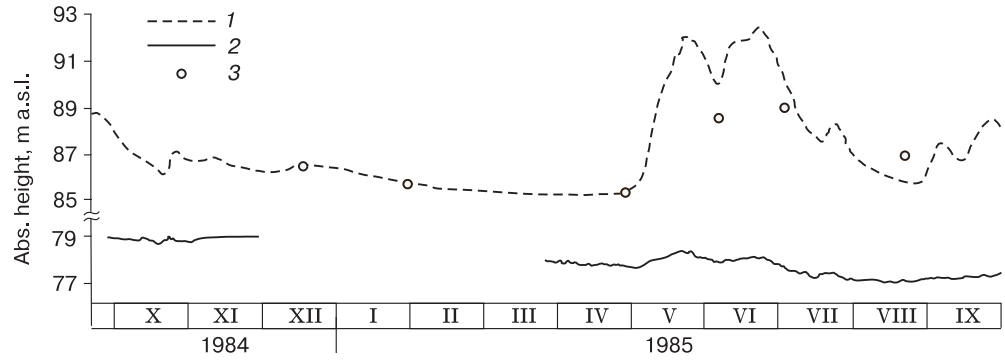

Fig. 4. Graph of changes in the water level in the (*1*) Lena River and (*2*) boreholes equipped for the Lower and Middle Cambrian aquifer on the high floodplain of the Lena River and on (*3*) Peschanyi Island.

Based on the archive materials of the Sakhageoinform unitary enterprise and the Melnikov Permafrost Institute, Siberian Branch of the Russian Academy of Sciences.

servations; it is about 4.6×10^3 m^2/day. The similar hydrodynamic regime of groundwater can be expected in the suprapermafrost taliks on islands and reclaimed areas in the river floodplain.

The groundwater regime of the Lower–Middle Cambrian aquifer complex was studied in the area of the open under-channel talik of Tabaga Cape in the 1980s by the employees of "Yakutskgeologiya" PGO. As a result of these studies, it was found that the change in the piezometric level of groundwater is synchronous with the fluctuations in the Lena River level. The influence of the river on the hydrodynamic regime of subpermafrost water can be traced in the borehole drilled on the high floodplain (Fig. 4). On the low terraces, the level of subpermafrost waters is not affected by seasonal changes and is closely related to water intake from the production boreholes [*Shepelev et al., 2002*].

Suprapermafrost groundwater is generally characterized by pressure-free regime under the freezing small rivers and waterbodies [*Anisimova, Pavlova, 2014*]. From July to March, as long as the conditions exist for their water filtration through the strata and the boundary of the freezing layer does not reach water-bearing rocks, the groundwater has the free surface. When the aquifer freezes, the cryogenic pressure appears in the talik and reaches its maximum value in May–June.

Quality of surface water and groundwater of the suprapermafrost taliks

The chemical composition of water in the Lena River depends on its feeding conditions. In spring and summer, when the river runoff is formed generally due to snow melting and liquid precipitation, the surface water mineralization is 70–100 mg/L with chloride–bicarbonate sodium–calcium or magnesium–calcium composition. By the end of summer, the concentration of dissolved substances increases to 170–180 mg/L. The ratio of anions in water does not change. Its cationic composition becomes mostly sodium–calcium near Yakutsk and magnesium–calcium near the right bank (Table 1). The probable reason for such variability is the inflow of small rivers with bicarbonate calcium–magnesium water from the right bank into the Lena River. In winter, during transition to the underground feeding, the water mineralization in the Lena River fairway is about 300–500 mg/L; in

Table 1. **Chemical composition of water in the Lena River watercourses**

Watercourse	pH	Sum of mineral dissolved solids, mg/L	Ca^{2+}	Mg^{2+}	Na^{+}	K^{+}	HCO	SO	Cl
Tabaga	7.5	164	24 45	7 22	20 33	1 0	107 59	18 13	29 28
Gorodskaya	7.0	138	20 45	5 19	18 36	1 0	94 62	8 7	28 31
Rassoloda	7.4	147	30 55	12 35	6 9	1 1	159 96	<1 0	5 4
Khaptagai	7.7	161	28 50	10 31	12 19	1 0	159 83	9 6	12 11

N o t e: Numerator, mg/L; denominator, % (meq).

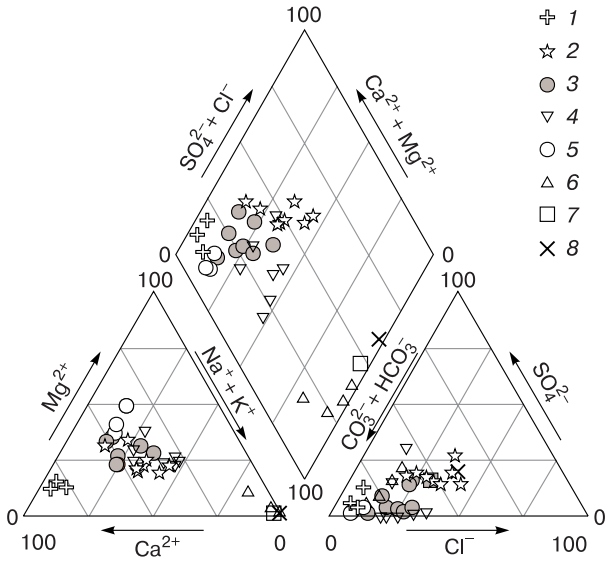

Fig. 5. Piper diagram of the macrocomponent composition of natural waters.

(*1*) atmospheric precipitation (rain); (*2*) Lena River, (*3–5*) suprapermafrost groundwater of the Quaternary aquifer under the Lena River watercourses, in the reclaimed floodplain area of Yakutsk (left bank of the Lena River), and under the Tamma River channel and floodplain (right bank of the Lena River), respectively; (*6*) suprapermafrost groundwater of the Middle Jurassic aquifer; and (*7, 8*) interpermafrost water of the open under-channel talik of the Lena River within the Lower Jurassic (sampling interval 106–261 m) and Cambrian (sampling interval 261–320 m) aquifers, respectively.

the channels near Yakutsk, it is up to 800 mg/L. The chemical composition of water is transformed to chloride–bicarbonate calcium–sodium.

In the suprapermafrost underwater talik of the Lena River, in the upper part of the Quaternary aquifer, the concentration of dissolved substances in water is 0.4–0.8 g/L [*Anisimova et al., 2005*]. In the annual cycle, the fractional ratio of main anions and cations changes according to the composition of the feeding river water.

The groundwater quality of the Middle Jurassic aquifer is formed under the conditions of relatively slow water exchange. Consequently, their mineralization increases to 0.8–1.1 g/L; alkalinity becomes higher (pH 7.7–8.4), and sodium steadily prevails over other cations (up to 87–98%) (Fig. 5).

In the subpermafrost open talik of the Lena River near Tabaga Cape, the water mineralization also increases along the section from 0.6 g/L in the top of the Lower Jurassic aquifer complex to 1.3 g/L in the Lower Cambrian aquifer complex [*Balobaev et al., 2003*]. The anionic composition of water changes in depth from bicarbonate to chloride–bicarbonate in the Jurassic sediments, while in the Cambrian aquifer complex, it becomes bicarbonate–chloride (Table 2). Regardless of the lithology and rock age, sodium ions prevail in the groundwater of the open talik among cations; their share increases with depth from 81 to 98%. Relatively low water mineralization in the under-channel sediments, as compared to the subglacial

Table 2. **Chemical composition of groundwater in the area of Tabaga Cape**

Location	Symbol of aquifer; sampling depth, m	HCO	Cl^-	SO	Ca^{2+}	Mg^{2+}	$(Na+K)^+$	F^-	pH	M, mg/L
				Open subchannel talik						
Peschanyi Is.	J_1 24–105	358/84	31/12	13/4	11/7	8.7/10	143/83	1.4/–	8.4	599
	J_1 106–261	344/53	134/31	93/16	6/2	2/1	270/97	í /ä/–	8.5	725
	$Є_1 + Є_2$ 261–320	465/43	249/37	184/22	8/1	6/1	417/98	1.8/–	8.6	1346
				Subpermafrost water, left bank of the Lena River						
Tabaga settlement	J_1 172–267	613/50	392/48	24/2	8/2	2/1	519/97	5.0/–	7.3	1573
	$Є_1 + Є_2$ 273–450	507/21	478/35	810/44	175/22	63/13	661/65	2.2/–	7.9	2701
				Subpermafrost water, left bank of the Lena River						
Khaptagai settlement	$Є_2$ 320–500	604/27	269/21	909/52	34/5	35/8	428/87	2.5/–	7.3	2280

Note: Numerator, mg/dm^3; denominator, % (equiv,); nd – no data; M – mineralization.

aquifer complexes, is the result of surface water infiltration along the open talik.

In the taliks under shallow watercourses, oxbow lakes, and small tributaries of the Lena River, the chemical composition of suprapermafrost water depends on the degree of flowability of watercourses and water bodies. With good water exchange, the composition is close to the composition of the Lena River under-channel waters. Therefore, on the right-bank floodplain of the river, the water mineralization in the suprapermafrost taliks at the end of winter is 0.2–0.4 g/L, the chemical composition is mostly magnesium–calcium bicarbonate. Water in under-channel taliks of small rivers (Tamma and Menda), has a similar composition in winter.

In the taliks on the left-bank floodplain of the Lena River, the water mineralization is 0.5–0.8 g/L. Increased chloride-ion content (up to 25–37% of the sum of anions) and predomination of sodium ions (41–45% of the sum of cations) are caused by worsening water exchange conditions and by the influence of cryogenic metamorphization processes on the composition of water. Near Yakutsk, an increase in the concentration of sulfate anions and nitrogen compounds is often noted in floodplain taliks, indicating the technogenic contamination of suprapermafrost groundwater.

CONCLUSIONS

In the area of Yakutsk, the long-term migration of the Lena River channel and its tributaries and processes of cryogenesis resulted in the local distribution of groundwater streams in the floodplain sediments that often do not coincide with the water surface in the river branches. Despite the presence of permafrost and limited distribution of suprapermafrost taliks on the river floodplain, the groundwater contained in them is hydraulically connected with the surface and under-channel waters of the Lena River. This connection is distinctly manifested during floods, when, under the backwater effect, suprapermafrost water of the floodplain taliks is recharged not so much by downward infiltration of river waters into the aquifer as by the underground flow filtered through the network of connecting taliks.

The chemical composition of water in the Lena River and its under-channel talik is variable in the lateral and vertical directions and depends on the presence of tributaries and conditions of interconnection of the surface and ground waters. The minimal mineralization is typical for the under-channel waters of the Quaternary aquifer closer to the right bank of the Lena River. Here, there are the conditions for the aquifer recharge by the suprapermafrost water from the Bestyakh terrace and under-channel taliks developed under small tributaries of the Lena River. An increase in water mineralization along the section of the under-channel talik is caused by the change in the lithological composition of water-bearing rocks and deterioration of their filtration properties with depth.

The increased concentration of sulfate and chloride ions, sodium ions, and, sometimes, nitrogen compounds in water is observed near Yakutsk, in the Lena River channels, suprapermafrost taliks under them, and in small rivers. The probable causes are the cryogenic metamorphization of water and water-bearing rocks under the conditions of poor water exchange and the input of polluted runoff from the floodplain terrace, where the city is located.

Acknowledgments. *This work was supported by the Russian Science Foundation and the Yakutia Science Foundation, grant no. 22-17-20040.*

References

Anisimova N.P., 1996. Regime studies of permafrost taliks in the vicinity of Yakutsk. In: *Cryolithozone and Groundwater of Siberia*. Vol. 2, Yakutsk, Izd. Inst. Merzlotoved. Zemli Sib. Otd. Ross. Akad. Nauk, p. 3–16 (in Russian).

Anisimova N.P., Pavlova N.A., 2014. *Hydrogeochemical studies of the cryolithozone of Central Yakutia*. Novosibirsk, Geo Publ., 189 p. (in Russian).

Anisimova N.P., Pavlova N.A., Stambovskaya Ya.V., 2005. Chemical composition of talik waters of the Middle Lena River. *Nauka i Obrazovanie* no. 4, 118–124 (in Russian).

Balobaev V.T., Ivanova L.D., Nikitina N.M. et al., 2003. *Groundwater in Central Yakutia and Prospects of Its Use*. Novosibirsk, Geo Publ., 137 p. (in Russian).

Beletsky V.L., 1975. Features of water exchange in the first from the surface aquifers of Central Yakutia. In: *Issues of Cryolithozone Hydrogeology*, Yakutsk, Izd. Inst. Merzlotoved. Sib. Otd. Akad. Nauk SSSR, p. 11–35 (in Russian).

Chalov R.S., Zavadsky A.S., Ruleva S.N. et al., 2016. Morphology, deformations and temporary modifications of the Lena River channel and its influence on the Yakutsk economic infrastructure. *Geomorfologiya*, iss. 3, 22–35 (in Russian).

Chang L., Qianlai Z., 2017. Quantifying the role of permafrost distribution in groundwater and surface water interactions using a three-dimensional hydrological model. *Arct. Antarct. Alp. Res.* **49** (1), 81–100.

Chistyakov G.E., 1952. Riverbed processes on the Lena River. In: *Permafrost Studies in the Yakutia Republic*. Vol. 3. Moscow, Izd. Akad. Nauk SSSR, p. 213–225 (in Russian).

Efimov A.I., 1964. Permafrost-hydrogeological features of the coastal and riverbed sections of the Lena River near Yakutsk. In: *Geocryological Features of West Yakutia, Yakutia and Chukotka*. Moscow, Nauka, p. 97–110 (in Russian).

Fotiev S.M., 1968. Classification of hydrogenic-class taliks. In: *Proc. Sci. Techn. Conf*. Moscow, PNIIS, p. 168–171 (in Russian).

Fotiev S.M., 2009. *Cryogenic Metamorphism of Rocks and Groundwater (Conditions and Results)*. Novosibirsk, Geo Publ., 279 p. (in Russian).

Gautier E., Dépret T., Virmoux C. et al., 2018. Going with the flow: Hydrologic response of middle Lena River (Siberia) to the climate variability and change. *J. Hydrol.* **557**, 475–488.

Hydrogeology of the USSR, 1970. Vol. XX. *Yakut ASSR*. Moscow, Nedra, 384 p. (in Russian).

Khristoforov I.I., Omelyanenko A.V., 2013. Results of georadiolocation of the bottom and bottom sediments of river crossings of linear engineering structures. *Nauka i Obrazovanie*, no. 1, 38–43 (in Russian).

Melnikov P.I., 1963. *The Results of Geocryological, Hydrogeological and Engineering-Geological Studies in Central and Southern Yakutia*. Moscow, V.A. Obruchev Perm. Inst., 84 p. (in Russian).

Mikhailov V.M., 2013. *Floodplain taliks of the Northeast of Russia*. Novosibirsk, Geo Publ., 244 p. (in Russian).

Pavlova N., Ogonerov V., Danzanova M. et al., 2020. Hydrogeology of reclaimed floodplain in a permafrost area, Yakutsk, Russia. *Geosciences* **10** (5), 192.

Roman L.T., Tsernant A.A., Poleshhuk V.L. et al., 2008. *Construction on Alluvial Soils in the Cryolithozone*. Moscow, Izd. Ekonomika, Stroitelstvo, Transport, 323 p. (in Russian).

Romanovskii N.N., 1983. *Groundwater in the Cryolithozone*. Moscow, Izd. Mosk. Gos. Univ., 231 p. (in Russian).

Shepelev V.V., 2011. *Suprapermafrost Water in the Cryolithozone*. Novosibirsk, Geo Publ., 169 p. (in Russian).

Shepelev V.V., 2021. Analysis of the cryolithozone effect on water exchange processes. *Nauki o Zemle i Nedropol'zovanie* **44** (2), 184–190 (in Russian).

Shepelev V.V., Boitsov A.V., Oberman N.G. et al., 2002. *Monitoring of Groundwater in the Cryolithozone*. Yakutsk, Izd. Inst. Merzlotoved. Sib. Otd. Ross. Akad. Nauk, 172 p. (in Russian).

Shepelev N.G., Makogonova O.V., 2010. Modeling of hydrogeological conditions of a subpermafrost aquifer for the Yakutsk territory. *Nauka i Obrazovanie*, no. 2 (58), 21–26 (in Russian).

Shesternev D.M., Zhang R.V., Kuzmin G.P. et al., 2014. Industrial and residential construction on hydraulic fill in permafrost regions; problems and prospects. *J. Engin. Heilongjiang Univ.*, no. 5 (3), 100–109.

Stognii V.V., 2003. *Pulsed Inductive Electrical Survey of Taliks in the Cryolithozone of Central Yakutia*. Yakutsk, Academy, 124 p. (in Russian).

Tananaev N.I., 2005. Hydrometeorological conditions of frozen soils formation in the middle Lena riverbed. *Moscow Univ. Byull. Ser. 5, Geografiya*, no. 6, 60–64 (in Russian).

Tananaev N., 2016. Hydrological and sedimentary controls over fluvial thermal erosion, the Lena River, Central Yakutia. *Geomorphology* **253**, 524–533.

Received April 27, 2022
Revised November 28, 2022
Accepted December 8, 2022

Translated by V.A. Krutikova

EARTH'S CRYOSPHERE
SCIENTIFIC JOURNAL

Earth's Cryosphere, 2023, vol. XXVII, No. 1, pp. 39–50

SNOW COVER AND GLACIERS

DYNAMICS OF LAKES OF THE BOLSHOY AZAU GLACIER ON ELBRUS

A.Kh. Adzhiev[1], M.Yu. Bekkiev[1], M.D. Dokukin[1,*], R.Kh. Kalov[1], E.A. Savernyuk[2], S.I. Shagin[3]

[1] *High-Mountain Geophysical Institute, prosp. Lenina 2, Nalchik, 360030 Russia*
[2] *Lomonosov Moscow State University, Faculty of Geography, Leninskie Gory 1, Moscow, 119991 Russia*
[3] *Berbekov Kabardino-Balkarian State University, Department of Scientific Research and Innovation, Tolstogo St. 175a, Nalchik, 360004 Russia*

**Corresponding author; e-mail: inrush@bk.ru*

High rates of degradation of the Bolshoy Azau Glacier on Elbrus make it necessary to assess the development of lakes on the ice-free land and on the glacier itself. For this purpose, aerospace data for the period of 1957–2021, as well as information from visual observations, Internet sources, and tourist photos were analyzed. The existence of 15 lakes with an area of 140–20 250 m^2 on the Bolshoy Azau Glacier and the adjacent territory was recorded at various times. The long-term existence of the lake in contact with the glacier on the Echo of the War mountain passage covering with an area of up to 4500 m^2 was revealed for the period of 1971–2009. The maximum area (20 250 m^2) was detected on a satellite image from June 25, 2009 for a lake on the dead ice part of the median moraine between left and right ice streams of the Bolshoy Azau Glacier. In the hollows on the glacier surface, up to three lakes with a maximum total area of 7860 m^2 were observed in different times. Lakes on the Bolshoy Azau Glacier appeared mainly during the snow cover melting, while masses of drifted snow served as dams in the drainage area of hollows. These lakes disappeared after melting of drifted snow dams and/or in the course of drainage through subglacial and underground runoff channels.

Keywords: *glacier, satellite images, glacial lake, drainage channel, snow cover, lake basin.*

Recommended citation: Adzhiev A.H., Bekkiev M.Yu., Dokukin M.D., Kalov R.Kh., Savernyuk E.A., Shagin S.I., 2023. Dynamics of Lakes of the Bolshoy Azau Glacier on Elbrus. *Earth's Cryosphere* XXVII (1), 39–50.

INTRODUCTION

Climate warming and succeeding degradation of glaciers induce the formation on new lakes posing a significant risk of outbursts and floods that may led to natural disasters with a large number of human casualties – up to 4000–6000 people [*Allen et al., 2016; Mergili et al., 2020*]. According to [*Emmer, 2018*], 892 scientific papers on the subject of lake outbursts were recorded in the Web of Science database for the period of 1979–2016. One of the recent examples is an outburst of Lake Bashkara in the Caucasus that led to the catastrophe in 2017 [*Chernomorets et al., 2018*].

The other instances happened to the lakes that were formed in front of the Elbrus glaciers. They repeatedly broke through in the upper reaches of the Birdzhalysu River in 1909, 1973, 1983, 1993, 1999, 2003, and 2006 [*Gerasimov, 1909; Chernomorets et al., 2007; Dokukin et al., 2012, 2022*]; in the upper reaches of the Garabashi River Azau Basin in 1895 [*Ivanov, 1902*], in 1912, and 1947; and in the upper reaches of the Malaya Azau River in 1978 and 2011 [*Seynova, Zolotarev, 2001; Dokukin et al., 2016*].

The rate of degradation of the Elbrus glaciers has increased significantly in the 21st century [*Kutuzov et al., 2019; Bekkiev et al., 2021*]. Significant risks of emergence and outburst of lakes in front of the Bolshoy Azau Glacier were discussed by Vasil'chuk with coauthors [*Vasil'chuk et al., 2010*]. In order to estimate the scale and rate of lake formation on the ice-free land of the Bolshoy Azau Glacier and on the glacier itself, multitemporal satellite images and available data of aerial surveys, Internet data, information and photos from travelers were analyzed.

MATERIALS AND METHODS

Aerial photos, satellite images, topographic maps and orthophotomaps, photos from helicopter, and ground photos of various authors were used in our study (Table 1).

Satellite images and aerial photos were transformed using SPLINE transformation and reference points to the WGS 84 coordinate system in the UTM zone 38N in the ArcMap 10.7 program; lakes were vectorized, and their areas were determined. Measurement errors were estimated via triple delineation of the lakes. On the Sentinel-2 and Landsat 5-8 satellite images, the lakes were more clearly displayed using false color (false color, bands 8, 4, 3). Depending on the characteristics of satellite images, the clarity of

Table 1. **Materials used**

Materials	Year/Data	Scale, resolution, m (MS/Panchromatic)	Source, copyright holder
Aerial photographs	Aug. 22, 1957; Sept. 8, 1973, 1975; Aug. 17, 1983; July 27, 1988	1:25 000	Archive of the Federal State Budgetary Institution "High Mountain Geophysical Institute"
Topographic maps	1958	1:10 000	*Atlas of Elbrus Glaciers*. [*1965*]
	2012	1:5000	Aerotech JSC
Orthophotomaps	1997	1:10 000	I.A. Labutina, E.A. Zolotarev et al.
	Sept. 28, 2012	1:5000	Aerotech JSC
Satellite images			
KH-4B (Corona)	Sept. 20, 1971	1.8	Site EarthExplorer [https://earthexplorer.usgs.gov/]
Landsat 7	Aug. 9, 1999; Sept. 12, 2000	30/15	
IRS P5	Sept. 12, 2007	2.5	© 2003-2007 ANTRIX
IRS 1C/1D	Aug. 1, 2006; Aug. 11, 2006	23/5.8	© 2006 National Remote Sensing Centre, Department of Space, Government of India
EROS A	July 20, 2007	1.8	© 2007 ImageSat International N.V.
SPOT 5	Sept. 21, 2011	10/2.5	© CNES 2011
GeoEye-1[6]	Sept. 19, 2009; Oct. 16, 2009; Sept. 23, 2014	1.64/0.41	© GeoEye, Inc.
GeoEye-1	Feb. 15, 2014; Sept. 12, 2015	1.64/0.41	World Imagery [http://goto.arcgisonline.com/maps/World_Imagery]
WorldView2	Aug. 31, 2010	1.84/0.46	
Pleiades-1A	Sept. 6, 2014	2/0.5	© CNES 2014
Pleiades-1B	Aug. 23,2015		© CNES 2015
Sentinel-2	**2015–2021**	20/10	Site Sentinel Hub EO Browser [https://apps.sentinel-hub.com/eo-browser/]
Landsat-5	**2009**	82/30	
Landsat-8	**2013–2015**	30/15	
Resurs P	Aug. 19. 2016	3/1	Research Center for Space Hydrometeorology "PLANETA"
Kanopus B5	Sept. 15, 2020	10.5/2.1	
Ground photographs	Aug. 29, 1973;	–	V.F. Sukomeilo
	July 1985;	–	uz89 [https://risk.ru/blog/198343]
	Aug. 27, 2008;	–	A. Lebedev
	June 7, 2020	–	K. Lagodienko
	2009–2012	–	Ya. Berezhko
Helicopter photos	June 18, 2009; June 17, 2011; June 23, 2015	–	M.D. Dokukin

Note: MS, multispectral images. Images from IRS, EROS, SPOT, GeoEye, and Pleiades satellite were kindly provided by the SCANEX Engineering and Technology Center. Dashes mean that the photos were made with different models of digital and SLR cameras.

coastlines, and the shape of the lakes, the measurement errors varied from 1 to 33% (mostly, up to 10%). The absolute heights of the lakes were determined according to the topographic map of 2012 on a scale of 1:5000.

The comparative interpretation of multitemporal images was carried out using the Swipe Layer tool for interactive display of multitemporal layers in the ArcMap program and in the GIF animation mode of the Easy GIF Animator Pro to reveal changes in the state of lakes and their basins, identify areas of dead ice, and determine glacier boundaries.

RESULTS

According to [*Bekkiev et al., 2021*], the area of the Bolshoy Azau Glacier decreased by 6.35 km^2 from 1957 to 2020, taking into account the reduction of the tongue of the glacier descending into the Ulukam River valley. In 2011–2021, the decrease in the area of the Bolshoy Azau Glacier, including areas on the border of the Bolshoy and Maly Azau Glaciers, amounted to 2.21 km^2 (almost 35% of the total area loss for 1957–2021). To the western and central areas of maximum deglaciation, the area of the formed massif of dead ice from the middle moraines was added. It

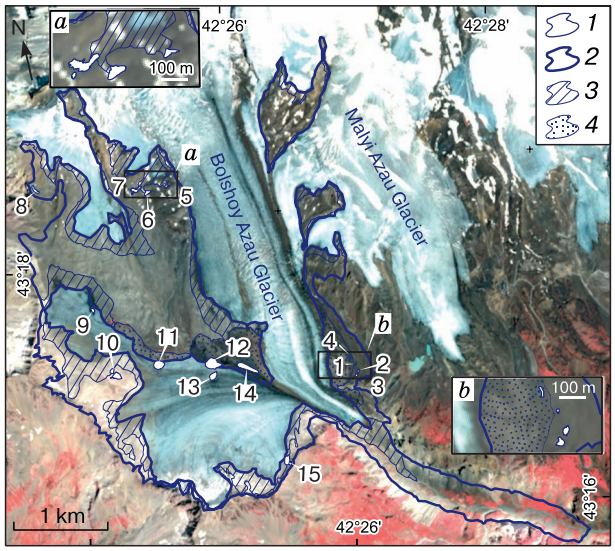

Fig. 1. Degradation of the Bolshoy Azau Glacier for 1957–2021 and formed lakes on Sentinel-2 image from August 27, 2021:

(*a*) Enlarged fragment of the north lakes area; (*b*) enlarged fragment of the east lakes area. Lake numbers are given in Table 2. *1* – lakes, *2* – areas freed from ice in 1957–2021, *3* – ice-free areas in 2011–2021, *4* – dead ice.

Table 2. **Characteristics of lakes of the Bolshoy Azau Glacier**

No.	Coordinates	Height, m a.s.l.	Maximum area, thousand m^2	Date
		East lakes		
1	N43°17′07,89″ E42°26′22,54″	3251	0.14 ± 0.012	Sept. 19, 2009
2	N43°17′05,07″ E42°26′22,97″	3247	0.59 ± 0.03	Aug. 31, 2010
3	N43°17′04,02″ E42°26′21,71″	3244	0.67 ± 0.007	June 23, 2015
4	N43°17′10,81″ E42°26′20,80″	3262	0.41 ± 0.010	Sept. 15, 2020
		North lakes		
5	N43°18′20,46″ E42°25′11,30″	3637	1.12 ± 0.07	Sept. 12, 2015
6	N43°18′19,64″ E42°25′02,18″	3637	2.43 ± 0.024	Sept. 28, 2012
7	N43°18′20,97″ E42°24′57,12″	3638	3.86 ± 0.10 0.43 ± 0.041	Sept. 12, 2015
8	N43°18′28,09″ E42°24′10,25″	3600	2.20 ± 0.18	Aug. 27, 2021
		Lakes in the Khotyutau Circus and the massif of median moraines		
9	N43°17′43,11″ E42°24′25,79″	3385	2.56 ± 0.55	June 7, 2017
10	N43°17′21,30″ E42°24′30,05″	3349	3.50 ± 0.15	July 20, 2007
11	N43°17′20,31″ E42°24′50,83″	3260	7.96 ± 0.97	June 19, 2016
12	N43°17′18,51″ E42°25′16,60″	3250–3255	20.25 ± 1.03	June 25, 2009
13	N43°17′13,99″ E42°25′14,97″	3255–3260	6.28 ± 1.02	June 2, 2019
14	N43°17′13,55″ E42°25′31,03″	3255	14.92 ± 5.01	June 19, 2016
		Lake on the Echo of War Passage		
15	N43°16′40,32″ E42°25′41,90″	3315	4.54 ± 0.07	July 20, 2007

was identified from the absence of ice movement during the analysis of glacier dynamics in ArcMap and GIF animations.

Figure 1 shows the zones of deglaciation and lakes that existed in different periods in these areas and on the Bolshoy Azau Glacier itself. A total of 15 lakes were identified: 4 lakes in the eastern section, 4 lakes in the northern section, 6 lakes in the Khotyutau Circus and in the section of median moraines, and 1 lake at the Echo of War Pass. The characteristics of the lakes are presented in Table 2.

East Lakes (nos. 1–4)

The lakes appeared following the retreat of the left edge of the glacier in the 21st century depressions of the initial relief covered with moraine. The first mention about these lakes and their photos of 2008 were received from A. Lebedev. Because of their size, ultrahigh resolution satellite images were used to study their dynamics (Fig. 2).

A specific feature of the dynamics of these lakes is the disappearance of Lake 2 in the second half of September (Fig. 2*b*, September 19, 2009; Fig. 2*d*, September 23, 2014) despite its presence in August and the beginning of September (Fig. 2*c*, August 31, 2010; Fig. 2*e*, August 23, 2015).

One of the explanations is that the main water flow from the glacier passes beyond Lake 2 and enters the basin due to channel branching during the maximum water level in July–August. In that period, the area of the lake reached 600 m^2. However, in late August–early September, a light-colored strip appeared on satellite images near the lake indicating a decrease in the water level. Lake 2 was clearly seen on images of 2016–2019 and was not seen on images of 2020–2021. In 2014–2015, water stopped flowing into the basin of Lake 1, which had already been filled with glaciofluvial sediments by that time.

Lake 3 was identified from an indirect sign – the appearance of a light-colored area on the image of 2015 in place, where no indication of the lake existence could be found in previous years (Fig. 2*e*). The existence of Lake 3 was confirmed by data of a helicopter flight on June 23, 2015: in this place, a reservoir with numerous ice floes was seen in the depression covered with snow. In subsequent years, Lake 3 could be seen on Sentinel-2 images made during the

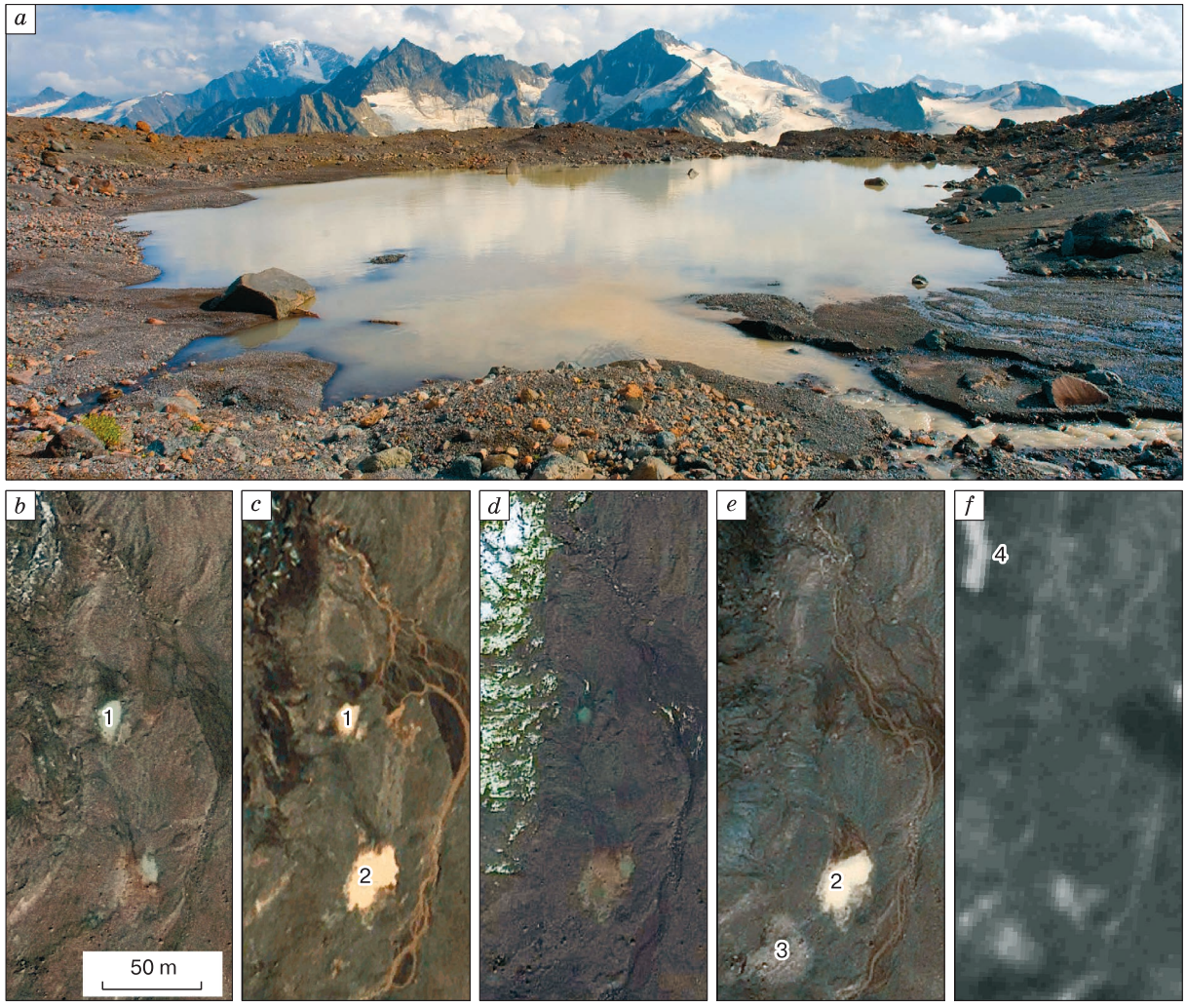

Fig. 2. Lakes to the east of the Bolshoy Azau Glacier:

(*a*) Lake 2, photo by A. Lebedev (Aug. 27, 2008); satellite images: (*b*) GeoEye-1 (Sept. 19, 2009), (*c*) WorldView2 (Aug. 31. 2010), (*d*) GeoEye-1 (Sept. 23, 2014), (*e*) Pleiades (Aug. 23, 2015), and (*f*) Canopus B5 (Sept. 15, 2020). Lake numbers correspond to Fig. 1 and Table 2.

snowmelt season in June–early July. Lake 4 appeared on the site of dead ice in 2020 and was still present in 2021 (Fig. 2*f*).

North Lakes (nos. 5–8)

The dynamics of the North lakes are shown in Fig. 3, and their areas are presented in Table 2. The formation of the lakes began in 2007 following the retreat of the glacier from the territory of the lava flow; several local depressions formed on its surface. By 2012, the glacier and dead ice partially covered basins of lakes 5 and 7 (Fig. 3*a*). By that year, Lake 6 had reached its maximum area. In 2015, lakes 5 and 7 reached their maximum sizes (Fig. 3*c*). However, Lake 6 disappeared after the water inflow from the glacier discontinues because of changes in the local landscape features.

At the same time, the satellite image from February 2014 (Fig. 3*b*) shows that all these lakes were absent in winter, which can be explained by the underground runoff from the lakes as noted in [*Dokukin, Shagin, 2014*].

The area of Lake 5 changed little during summer seasons until 2021. Just the opposite, lake 7 experienced considerable fluctuations; thus, in August 2019 and 2020, its area decreased from 3900 to 1100–1200 m^2. This can be explained by the fact that the main runoff from the glacier no longer fell into the basin. This lake is fed by two residual glaciers, the runoff from which into the lake at the end of summer becomes lower than the outflow from the lake through underground channels.

At the end of August 2021, there were still snowfields on the site of the lakes, and they were melting

and kept feeding Lake 7 at a high level. The area of the lake began to decrease gradually after September 4, 2021 as a result of cooling and decreased sharply only at the end of September. The same rapid reduction in area was observed in the second half of August 2020 for Lake 8, which formed in the 1980s.

Lakes in the Hotyutau circus and on the massif of median moraines (nos. 9–14)

Lake 9 was identified on a photo by an unknown author dated 1991. The lake was recorded on the surface of the Bolshoy Azau Glacier during the flight on June 17, 2011 and on satellite images in subsequent years at the beginning of summer. Below the lake basin, there is a permanent channel developed by the water flow on the surface of the glacier.

Lake 10 appeared on the surface of the bedrock (crossbar) covered by moraine following the retreat of the glacier to the lower levels. The dynamics of the lake was studied using high and ultrahigh resolution images (Fig. 4).

Comparison of satellite images with the topographic map (scale 1:5000) showed that the water level in the lake decreased by 5 m in the period from 2007 to 2012. In 2007, the maximum depth of the lake was 3.5 m. The glacier dammed the lake from the northwestern side. In 2007, the surface flow from the lake towards southeast was formed. As the glacier retreated, the lake continued to exist, but the surface flow from it stopped.

Comparison between the helicopter image made on June 17, 2011 (Fig. 4*d*) and the satellite image from September 21, 2011 demonstrated a sharp decrease in the area from 3210 to 1750 m^2 in 2011, when arc cracks appeared on the surface of the glacier and the lake water level dropped by 4 m. Such cracks indicate that there was a grotto filled with lake water under the surface of the glacier, the roof of which then collapsed. Subsequently, the remaining small lake existed until 2015 (area 1000 m^2 on September 12, 2015) and then disappeared.

Lake 11 was recorded on a satellite image from July 20, 2007 (Fig. 5*a*); its boundaries were identified on a helicopter image from June 17, 2011 (Fig. 5*d*).

On satellite images of 2013–2015, this lake could not be identified. In 2016, the lake appeared on May 30 and reached its maximum area of about 8000 m^2 on June 19–22 (Fig. 5*b*). Then, the lake considerably shrunk and disappeared by the early July. In 2017 and 2018, it existed for a short time and its area was less than 100–200 m^2. In 2019, the lake existed in May with an area of up to 2000 m^2; in June, its area was minimal (Fig. 5*c*). In 2020 and 2021, the lake was absent.

Lake 12 formed in a thermokarst funnel in the area of dead ice in the massif of median moraines (Fig. 6).

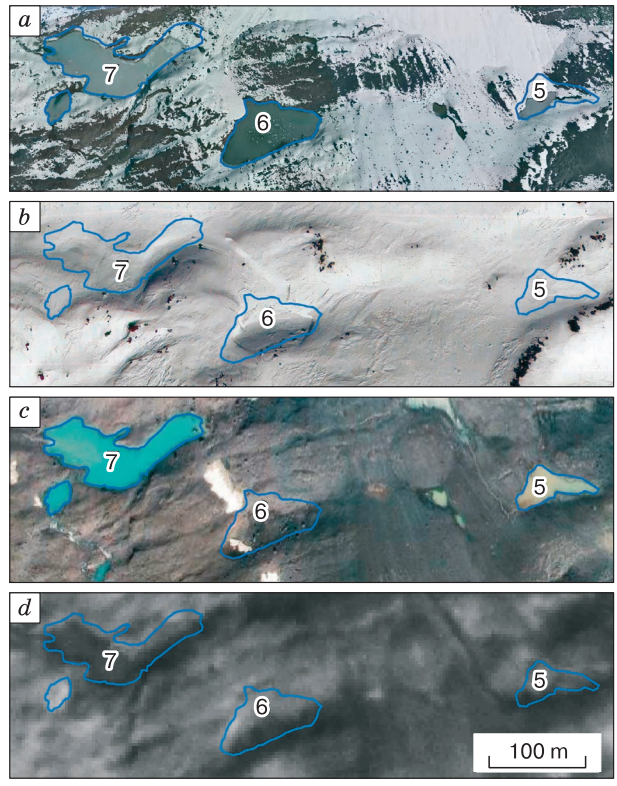

Fig. 3. North group of lakes:

(*a*) Aerial photo from Aerotech JSC (Sept. 28, 2012), (*b*) GeoEye-1 image (Feb. 15, 2014), (*c*) GeoEye-1 image (Dec. 9, 2015), and (*d*) Canopus B5 image (Sept. 15, 2020). Boundaries of lakes 5 and 7 are drawn according to data of 2015; boundaries of Lake 6 are drawn according to data of 2012.

On the satellite image from July 20, 2007 (Fig. 6*c*), traces of lake 12 were seen as an oval-shaped line on the snow-covered surface of the glacier. The lake was identified during the flight on June 18, 2009 (Fig. 6*a*). Its area exceeded 12 000 m^2. The maximum area of the lake was found on the Landsat-5 image from June 25, 2009; it reached 20 000 m^2 (Fig. 6*d*). On the photo from June 17, 2011 and on the satellite image from September 21, 2011, this lake was no longer found (Figs. 6*b* and 6*e*).

A comparison between two satellite images from August 11, 2006 (5.8 m resolution) and September 19, 2009 revealed similar features of a thermokarst funnel with fresh edges and walls, which suggests that the lake already existed in 2006. A clear boundary is visible on the snow-covered sections of the funnel walls on the helicopter image from June 17, 2011 (Fig. 6*b*); it can be interpreted as a fresh trace of the existence of the lake. The lake was clearly identified on satellite images from May 28 and June 13, 2013; its area was more than 12 000 m^2 (Fig. 6*f*). According to the contour line of the lake on the topographic map of 2012, the volume of the lake in 2013

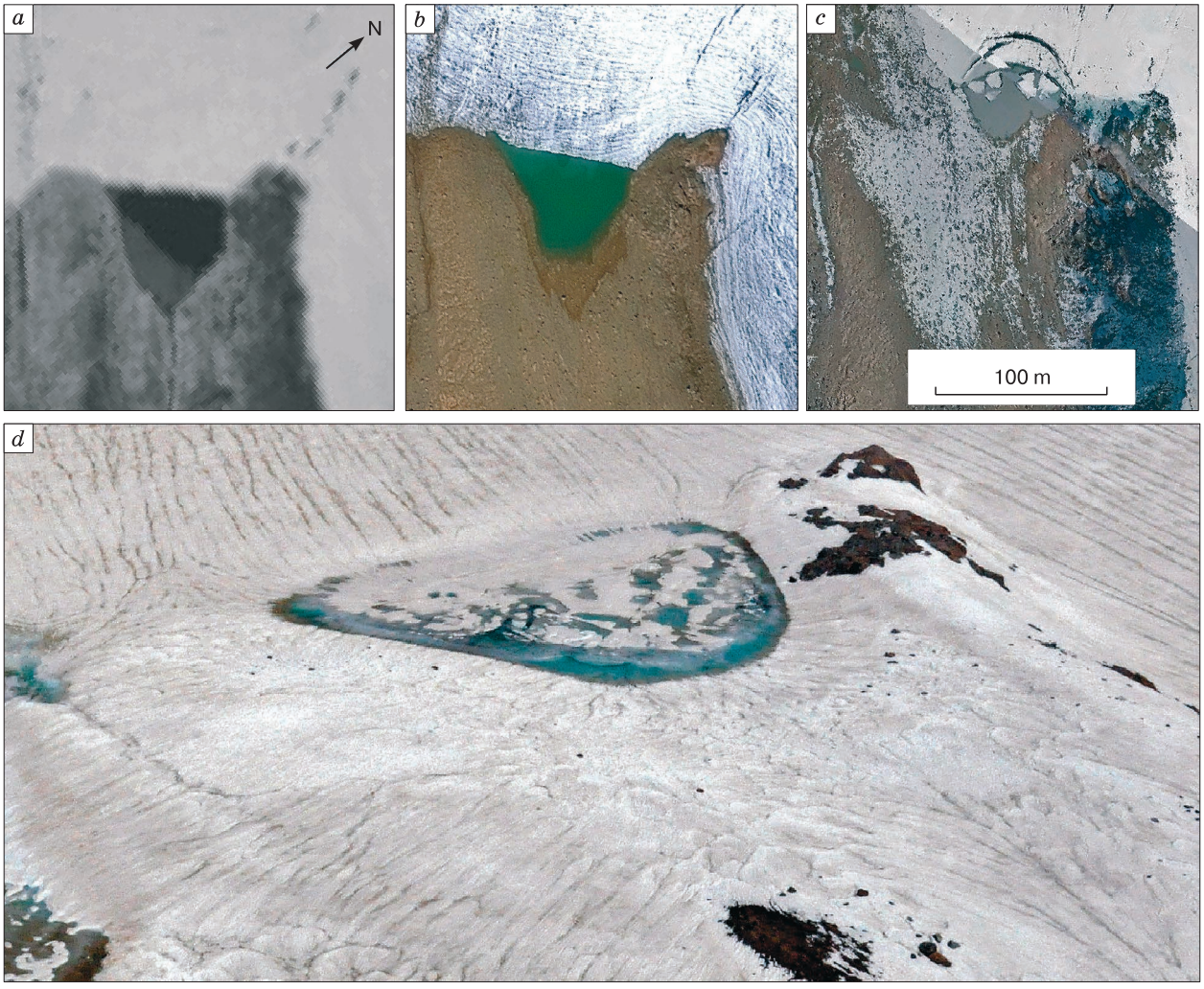

Fig. 4. Lake 10 at the rock bar in the Khotyutau Circus:

(*a*) EROS A image (July 20, 2007), (*b*) GeoEye-1 image (Sept. 19, 2009), (*c*) aerial photo from Aerotech JSC (Sept. 28, 2012), and (*d*) photo by M.D. Dokukin (June 17, 2011).

was estimated at about 52 000 m^3; the depth was up to 15–17 m. At the end of June 2013, the lake disappeared. It appeared again in June 2017 and existed throughout June. It covered an area of 8400 m^2 on June 2. Much smaller lake area (<4000 m^2) was observed on June 2, 2019. In subsequent years, Lake 12 did not appear on the analyzed materials.

A depression on the glacier surface in the area of Lake 13 began forming in 2017. The first lake with an area of less than 1000 m^2 appeared in June 2018. In 2019, the lake of the same area appeared on May 13 and began expanding. By the end of May, the area of the lake covered with ice floes reached 6300 m^2 (Fig. 5*c*).

The size of the lake did not change throughout June. Then, with the release of the glacier from snow, the area of the lake decreased to 2000–2200 m^2. The lake existed on the surface of the glacier until the middle of September 2019. In 2020, it existed from the end of May until July 25 without considerable fluctuations in size (about 3300 m^2). In 2021, despite the increase in the depression, the area of the lake did not exceed 2000 m^2 from the end of May to the end of June (Fig. 5*e*).

Lake 14, about 200 m long, was identified on a satellite image from May 31, 2014. In 2015, the boundaries of the lake could be hardly observed. In 2016, the lake existed in June; on June 19, its area reached 14 920 m^2 with a length of 300 m and a width of 50 m (Fig. 5*b*). At the end of June, the lake disappeared. In 2017, the lake appeared on May 8 and had a length of 150 m. In late May–early June 2017, the lake reached its usual size (length 240 m) and disappeared in early July. On May 3, 2018, the lake was

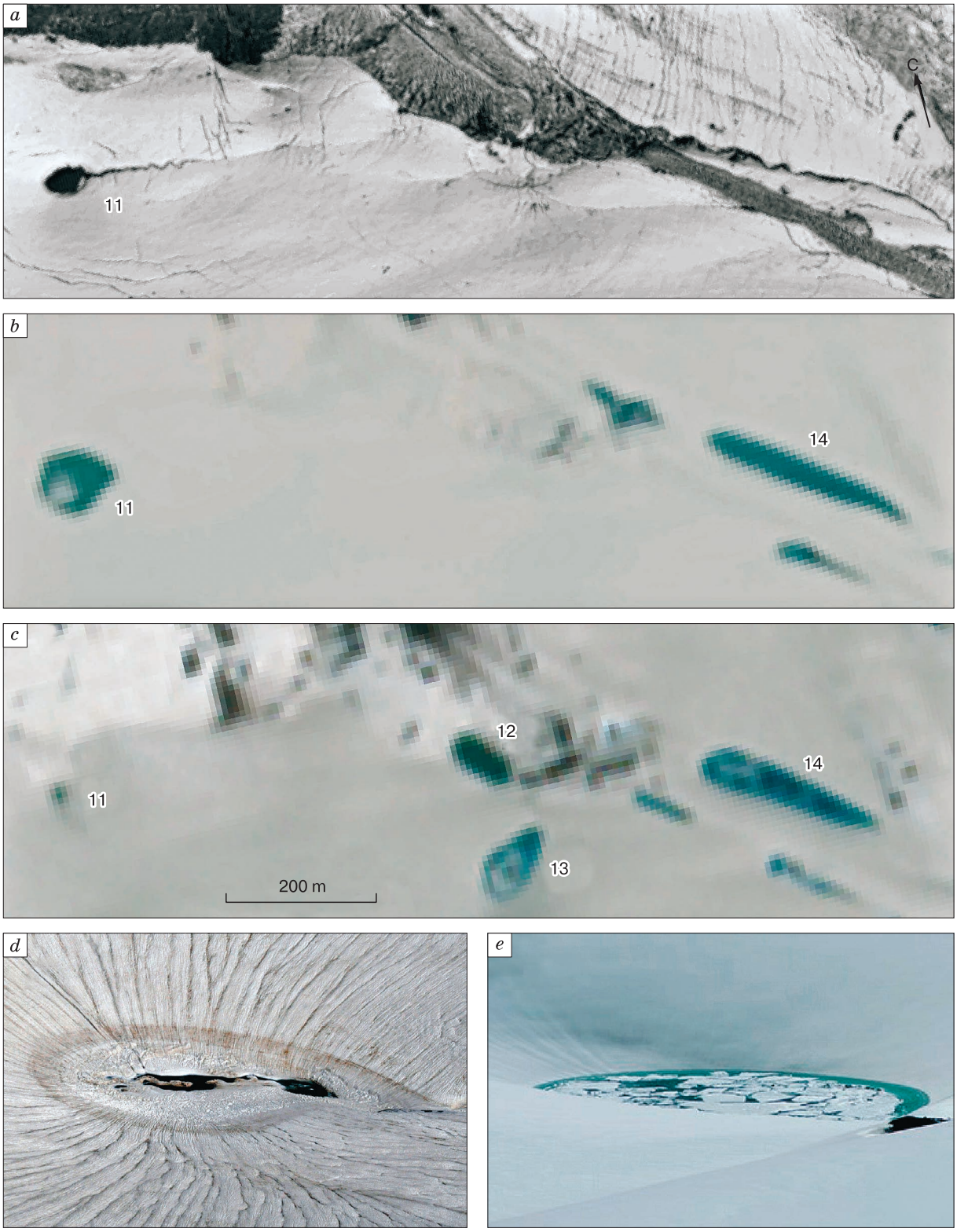

Fig. 5. Lakes on the Bolshoy Azau Glacier and on the dead ice massif of median moraines:

(*a*) EROS A image (June 20, 2007), (*b*) Sentinel-2 image (June 19, 2016), (*c*) Sentinel-2 image (June 2, 2019), (*d*) traces of Lake 11, photo by M.D. Dokukin (June 17, 2011), and (*e*) Lake 13, photo by K. Lagodienko (June 7, 2020).

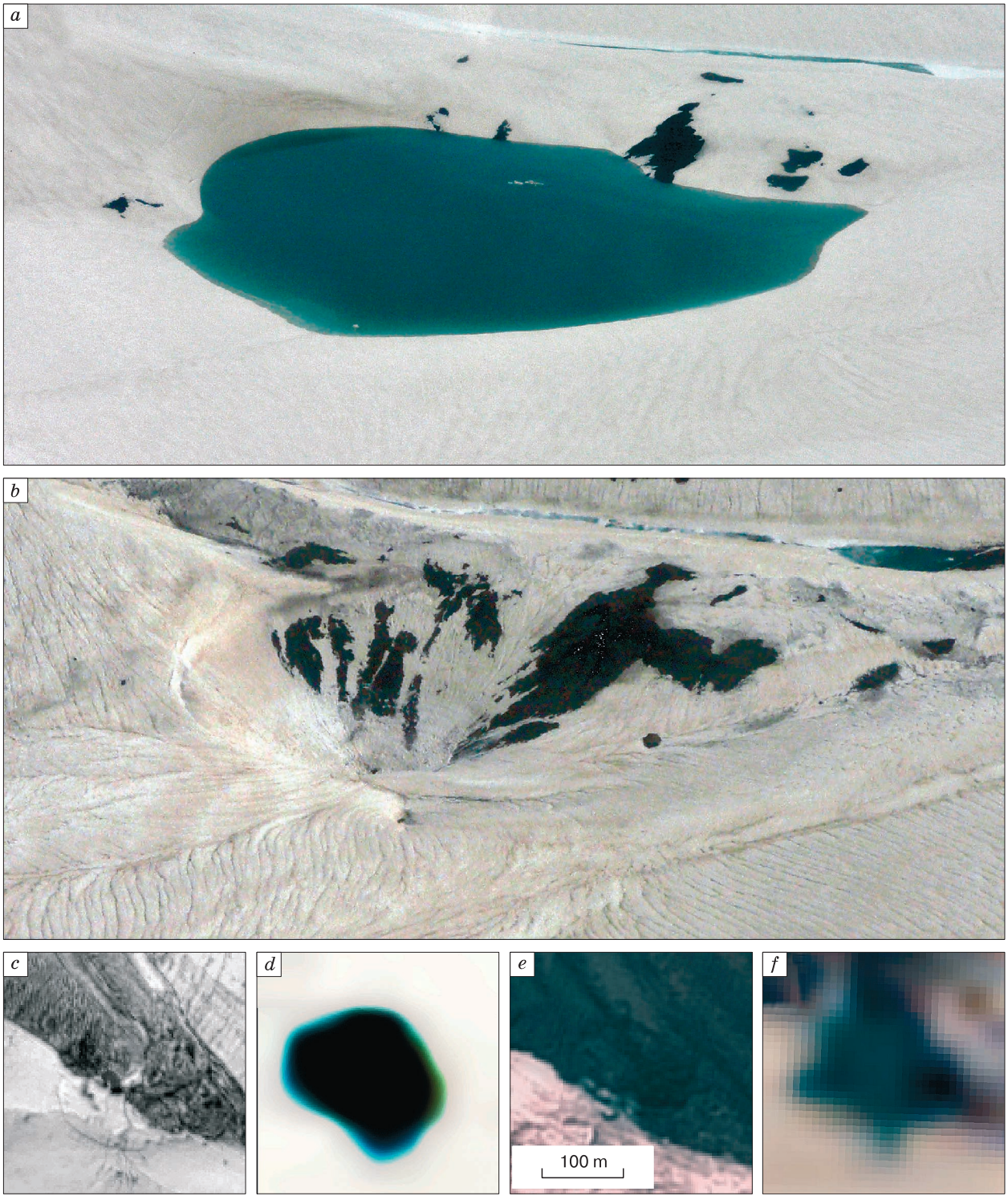

Fig. 6. Lake 12 on a massif of dead ice of median moraines:

(*a*) Photo by M.D. Dokukin (June 18, 2009), (*b*) photo by M.D. Dokukin (June 17, 2011), (*c*) EROS A satellite image (June 20, 2007), (*d*) Landsat-5 image (June 25, 2009), (*e*) SPOT 5 image (Sept. 21, 2011), and (*f*) Landsat-8 image (June 13, 2013).

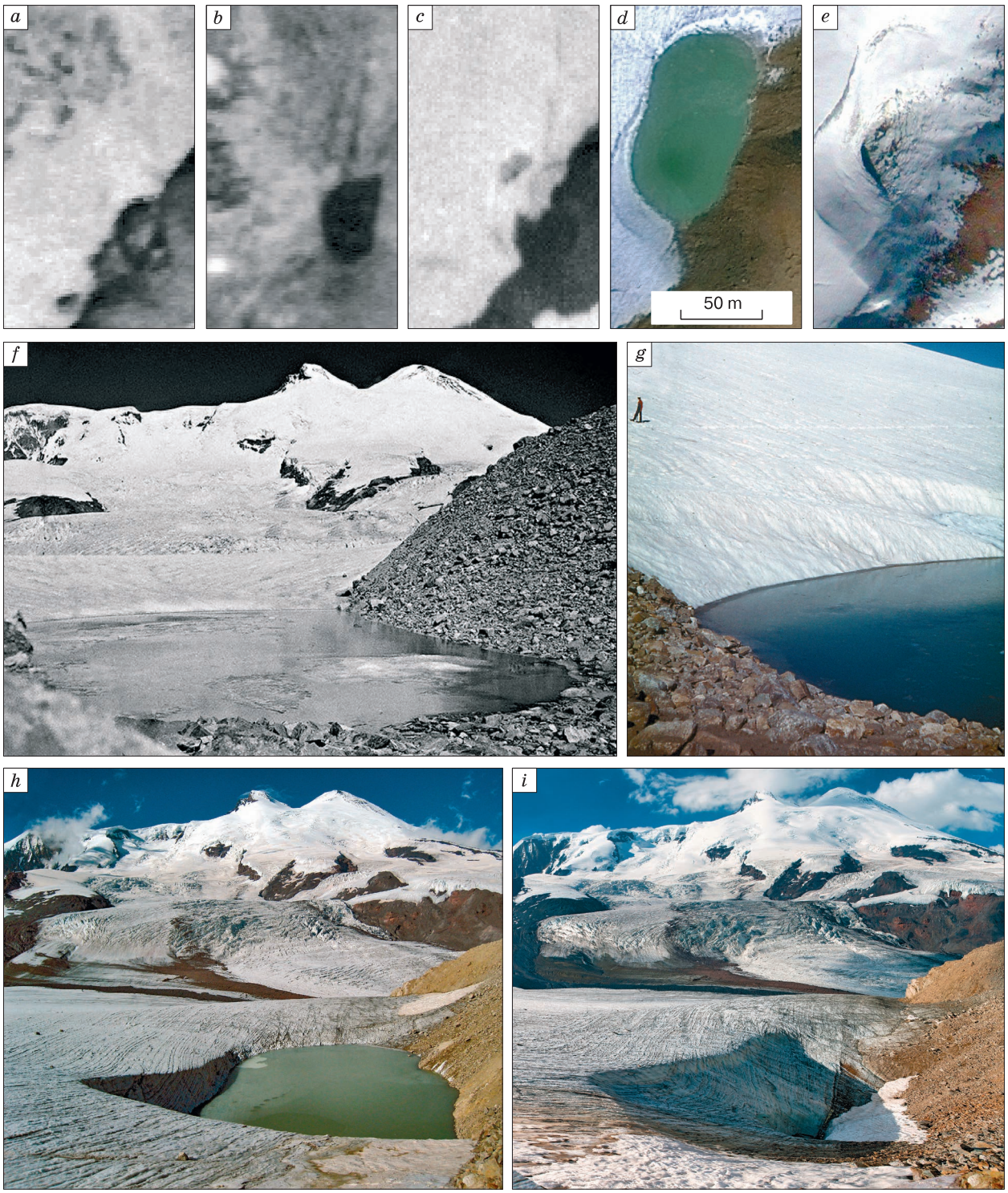

Fig. 7. Lake 15 on the Echo of War Passage:

(*a*) Aerial photo (Sept. 8, 1973), (*b*) aerial photo (Aug. 17, 1983), (*c*) aerial photo (July 27, 1988), (*d*) GeoEye-1 image (Sept. 19, 2009), (*e*) GeoEye-1 image (Oct. 16, 2009), (*f*) photo by V.F. Sukhomeilo (Aug. 29, 1973), (*g*) photo "uz89" (July 1985), (*h*) photo by Ya. Berezhko (Aug. 27, 2009), and (*i*) photo by Ya. Berezhko (Aug. 4, 2012).

180 m long. By May 18, its length reached 260 m, and the lake existed until June 14. In 2019, the lake appeared in mid-May and reached a length of 250 m by early June (Fig. 5*c*). In July, the lake was relatively small and disappeared at the end of the month. In 2020, satellite images made in May were unsuitable for lake detection because of the high cloudiness. In June 2020, the length of the lake reached 150 m; on July 8, 180 m. On July 11, the lake disappeared. In 2021, in May–June, satellite images were cloudy; at the end of June, the lake reached a length of 200 m; on July 8, it disappeared.

Lake at the Echo of War Passage (no. 15)

The lake existed in September 1971 (satellite image KH-4B (Corona) as of September 20, 1971, area of 550 m^2). In 1973, it was recorded on a photo by V.F. Sukhomeilo from August 29 (Fig. 7*f*) and on the aerial photo from September 8 (Fig. 7*a*, 630 m^2). In 1983, in an aerial photo on August 17, the area of the lake reached 770 m^2 (Fig. 7*b*). The lake was seen in July 1985 (Fig. 7*g*) and was absent in 1988 (Fig. 7*c*). There were no signs of its existence on the orthophotomap of 1997. The maximum area of 454 000 m^2 was determined from the satellite image of July 20, 2007, when a powerful surface runoff from the lake was seen. On March 31, 2009, there were no signs of the lake on the photo taken by Ya. Berezhko. In 2009, the lake was seen on the photos by Ya. Berezhko made on August 27, 29, and 30 and on a satellite image from September 19 (Fig. 7*d*). No signs of the lake were reveled on the satellite image as of October 16, 2009 (Fig. 7*e*). On July 30, 2010, the lake was seen on the Landsat-5 satellite image; on the image from August 8, it was absent. It was not absent on the photo taken by Ya. Berezhko on August 23, 2010. The lake cannot be seen on subsequent satellite images and photos. The approximate volume of the lake in 2009 in comparison with the topographic map of 2012 was 18 000–20 000 m^3, the depth was about 10 m.

DISCUSSION AND CONCLUSIONS

The conducted study made it possible to identify glacier lakes that existed in different periods near the Bolshoy Azau Glacier and on the glacier itself. The parameters of their long-term and seasonal dynamics were determined and compared to those of other lakes in different regions. Based on the data obtained, the following conclusions were made:

1. The areas of the identified lakes are small: up to 1000 m^2 – 4 lakes; 1000–5000 m^2 – 7 lakes; 5000–10 000 m^2 – 2 lakes, and more than 10 000 m^2 – 2 lakes. Based on the area of the lakes, the risks of lake breakthrough have been assessed differently. Thus, according to [*Rinzin et al., 2021*], the minimum threshold for the area of outburst-prone lakes is 50 000 m^2. For lakes smaller than 50 000 m^2, the breakthrough hazard index is low. In the new catalog of glaciers in Russia [*Khromova et al., 2021*], glacial lakes are considered hazardous, if their area is more than 5000 m^2. According to these criteria, four lakes (nos. 11–14) can be classified as hazardous.

2. According to the location relative to the glacier, the identified lakes can be classified as periglacial (at a distance of up to 2 km from the glacier, lakes 1–3, 5–8), proglacial (at the contact with the glacier, lakes 10, 15), and supraglacial (on the surface of the glacier or dead ice, lakes 4, 9, 11–14). At the initial stage of formation, lakes 5–9 were proglacial.

3. According to the type of dams, the lakes can be classified into the following groups: moraine–rock bar dams (lakes 1–3, 5–8), ice dams (lakes 10, 15) typical of periglacial and proglacial lakes, and snow-ice dams (lakes 4, 9, 11–14) typical of supraglacial lakes. Moraine-rock bar dams are resistant to erosion and slumping. Dynamics of the lakes bounded by them is determined by the balance of water inflow due to liquid precipitation in the catchment area, snow and ice melting, and water outflow from the basins through underground drainage channels. This explains the disappearance of lakes in the fall-winter period, when the filtration of water through the bottom of the lakes continued in the absence of water inflow into the basins.

Ice dams of proglacial lakes prevent the flow of water from the lakes until subglacial flow channels are formed, which leads to the disappearance of lakes in the fall-winter period. This was observed for lake 15: it was not found in March 2009 on the photo taken by Ya. Berezhko, but in the summer the lake reappeared (satellite image from September 19, 2009). Subsequently, with the retreat of the glacier to lower altitude levels and a decrease in its thickness, the basins of proglacial lakes and 15 were leveled and the lakes no longer appeared on the surface. Lake 15 passed through the stage of an increase in the mass balance of the glacier (in the late 1980s–mid-1990s), and the basin was filled with ice.

Snow-ice dams were formed annually at supraglacial lakes 9, 11, 13, and 14. The lakes existed in May–June, when the snow cover was still preserved until the snow-ice dams were eroded by concentrated flows of meltwater or melted. Before that, there was a period (as the dynamics of young lake 13 indicates), when a funnel was formed on the surface of the glacier as a result of ice subsidence. During this period, the outflow from the lake took place through the underground drainage channel; surface runoff through the glacier also developed. In this period, lake 13 existed in the second half of the summer (2019–2020). Supraglacial lake 12 has an ice dam, but the underground drainage channel can be blocked by seasonal snow-ice or debris masses slipping from the slopes of its basin.

4. The development of supraglacial lakes and their outbursts are characterized in studies of ice sheet lakes in Greenland and Antarctica [*Legleiter et al., 2014; Corr et al., 2022; Dirscherl et al., 2021*], as well as of glacier lakes in the Himalayas, Tibet, and other mountainous regions, including the outburst of a supraglacial lake with a volume of more than 1 million m^3 on the Halji Glacier in the Limi Valley (Nepal) [*Kropácek et al., 2015*]. The number of supraglacial lakes on one glacier can be very significant. For example, on the Chapdara Glacier in the basin of the Gunt River in the Pamirs, the authors identified more than 140 supraglacial lakes, the largest of which had an area of about 8000 m^2.

5. According to [*Kutuzov et al., 2019*], in the part of the Bolshoy Azau Glacier, where lakes 12–14 exist, the ice thickness exceeds 100 m. In this area, a redeepening of the subglacial relief was observed [*Lavrentyev et al., 2020*], where the development of a subglacial lake is quite possible. Moreover, ongoing degradation of a glacier could also produce a large lake on the surface of the residual dead ice. In this regard, the appearance of supraglacial lakes of a larger size compared to the existing lakes can be supposed. Their outbursts might be cascaded, involving water masses from several supraglacial and subglacial lakes in the outburst flood. In this context, it is expedient to continue satellite monitoring of glacial lakes, conduct ground-based georadar studies of the glacier, and model possible outburst floods.

Acknowledgments. *The authors express their gratitude to the SCANEX Group of Companies and the Planet Research Center for Satellite Hydrometeorology for providing satellite images and to Ya. Berezhko, A. Lebedev, K. Lagodienko, and V.F. Sukhomeylo for providing photos.*

This study was carried out within the framework of the Plan of Research and Technological works of research institutions of Roshydromet (theme 6.3.2 AAAA-A20-120031990040-7) and the Development Program of the Interdisciplinary Scientific and Educational School of Lomonosov Moscow State University "The Future of the Planet and Global Environmental Changes".

References

Atlas of Elbrus Glaciers. Part III. *General Geographical Maps*. 1965. Moscow, Izd. Mosk. Gos. Univ. (in Russian).

Allen S.K., Rastner P., Arora M. et al., 2016. Lake outburst and debris flow disaster at Kedarnath, June 2013: hydrometeorological triggering and topographic predisposition. *Landslides* 13, 1479–1491.

Bekkiev M.Yu., Dokukin M.D., Kalov R.Kh., Tashilova A.A., 2021. Modern degradation of valley glaciers in the Central Caucasus. *Fundamentaln. prikladn. klimatolog.* **7** (3), 113–141 (in Russian).

Chernomorets S.S., Petrakov D.A., Alejnikov A.A. et al., 2018. The outburst of Bashkara Glacier lake (Central Caucasus, Russia) on September 1, 2017. *Earth's Cryosphere* XX (2), 61–70.

Chernomorets S.S., Petrakov D.A., Tutubalina O.V. et al., 2007. Breakthrough of a glacial lake on the northeastern slope of Elbrus on August 11, 2006: forecast, event and consequences. *Materialy Glyatsiol. Issled.* 102, 225–229 (in Russian).

Corr D., Leeson A., McMillan M., Zhang C., Barnes T., 2022. An inventory of supraglacial lakes and channels across the West Antarctic Ice Sheet. *Earth Syst. Sci. Data* 14, 209–228.

Dirscherl M.C., Dietz A.J., Kuenzer C., 2021. Seasonal evolution of Antarctic supraglacial lakes in 2015–2021 and links to environmental controls. *The Cryosphere* **15**, 5205–5226.

Dokukin M.D., Khatkutov A.V., 2016. Lakes near the glacier Maliy Azau on the Elbrus (Central Caucasus): dynamics and outbursts. *Led i Sneg* **56** (4), 472–479 (in Russian).

Dokukin M.D., Savernyuk E.A., Bagov A.M., Markina A.V., 2012. Reconstruction of the hydrographic network of the northeastern foot of Elbrus (basins of the Birjaly-Su and Kara-Kaya-Su rivers), *Led i Sneg* **118** (2), 23–30 (in Russian).

Dokukin M.D., Savernyuk E.A., Bekkiev M.Y. et al., 2022. Evolution of lakes near the Dzhikiugankez Glacier (Northern Elbrus area) in 1957–2020 with consideration of underground flow channels. *Led i Sneg* **62** (1), 47–62 (in Russian).

Dokukin M.D., Shagin S.I., 2014. Features of dynamics of glacial lakes with underground drain channels (analysis of multitemporal aerospace information). *Earth's Cryosphere* XVIII (2), 41–50.

Emmer A., 2018. GLOFs in the WOS: bibliometrics, geographies and global trends of research on glacial lake outburst floods (Web of Science, 1979–2016). *Nat. Hazards Earth Syst. Sci.* **18**, 813–827.

Gerasimov A., 1909. About the breakthrough of a on the northern slope of Elbrus. Izv. Geologich. Komiteta **28** (7), 156–160 (in Russian).

Ivanov M.A., 1902. In the Baksan gorge. In: *Proc. of the Imperial Geographical Society*, vol. XV, p. 7–20 (in Russian).

Khromova T.Y., Nosenko G.A., Glazovsky A.F. et al., 2021. New inventory of the Russian glaciers based on satellite data (2016–2019). *Led i Sneg* **61** (3), 341–358 (in Russian).

Kropácek J., Neckel N., Tyrna B. et al., 2015. Repeated glacial lake outburst flood threatening the oldest Buddhist monastery in north-western Nepal. *Nat. Hazards Earth Syst. Sci.* **15**, 2425–2437.

Kutuzov S., Lavrentiev I., Smirnov A. et al., 2019. Volume changes of Elbrus glaciers from 1997 to 2017. *Frontiers Earth Sci.* **7**, article 153.

Lavrentyev I.I., Petrakov D.A., Kutuzov S.S. et al., 2020. Assessment of glacier lakes development potential in the Central Caucasus. *Led i Sneg* **60** (3), 343–360 (in Russian).

Legleiter C.J., Tedesco M., Smith L.C. et al., 2014. Mapping the bathymetry of supraglacial lakes and streams on the Greenland ice sheet using field measurements and high-resolution satellite images. *The Cryosphere* **8**, 215–228.

Mergili M., Pudasaini S.P., Emmer A. et al., 2020. Reconstruction of the 1941 GLOF process chain at Lake Palcacocha (Cordillera Blanca, Peru). *Hydrol. Earth Syst.* **24**, 93–114.

Rinzin S., Zhang G., Wangchuk S., 2021. Glacial lake area change and potential outburst flood hazard assessment in the Bhutan Himalaya. *Frontiers Earth Sci.* **9**, article 775195.

Seynova I.B., Zolotarev E.A., 2001. *Glaciers and Debris Flows of the Elbrus Region*. Moscow, Nauchny Mir, 204 p. (in Russian).

URL: http://goto.arcgisonline.com/maps/World_Imagery/ World Imagery Map (last visited: December 4, 2022).

URL: https://apps.sentinel-hub.com/eo-browser/Sentinel Hub EO Browser (last visited: December 4, 2022).

URL: https://doi.org/10.3389/feart.2021.775195 (last visited: December 4, 2022).

URL: https://earthexplorer.usgs.gov / Earth Explorer (last visited: December 4, 2022).

URL: https://risk.ru/blog/198343/For the first time to Elbrus or a family crossing over the Khotyutau Pass in 1985 (last visited: December 4, 2022).

Vasil'chuk Yu.K., Chizhova Yu.N., Budantseva N.A., Mukhina Yu.S., 2010. Fast retreat of the Bolshoy Azau Glacier in the Elbrus area in stable climatic conditions and associated risks. *Georisk* **2**, 16–29 (in Russian).

Received February 10, 2022
Revised October 3, 2022
Accepted December 7, 2022

Translated by E.S. Shelekhova

EARTH'S CRYOSPHERE
SCIENTIFIC JOURNAL

Earth's Cryosphere, 2023, vol. XXVII, No. 1, pp. 51–57

METHODS OF CRYOSPHERIC RESEARCH

METHODOLOGY FOR ZONING OF THE TERRITORY OF LONG-DISTANCE LINEAR OBJECTS ACCORDING TO THERMOKARST FORMATION CONDITIONS

E.M. Makarycheva[1,*], V.P. Merzlyakov[2], O.K. Mironov[2]

[1] *Pipeline Transport Institute LLC (Transneft R&D, LLC), Sevastopolskiy prosp. 47a, Moscow, 117186 Russia*
[2] *Sergeev Institute of Environmental Geoscience, Russian Academy of Sciences, Ulanskiy per. 13, bld. 2, Moscow, 101000 Russia*

**Corresponding auhtor; e-mail: MakarychevaEM@niitnn.transneft.ru*

The probabilistic-statistical method has been applied to study the causes of the thermokarst distribution heterogeneity along the long linear constructions. A list of natural conditions affecting the development of thermokarst along an oil pipeline is discussed. The methodology for zoning buffer area of long-distance linear constructions (e.g., oil pipeline) according to the conditions of thermokarst development is substantiated. We have delineated and mapped thermokarst-susceptible and thermokarst-tolerant areas along the oil pipeline buffer zone according to the environmental conditions.

Keywords: *thermokarst, trunk pipeline, zoning, big data, probability, statistics.*

Recommended citation: Makarycheva E.M., Merzlyakov V.P., Mironov O.K., 2023. Methodology for zoning of the territory of long-distance linear objects according to thermokarst development conditions. *Earth's Cryosphere* XXVII (1), 51–57.

INTRODUCTION

In this paper, we define thermokarst phenomena as landforms appearing in a particular time slice of thermokarst process or after its end due to melting of massive or segregated ground ice, compaction of thawed ground, and its deformation regardless of the scale of the process [*Shur, 1988*]. In this paper, we consider both relic and ancient thermokarst phenomena along with modern ones.

Big data on the object and environmental conditions are being accumulated during the operation of trunk oil pipelines. In conditions of long-distance linear objects' specificity, it is impossible to provide equal spatiotemporal detail of information; one faces the problems of interpolation and extrapolation of data.

Numerical models describing the state of the "pipeline–environment" system have a range of limitations [*Radionova et al., 2016*]:

– a large set of required initial data,

– the need for the hypotheses about changes in the initial data with time;

– inconsistency between the grid size of the available environmental parameters and their actual variability,

– impossibility of comparing data of different scales.

Accumulation of big time-series data and the impossibility of providing equal spatiotemporal detail on linear objects' environment encourage the search for new means of processing and analyzing information, as well as the need to form a basis for rational planning of geological survey, considering the necessity and sufficiency requirements.

METHODOLOGY

This paper is aimed to develop and justify the methodology for zoning the territory of long-distance linear objects according to the conditions of thermokarst formation. East Siberia–Pacific Ocean-1 (ESPO-1) trunk oil pipeline buffer area has been chosen as the study area. This is the longest pipeline in the permafrost area (Fig. 1). Buffer area of trunk oil pipeline ESPO-1 is a 3-km-wide strip of land (1.5 km from the pipeline axis), 2085 km long (in the permafrost zone).

The width of the ESPO-1 buffer area allows one to conduct the analysis of thermokarst phenomena both in the zone of influence of the oil pipeline and in the undisturbed conditions. The underground laying of the oil pipeline along the entire route suggests an approximately similar technogenic impact on the environment during the construction and operation of the pipeline.

During the study, we identified thermokarst phenomena within the pipeline buffer area, searched for cause-and-effect relationships of uneven thermokarst distribution across the study area, and zoned the buffer area according to thermokarst forming conditions [*Makarycheva, 2018*].

Fig. 1. Scheme of trunk oil pipelines located in the areas with complicated environmental conditions.

(*1*) trunk oil pipelines of Transneft PJSC, (*2*) oil pipelines of Transneft PJSC under construction and design, (*3*) other trunk oil pipelines, (*4*) trunk pipelines for oil products of Transneft PJSC, (*5*) projected trunk pipelines for oil products of Transneft PJSC, and (*6*) geotechnical monitoring sites of Transneft PJSC.

Topographic maps of different scales, satellite images and aerial photographs of ultrahigh spatial resolution (0.19 m/pixel), three-year-long aerial and ground survey data obtained by the Sergeev Institute of Environmental Geoscience, Russian Academy of Sciences (IEG RAS) and the ESRC (Research Center for Emergency Situations) LLC in 2010–2012, as well as the results of engineering geological surveys and archieve data.

Thermokarst genesis of the identified landforms is confirmed by engineering-geological survey data, as well as by the additional image interpretation features, such as the subsidence of coastal slopes (cracks parallel to the slope and alternation of deep and shallow areas of the shore underwater part). An additional identification feature of thermokarst was the stable or positive dynamics of the waterlogging of the area throughout the entire survey period despite climatic oscillations. Overall, 2146 thermokarst landforms were identified and mapped.

Aerial survey data from 2011–2012 were also used to identify with compensatory measures and repair works and analyze the influence of thermokarst on the operation of the trunk oil pipeline.

We applied a probabilistic-statistical method to search for cause-and-effect relationships for the uneven distribution of thermokarst phenomena across the study area. As the source data, we used small-scale maps [*Fedorov et al., 1989; Fedorov, 1991; Mel'nikov, 1991; Ershov, 1996*], thematic large-scale maps of the territory along the oil pipeline created by the IGE RAS in 2010, the map of environmental complexes (scale 1:50,000), and the map of morphostructural zoning (scale 1:100,000), as well as archieve data [*Gerasimov, 1965; Kudryavtsev, 1975; Tyrtikov, 1976; Ospennikov et al., 1980*].

Thematic maps contain several characteristics of the study area. For example, the map of environmental complexes contains information about the landscape units, vegetation, topography, and swampiness of sections of the oil pipeline route. Landscape units are understood here as taxonomic units of the landscape distinguished by the homogeneity of the topography and zonal types of vegetation.

According to the map of morphostructural zoning, pre-neotectonic (ancient) regional structures and second-order neotectonic structures (arch, trough, and uplift) are identified within the study area.

Second-order neotectonic structures are distinguished by their direction (vertical and horizontal), intensity of movements, and features of their expression in the topography. Arches are mainly formed by vertical movements (stresses) and, to a lesser extent, by subhorizontal movements. These are relatively stable oval-shaped or isometric rises. Within the plat-

forms, arches can be expressed in the form of slightly convex plateaus (arch-like plateaus) with a well-developed "ladder" of geomorphic surfaces.

Uplifts and troughs are formed due to predominantly subhorizontal movements (stresses) and are more intensively developing forms compared to arches. They have an extended or linear type of development. As a rule, uplifts and troughs are conjugated forms and are characterized by zonal development associated with highly active tectonic areas.

Independence of criteria while creating environmental (landscape) maps of the area allows to use them for searching the connections between thermokarst development and different geographical and geological conditions within the oil pipeline route, as well as to increase the reliability of the obtained data.

The influence of areal environmental conditions on the thermokarst distribution was carried out in a series of independent experiments. Thermokarst landforms and the particular environmental and technogenic conditions along the pipeline route were considered together.

A series of independent tests were carried out with following settings. We selected a characteristic of the study area, whose influence on the distribution of thermokarst interested us, for example, the separation of the territory by landscape units. A set of landscape units within the study area was determined. In our case, there were four landscape units: (1) intrazonal (terrace complexes of river valleys, floodplains, valleys of small rivers and waterlogged hollows, raised and transitional bogs, areas burned by a surface fire); (2) forest; (3) forest-tundra, mostly flat (plateaus); and (4) forest-tundra, mountainous. Then, we analyzed each kilometer of the pipeline route and identified the types of landscape units within it; the thermokarst phenomena within the identified landscape units were recorded. We summarized these data as in a table with the rows corresponding to kilometer areas of the pipeline route and the columns indicating landscape units. This information was encoded as follows: 0 – there is no such landscape unit within the study area, 1 – area is characterized by this landscape unit without thermokarst , and 2 – area is characterized by this landscape unit with thermokarst.

Next, we calculated the occurrence frequency of thermokarst landforms for each landscape unit. For this, we determined the number of kilometer areas of the pipeline route containing the given landscape unit and the number of them characterized by thermokarst phenomena. These operations were performed using GIS query builder, which allows to select all rows with a value of 1 and 2 from the table while calculating the occurrence of landscape units or 2 while calculating the occurrence of thermokarst phenomena.

Statistical processing was done in MapInfo software by applying a special algorithm to optimize processing time and increase reliability of the results [*Makarycheva et al., 2018*].

Thus, we obtained the data for statistical processing: the occurrence frequency of given landscape units N_k (the number of kilometer-long sections of the route containing a given landscape unit), the total occurrence of all landscape units $N \quad \sum N$ the frequency of thermokarst occurrence in a landscape unit n_k (the number of kilometer-long sections containing a given landscape unit with thermokarst), and the total number of all outcomes of the experiment $n \quad \sum n$ where k = 1, 2, 3, 4 is the number of the landscape unit.

For statistical processing, it was assumed that: (1) the presence or absence of thermokarst phenomena in a given landscape unit (under given natural or technogenic conditions) is a *random event* (the outcome of the experiment); and (2) thermokarst phenomena have a *uniform* distribution of probabilities across all landscape units; the more often a given landscape unit occurs, the greater the likelihood of finding thermokarst phenomena in it.

These assumptions, as well as the above-mentioned method of determining the occurrence of a very short section length in comparison with the total length of the pipeline route, allow to accept the formula $p_k = N_k/N$ for calculating the probability p_k of thermokarst occurrence in the k-unit. If the specified assumptions are true, then the frequencies of occurrence of thermokarst phenomena should have a polynomial probability distribution [*Prokhorov et al., 1988*].

Below we test the hypothesis that the experimentally obtained frequencies of thermokarst occurrence found within landscape units n_1, n_2, n_3, n_r have a polynomial distribution.

Pearson's chi-squared test is recommended to test this hypothesis [*Prokhorov et al., 1988*]. This criterion, however, rejects the hypothesis, for all indices k in case of disagreement, if the occurrence of outcomes in at least one landscape unit is *nonrandom*. The authors are interested, however, in discrimination between *random* and *nonrandom* (subjected to systematic influences of conditions, the presence of connections). It is impossible to answer this question using the Pearson's criterion.

The polynomial distribution has an important property: each of the r random variables n_k has a binomial probability distribution. This allows us to consider a system of k different binomial distributions with the expected values $M_k = np_k$ (theoretical frequencies), dispersions $D_k = np_k\left(1-p_k\right)$, and standard deviations $\sigma_k = \sqrt{np_k\left(1-p_k\right)}$ instead of one polyno-

Table 1. **Analysis output: influence of landscape units on the distribution of thermokarst in the buffer area of the oil pipeline**

Numerical characteristics	Landscape unit			
	Intrazonal	Forest	Forest-tundra, mainly flat (plateaus)	Forest-tundra mainly mountainous
Number of landscape unit (k)	1	2	3	4
Total occurrence of thermokarst within all landscape units (n)	388	388	388	388
Detected occurrence of thermokarst within one landscape unit (n_k)	216	158	4	10
Lower threshold of "reliability" ($M_k - 3\sigma_k$)	105.28	174.86	–2.14	29.28
Upper threshold of "reliability" ($M_k + 3\sigma_k$)	161.41	233.87	4.95	68.50
Connection characteristic of the direct type $\delta_k\uparrow$	54.6	–	–	–
Connection characteristic of the inverse type $\delta_k\downarrow$	–	16.86	–	19.28
Type of relationship	Direct	Inverse	Absent	Inverse

mial distribution, where $n \quad \sum n$ is the total occurrence of thermokarst within all landscape units.

Using the above equations, one can obtain numerical characteristics allowing to extract nonrandom experimental results [*Makarycheva et al., 2018*]. For this, for each landscape unit, the 3σ-rule was used; this rule is widely applied in mathematical statistics [*Ivashov-Musatov, 2003*]. By calculating M_k, σ_k, and making a comparison, we can state that our hypothesis is true, if n_k falls within the interval:

$$\left[M_k - 3\sigma_k; M_k + 3\sigma_k\right]. \quad (1)$$

In this case, the value n_k is the value of a random variable that obeys the specified distribution law. Otherwise, the hypothesis is rejected, from which it follows that this landscape unit systematically affects the value of n_k.

If $n_k > M_k + 3\sigma_k$ (experimental frequency is higher than the upper threshold), then k-landscape unit promotes the thermokarst formation:

$$\delta\uparrow = n_k - \left(M_k + 3\sigma_k\right). \quad (2)$$

If $n_k < M_k + 3\sigma_k$ (experimental frequency is lower than the lower threshold), the landscape conditions hinder the thermokarst formation:

$$\delta\downarrow = \left(M_k - 3\sigma_k\right) - n_k. \quad (3)$$

Values (2) and (3) can be called quantitative characteristics of direct and inverse relationships. They are expressed by numbers showing the excess of the upper threshold (1) by the experimental frequency and the amendment to the experimental frequency to the lower threshold, respectively.

Table 1 summarizes the results of probabilistic-statistical analysis of the relationship between the thermokarst phenomena and the landscape units in the buffer area of the oil pipeline.

The occurrences of landscape units had the following values $N_1 = 1331$, $N_2 = 2040$, $N_3 = 14$, $N_4 = 488$, $N = 3873$.

We have performed the zoning of the buffer area of the trunk oil pipeline according to conditions that promote or hinder the formation of thermokarst phenomena based of dependencies obtained from the probabilistic-statistical analysis. All conditions and factors were divided into two groups: those promoting the formation of thermokarst and those hindering the formation of thermokarst. Promoting conditions were those, for which direct relationship with the thermokarst occurrence frequency was found. Hindering conditions were characterized by the inverse relationship with the thermokarst occurrence frequency. Then, we generated two separate zoning maps by overlaying the distribution areas according to conditions that promote and hinder thermokarst formation.

THERMOKARST DISTRIBUTION HETEROGENEITY ANALYSIS

The considered analysis has been applied to the entire oil pipeline route and for each of the three ancient tectonic structures separately.

Thermokarst phenomena are distributed unevenly relative to ancient tectonic structures, but neither direct nor inverse relationships with particular tectonic structures have been identified. At the same time, regional ancient structures determine the material and structural heterogeneity of the territory, which in turn indirectly affects the patterns of thermokarst distribution.

The oil pipeline route crosses three ancient tectonic structures: sedimentary layer of the Siberian Platform (including the Central Siberian Plateau), the Aldan-Stanovoy shield of the Siberian Platform,

and the Mongol-Okhotsk fold system. We have identified changes in the relationships between thermokarst distribution landscape conditions (landscape unit, vegetation, topography), and second-order morphostructures of the relief (arch, uplift, trough) during the transition from one tectonic structure to another. We have also determined quantitative characteristics of these relationships and their direction (direct, inverse, or no connection) and identified conditions affecting the thermokarst formation.

Table 2 summarizes the sample of environmental conditions directly affecting thermokarst development as obtained from the statistical analysis of data on the three ancient tectonic structures. It should be noted that a change in both the type of relationships and their quantitative characteristics takes place upon the transition from one tectonic structure to another.

We have statistically proven the relationship between the distribution of thermokarst and uplift zones within the sedimentary layer of the Siberian Platform. This relationship is debatable; it is important that second-order morphostructures of the relief that reflect the direction and intensity of neotectonic movements can often manifest themselves not directly, but through other factors, including the entire set of landscape conditions.

It can also be assumed that denudation processes in the areas of uplifts lead to the displacement of the base of the active layer deep into the rock, so that it reaches layers with the high ice content, which are susceptible to thermokarst. The oil pipeline route in the southern part of the Central Siberian Plateau is characterized by the distribution of permafrost (including high-ice permafrost and permafrost with ice wedges) buried under the layer of surface sediments.

Table 2. **Quantitative environmental assessment of relationships between thermokarst distribution wand environmental conditions within ancient tectonic structures**

Environmental conditions	Platform (sedimentary layer)	Aldan-Stanovoy shield	Mongol-Okhotsk fold system
Direction of neotectonic movements			
Arch	Inverse	1.00*	Absent
Uplift	36.50	Absent	Absent
Landscape unit			
Intrazonal landscapes	29.29	14.11	Absent
Forest-tundra, mainly flat (plateaus)	Absent	Absent	0.28
Topography			
Elevated moderately dissected plateaus and steplike plateaus	Absent	3.18	Absent
Low valleys and intermountain depressions	8.69	Absent	Absent
Low-elevation ridged relief	1.49	Absent	Absent
Mid-elevated moderately dissected plateaus and steplike plateaus	48.27	Absent	Absent
Vegetation			
Raised and transitional bogs	Absent	0.93	Absent
Bogs and transitional fens with meadow-bog communities	Absent	7.09	Absent
Meadow-shrub communities with individual small-leaved trees	9.35	Absent	Absent
Burnt areas with groups of larch, less often pine with burned ground cover	2.40	Absent	Absent
Birch and willow shrublands with single low larch, pine, and birch trees, deadwood on felling sites and burnt areas, partially swampy	Absent	Absent	1.24
Birch shrub-green moss communities with single larch, pine, and birch	23.85	Absent	Absent
Shrub hummock communities with single low larch and birch trees, often swampy	8.37	6.80	Absent
Larch woodlands with patches of rocky ground	7.68	Absent	Absent
Larch-birch and birch forests	8.45	Absent	Absent
Non-vegetated dredging areas	Absent	Absent	0.52
Pine-spruce-fir forests	12.82	Absent	Absent
Pine and birch forests with isolated wetlands	8.06	Absent	Absent

* All presented values represent quantitative characteristics of direct relationships: $\delta_k\uparrow = n_k - (M_k + 3\sigma_k)$.

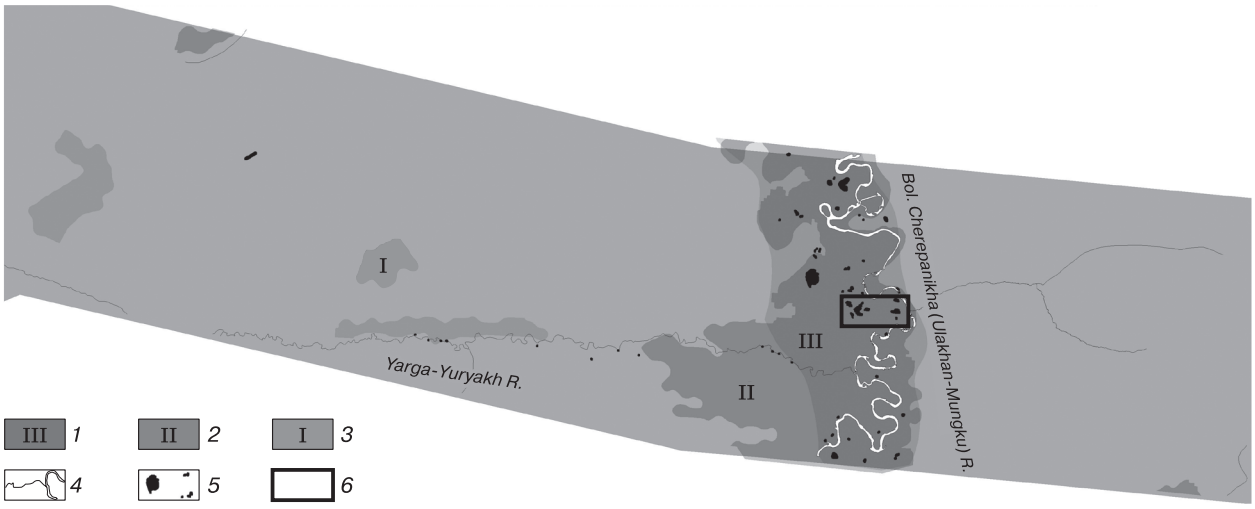

Fig. 2. Fragment of the zoning map of buffer area of the trunk oil pipeline at the intersection with the Bolshaya Cherepanikha River according to conditions of thermokarst development:

Superposition of (*1*) three (III) and (*2*) two (II) environmental conditions promoting the development of thermokarst, (*3*) one (I) environmental condition favoring the development of thermokarst; (*4*) streams, (*5*) thermokarst phenomena, and (*6*) site of ground geological survey.

In the discontinuous permafrost zone of the Central Siberian Plateau, thermokarst phenomena are confined to intrazonal landscapes, which is associated with the widespread distribution of sandy loamy and biogenic (peat) sediments with the high ice content in these landscapes (Fig. 2).

Additionally, we have identified the relationship between burnt areas (fires) and thermokarst for the Siberian Platform. Disturbances of vegetation cover resulting from fires create conditions for the uneven thawing of peat and formation of water-filled depressions. Surface subsidence begins under these depressions. Small lakes are formed, if peatlands are underlain by not subsiding permafrost with the low ice content.

In the Aldan Shield area of the Siberian Platform, thermokarst phenomena are mostly confined to the arch zones. Minor topographic differences represented by elevated plateaus and step-like plateaus with moderately dissected surfaces create limited conditions for drainage of surface water. Modern tectonic activity in the near-surface zone occurs under extensional conditions (the route crosses these structures across their strike), which is the reason for the presence of a large number of elevated river terraces. Fens and transitional bogs, as well as swampy areas, are widespread within the Aldan shield; their freezing and subsequent thawing contributes to the development of thermokarst.

Neotectonic movements are highly intense in area where the oil pipeline route crosses the Mongol-Okhotsk fold system. Zones of uplifts and troughs are characterized by large differences in elevation. In this area, no relationship between thermokarst development and neotectonic structures has been found. At the same time, we have found the relationship of thermokarst phenomena with partially swampy clearcut and burnt areas on plateaus occupied by birch and willow communities. The morphological characteristics of individual thermokarst phenomena (the shape of the coastline cut by straight segments with right angles, grid-like patterns or blocks on aerial photographs and satellite images) indicate the spread of ice wedges.

ZONING THE BUFFER AREA OF THE TRUNK OIL PIPELINE ACCORDING TO THERMOKARST FORMING CONDITIONS

The obtained dependencies formed the basis for the zoning of the territory. All conditions and factors were divided into two groups: those that hinder the thermokarst formation and those that promote it.

Based on the results of this work, we have compiled zoning maps of the three-kilometer buffer area of the trunk oil pipeline (scale 1:50,000) over 2085 km (Fig. 2). These maps provide rationale for selecting and optimizing the observation network of monitoring points.

Areas with the direct relationship between thermokarst development and environmental conditions are indicated by color and the number. The more conditions favor thermokarst, the more intense is the color.

The site of ground geological observations lies in the discontinuous permafrost zone, within which three environmental conditions favor thermokarst

development: (1) mid-elevated moderately dissected plateaus and steplike plateaus, (2) intrazonal landscape unit, and (3) larch-birch and birch forests. In the oil pipeline land allotment boundaries (50-m-wide) of this area, we have identified the phenomena of technogenic thermokarst associated with the thermal impact of the operating underground oil pipeline.

Outside the land allotment boundaries, in a three-kilometer zone, we have identified elongated lakes and depressions with the shores dissected by rectilinear segments with right angles.

According to ground observation data (description of pits), the site is composed of low- and medium-ice loam with layered cryostructures. Moreover, a massive ice body of 4 m in thickness was found.

The ground temperature in the boreholes next to the pipeline (–1.5 to –2°C) is higher than in the borehole beyond the land allotment boundaries (–3°C). Data from instrumental measurements in the pit indicated the development of a thaw bulb around the oil pipeline (up to 1.2 m under the pipeline section) [*Novikov et al., 2015*].

CONCLUSIONS

1. We have proposed a methodology for zoning the territory of long-distance linear objects according to the conditions of thermokarst formation based on the probabilistic-statistical method.

2. This methodology allows one to quickly analyze large amounts of data, and also to implement algorithms for automated analysis of the environmental conditions of the area, and to create zoning maps of long-distance linear objects.

3. The probabilistic-statistical method can be used to search for the dependence of thermokarst distribution on the geological and geographical conditions at the stage of design and operation of linear objects, including poorly studied areas.

The differences between the proposed methodology and those previously applied are:

– the ability to determine the experimental outcomes, which are caused by the presence of certain dependencies in the distribution of the phenomena and studied conditions, and which are random,

– the presence of quantitative criteria for the relationships between the studied phenomena and the conditions influencing their distribution,

– the ability to identify conditions both promoting and hindering the spread of the phenomena,

– the ability to analyze both regional and local relationships,

– the possibility of obtaining spatial patterns in conditions of insufficient input data, their uneven spatial distribution, and scales difference.

The developed methodology is universal, it can be applied to analyze spatial relationships when processing large amounts of data accumulated over the lifetime of a long-distance linear object.

Acknowledgments. *This study was performed within the framework of state assignment no. 122022400105-9.*

References

Ershov E.D. (Ed.), 1996. *Permafrost Map of the USSR, 1:2,500,000 Scale*. Vinnitsa, Vinnitsa Cartographic Factory, 16 p. (in Russian).

Fedorov A.N., 1991. *Permafrost Landscapes of Yakutia: Methods of Delineation and Mapping Issues*. Yakutsk, Melnikov Permafrost Institute, 140 p. (in Russian).

Fedorov A.N., Botulu T.A., Varlamov S.P., 1989. *Permafrost Landscapes of Yakutia*. Explanatory Note to Permafrost Landscape map of the Yakut ASSR, 1:2,500,000 scale. Novosibirsk, GUGK USSR, 170 p. (in Russian).

Gerasimov I.P. (Ed.), 1965. *Yakutia*. Moscow, Nauka, 467 p. (in Russian).

Ivashov-Musatov O.S., 2003. *Theory of Probability and Mathematical Statistics*. Moscow, FIMA, 224 p. (in Russian).

Kudryavtsev V.A. (Ed.), 1975. *South Yakutia. Permafrost-Hydrogeological and Engineering-Geological Conditions of the Aldan Mining Region*. Moscow, Izd. Mosk. Gos. Univ., 444 p. (in Russian).

Makarycheva E.M., 2018. *Analysis of Thermokarst Phenomena Distribution Near the Trunk Oil Pipeline System*. Candidate Sci. Theses, Moscow, 256 p. (in Russian).

Makarycheva E.M., Merzlyakov V.P., Mironov O.K., Besperstova N.A., 2018. Analysis of the spread of thermokarst phenomena along an extended linear structure using a probabilistic-statistical method. In: *Actual Problems of Geocryology* (proc. extended meeting of the scientific council on Earth Cryology of the Russian Academy of Sciences). Moscow, Universitetskaya Kniga, vol. II, p. 69–76 (in Russian).

Mel'nikov P.I. (Ed.), 1991. *Permafrost Landscape map of the Yakutskaya ASSR, 1:2,500,000 scale*. Moscow, GUGK USSR, 2 p. (in Russian).

Novikov P., Makarycheva E., Larionov V., 2015. Model of permafrost thaw bulb formation around a pipeline. In: *Engineering Geology for Society and Territory*. Switzerland, Springer, vol. VI, p. 405–408.

Ospennikov E.N., Trush N.I., Chizhov A.B., Chizhova N.I., 1980. *Exogenic Geological Processes and Phenomena (South Yakutia)*. Moscow, Izd. Mosk. Gos. Univ., 226 p. (in Russian).

Prokhorov Yu.V. et al. (Eds.), 1988. Mathematical Encyclopedic Dictionary. Moscow, Soviet Encyclopedia, 846 p. (in Russian).

Radionova S.G., Lisin Yu.V., Kuznetsov T.I. et al., 2016. Improvement of methods and means of forecast calculations of thawing bulbs, penetration and stress-strain state of pipelines laid in permafrost. *Nauka i Tekhnol. Truboprovodn. Transp. Nefti Nefteproduktov* XXI (1), 39–43 (in Russian).

Shur Yu.L., 1988. *Upper Horizon of Permafrost and Thermokarst*. Novosibirsk, Nauka, 213 p. (in Russian).

Tyrtikov A.P., 1976. About thermokarst in the north of Western Siberia. In: *Natural Conditions of Western Siberia*. Moscow, Izd. Mosk. Gos. Univ., iss. 6, p. 145–155 (in Russian).

Received June 4, 2021
Revised November 14, 2022
Accepted December 19, 2022

Translated by Yu.A. Dvornikov

KRIO LAB

ПРОИЗВОДСТВО ОБОРУДОВАНИЯ ДЛЯ ГЕОТЕХНИЧЕСКОГО МОНИТОРИНГА


Термометрическая коса


Контроллер KrioLab TKL


Термокоса, подключенная к контроллеру KrioLab TKL


Термокоса 250м на металлической катушке

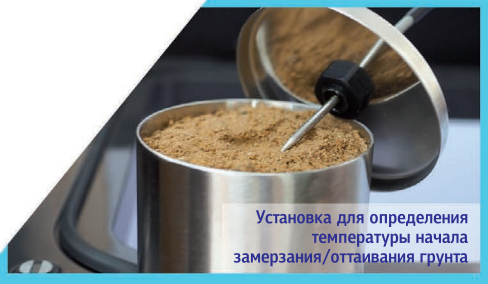
Установка для определения температуры начала замерзания/оттаивания грунта


Лабораторная система температурного мониторинга

- **ПОЛНЫЙ ЦИКЛ РАБОТ:**
  разработка,
  изготовление,
  испытание,
  поверка оборудования,
  поддержка на всех этапах сотрудничества.
- **ВСЕ ОБОРУДОВАНИЕ** — собственные разработки, имеющие патент, соответствующие ГОСТ 25358-2020.
- **Оборудование сертифицировано.**
- **Усовершенствование и апгрейд** под запросы заказчика.
- **Полный перечень оборудования** на сайте компании https://kriolab.ru

https://kriolab.ru

kriolab@kriolab.com
+7 (495) 991-50-81